

**Imperial College
London**

Imperial College London

Department of Mechanical Engineering

**Modelling Electrochemical and Thermal Behaviors
of Silicon-Based Electrodes for Lithium-Ion Batteries**

PhD Thesis

Yang Jiang

Supervisors:

Dr. Huizhi Wang

Department of Mechanical Engineering

Professor Gregory Offer

Department of Mechanical Engineering

July 2023

Declaration of Originality

I hereby declare that this thesis and the work presented herein is my own work except where appropriately referenced or acknowledged.

Yang Jiang

Copyright Declaration

The copyright of this thesis rests with the author. Unless otherwise indicated, its contents are licensed under a Creative Commons Attribution-Non Commercial 4.0 International Licence (CC BY-NC). Under this licence, you may copy and redistribute the material in any medium or format. You may also create and distribute modified versions of the work. This is on the condition that: you credit the author and do not use it, or any derivative works, for a commercial purpose. When reusing or sharing this work, ensure you make the licence terms clear to others by naming the licence and linking to the licence text. Where a work has been adapted, you should indicate that the work has been changed and describe those changes.

Please seek permission from the copyright holder for uses of this work that are not included in this licence or permitted under UK Copyright Law.

Abstract

Silicon (Si) has become an attractive alternative to graphite (Gr) as an anode material for the next generation lithium-ion batteries (LIBs) due to its high theoretical capacity, natural abundance, and reasonable electrode potential. However, Si-based electrodes exhibit distinct electrochemical and thermal behaviors compared to traditionally used carbonaceous electrode, and there have been rare models tailored to the behaviors of Si-based electrodes. Therefore, this thesis aims to develop physics-based models able to describe and predict the electrochemical and thermal behaviors of Si-based electrodes, which can serve as important tools for understanding and designing LIBs with Si-based anodes.

A mechanistic model of silicon anodes in LIBs is first developed to describe the unique voltage hysteresis phenomenon of silicon electrodes. The model correlates the voltage hysteresis of Si to its underlying phase transformation, crystallization and amorphization processes. The effects of crystallization rate and surface energy barriers are studied, unveiling the role of surface energy and particle size in determining the performance behaviors of Si.

Subsequently, a multi-material model is developed for simulating Si/Gr composite electrodes, considering different behaviors of Gr and Si. Results show that silicon introduces voltage hysteresis to Si/Gr electrodes. The (de)lithiation sequence and competing processes between Si and Gr are comprehensively studied. A dimensionless competing factor is derived to quantify the active operating regions for each material, and demonstrates to be a useful indicator to design cycling protocols for mitigating the degradation of composite electrodes.

The multi-material model is further coupled with a thermal submodel. By studying the respective heat contributions of each active material, the model reveals the origin

of thermal peaks of Si/Gr composite electrodes, which are highly related to the phase transition processes of Gr. These thermal peaks can be potentially used to detect the ageing of Si-based batteries in service.

Acknowledgement

First and foremost, I would like to express my deepest appreciation to my supervisors, Dr Huizhi Wang and Prof Gregory Offer, for their remarkable and continuous guidance, care and engagement in my PhD research. They always stay open to new ideas, and their considerable curiosity and enthusiasm inspired me a lot in discovering and exploring new research questions. I am also grateful for their invaluable encouragement and feedback at my early stage of research, without which the successful completion of research would not have been possible. Additionally, I wish to thank the Department of Mechanical Engineering and my supervisors who financed my research and life in London.

I would like to extend my sincere thanks to Dr Monica Marinescu, Dr Billy Wu, Dr Jun Jiang and Dr Jin Xuan, who generously provided their knowledge and expertise to help with this research. Words cannot express my gratitude to Dr Zhiqiang Niu for his invaluable and selfless technical support in modelling work, where he acted as my unofficial associated supervisor.

I must also thank the Electrochemical Science and Engineering group and the Faraday Institution where I gained a lot of new insights from a group of brilliant individuals. It was a truly pleasure to work in such an inspiring and cooperative environment. Special thanks should go to my past and present cohort members for their practical and friendly support. I would like to thank to Teng Zhang, Qiong, MingZhao and Simon for their expertise advice in modelling. I am also thankful to Yan, Niall, Jingyi and Xiangnan for their contributions and input in experimental support and guidance. Special mention to Weilong, Abir, Zirui, Lingding, Tino and Rob for all the great discussions and collaborations on different exciting battery modelling project.

I am extremely grateful to all my friends for their moral support and help during the Covid-19 pandemic. Special mention to Yan, Binbin, Qiong, Tianyu, Shen, MZ, Han, Tao, Xuanze, Ruihe, Ziyu and Meishan for many sharing meals and gaming weekends. I would be remiss in not mentioning my old best friends XinPeng, Zhiyao, Daijie and Wenting for their understanding and emotional support despite living thousands miles away.

Finally, I would like to express my deepest thanks to my family. To my parents and brother Xun Jiang for their unwavering support, encouragement and company throughout my years in the UK. Their belief in me has kept my spirits and motivations high during this process.

Project Outputs

ACADEMIC JOURNAL PUBLICATIONS

“Coupled Electrochemical-Thermal-Mechanical Stress Modelling in Composite Silicon/Graphite Lithium-Ion Battery Electrodes”. Mayur P. Bonkile, Yang Jiang, Niall Kirkaldy, Valentin Sulzer, Robert Timms, Huizhi Wang, Gregory Offer, Billy Wu.

“A User-Friendly Lithium Battery Simulator Based on Open-Source CFD” - Yang Jiang, Lingding Zhang, Gregory Offer, Huizhi Wang, Digital Chemical Engineering 5 (2022) 100055.

“Machine Learning Aided Predictions for Capacity Fade of Li-Ion Batteries” - N.M. Hitesh Penjuru, G. Vineeth Reddy, Manikantan R. Nair, Soumili Sahoo, Mayank, Jason Jiang, Joinal Ahmed, Huizhi Wang, Tribeni Roy, Journal of The Electrochemical Society 169 (2022) 050535.

“A Composite Electrode Model for Lithium-Ion Batteries with Silicon/Graphite Negative Electrodes” - Weilong Ai, Niall Kirkaldy, Yang Jiang, Gregory Offer, Huizhi Wang, Billy Wu, Journal of Power Sources 527 (2022) 231142.

“Insights into the Role of Silicon and Graphite in the Electrochemical Performance of Silicon/Graphite Blended Electrodes with a Multi-Material Porous Electrode Model” - Yang Jiang, Zhiqiang Niu, Gregory Offer, Jin Xuan, Huizhi Wang, Journal of The Electrochemical Society 169 (2022) 020568.

“Lithium Ion Battery Degradation: What you need to know” - Jacqueline S. Edge, Simon O'Kane, Ryan Prosser, Niall D. Kirkaldy, Anisha N. Patel, Alastair Hales, Abir Ghosh, Weilong Ai, Jingyi Chen, Jiang Yang, et al, Physical Chemistry Chemical Physics 23 (2021) 8200–8221.

“Dodecanethiol Coated Multi-Walled Carbon Nanotube Films as Flexible Current Collector for Lithium-Ion Batteries” - Xiangnan Yu, Yang Jiang, Xiao Yang, Zhaoheng Cai, Yang Hua, Shichun Yang, Huizhi Wang, Xinhua Liu, Liliang Wang, Materials Letters 291 (2021) 129508.

“‘3D+1D’ Modeling Approach toward Large-Scale PEM Fuel Cell Simulation and Partitioned Optimization Study on Flow Field” - Biao Xie, Guobin Zhang, Yang Jiang, Renfang Wang, Xia Sheng, Fuqiang Xi, Ziliang Zhao, Wenmiao Chen, Ying Zhu, Yao Wang, Huizhi Wang, Kui Jiao, ETransportation 6 (2020) 100090.

“Voltage Hysteresis Model for Silicon Electrodes for Lithium Ion Batteries, Including Multi-Step Phase Transformations” - Yang Jiang, Gregory Offer, Jun Jiang, Monica Marinescu, Huizhi Wang, Crystallization and Amorphization, Journal of The Electrochemical Society 167 (2020) 130533.

CONFERENCE PRESENTATIONS

“Multi-Scale Battery Modelling: Understanding Coupled Electrochemical and Mechanical Effects” – Billy Wu, Niall Kirkaldy, Mayur P. Bonkile, Yang Jiang, M. Naylor-Marlow, Y. Patel, Xinhua Liu, Huizhi Wang, E. Martinez-Paneda, Gregory Offer. 243rd ECS meeting with the 18th International Symposium on Solid Oxide Fuel

Cells (SOFC-XVIII). May 2023, Hynes Convention Center, Boston, Massachusetts, America..

“Silicon–Graphite Composite Electrodes: Modelling State-of-Charge and Current Distribution, and Experimentally Determining Degradation Rates”.

Niall Kirkaldy, Yang Jiang, Weilong Ai, Mohammad Amin Samieian, Zhiqiang Niu, Gregory J Offer, Jin Xuan, Monica Marinescu, Billy Wu, Huizhi Wang, Yatish Patel. ModVal 2023 - 19th Symposium on Fuel Cell and Battery Modeling and Experimental Validation. March 2023, Duisburg (Mercatorhalle), Germany.

“Modeling of the Thermal Behaviors of Silicon/Graphite Composite Electrodes for Lithium-ion Batteries” - Zirui Shao, Yang Jiang*, Gregory J Offer, Huizhi Wang. International Conference on Applied Energy. August, 2022, Bochum, Germany.

“Mechanistic Model of Lithiation and Delithiation in Silicon” - Yang Jiang, Gregory Offer, et al. “Next Generation Sustainable Batteries” IMSE online poster session, February, 2021, Institute for Molecular Science and Engineering, Imperial College London, London.

“Large-Scale Simulation of PEM Fuel Cell Using a “3D+1D” Model” - Biao Xie, Yang Jiang, et al. Society of Automotive Engineers International. 2020, Detroit, America.

POSTERS

“Model Analysis of Silicon-Based Electrodes for Lithium Ion Batteries” - Yang Jiang, Gregory Offer, Huizhi Wang. Advanced battery power conference. March 2022, Münster, Germany.

“Mechanistic Model of Lithiation and Delithiation in Silicon” - Yang Jiang, Gregory Offer, et al. “Next Generation Sustainable Batteries” IMSE online poster session, February, 2021, Institute for Molecular Science and Engineering, Imperial College London, London.

Table of Contents

Declaration of Originality	i
Copyright Declaration.....	ii
Abstract.....	iii
Acknowledgement	v
Project Outputs.....	vii
Table of Contents.....	xi
List of Figures	xv
List of Tables	xxi
List of Symbols & Acronyms	xxii
Chapter 1. Introduction.....	1
1.1. Why do we need lithium-ion batteries	1
1.2. Why use silicon-based electrodes	5
1.3. Why modelling is important	9
1.4. Thesis aim and objectives	9
1.5. Thesis structure	11
Chapter 2. Literature Review.....	14
2.1. Electrochemical behaviors of silicon	14
2.1.1. Voltage hysteresis	14
2.1.2. Two-phase lithiation and electrochemical amorphization of crystalline silicon.....	15
2.1.3. Electrochemical behaviors of lithiated amorphous Si	19
2.2. Si/Gr composite electrodes	22
2.2.1. Advantages and limitations of Si/Gr composite electrodes	22
2.2.2. Effects of Si on electrochemical behaviors of Si/Gr electrodes	23

2.2.3. Thermal behaviors of Si/Gr electrodes	27
2.3. Modelling of lithium-ion batteries	30
2.3.1. Overview of different modelling approaches	30
2.3.2. Physics-based models	32
Single particle model	34
Doyle-Fuller-Newman P2D model	36
2.3.3. Physics-based modelling of lithium-ion batteries with Si-based electrodes	40
2.4. Summary	42
Chapter 3. Modelling voltage hysteresis of silicon electrodes	44
3.1. Introduction.....	44
3.2. Reaction pathways and physical mechanisms	45
3.2.1. Reaction pathways when the lower cut-off voltage is above 0.05 V.....	45
3.2.2. Reaction pathways when the lower cut-off voltage is below 0.05 V.....	46
3.2.3. Pathway diagram.....	47
3.3. Development of voltage hysteresis model	47
3.3.1. Thermodynamics.....	47
3.3.2. Electrochemical amorphization	49
3.3.3. Charge transfer kinetics	49
3.3.4. Crystallization kinetics.....	50
3.3.5. Time evolution of species	51
3.3.6. Computational implementation and initial conditions	52
3.4. Results and discussion	54
3.4.1. Model-experiment comparisons.....	54
3.4.2. Charge/discharge behavior.....	57

3.4.3. Effect of crystallization rate.....	61
3.4.4. Amorphization with different surface energy barriers.....	63
3.5. Interim conclusion	64
Chapter 4. Modeling the role of Si in Si/Gr composite electrodes.....	66
4.1. Introduction.....	66
4.2. Multi-material electrochemical model.....	67
4.2.1. Reaction kinetics.....	69
4.2.2. Species conservation.....	71
4.2.3. Charge conservation.....	72
4.2.4. Boundary and initial conditions	73
4.2.5. Numerical procedures and model parameters.....	76
4.3. Results and discussion	76
4.3.1. Model-experiment comparison	76
4.3.2. Charge/discharge behaviors of Si/Gr electrodes with different Si/Gr ratios	78
4.3.3. Concentration and potential distributions in Si/Gr electrodes	80
4.3.4. (De)Lithiation competition between Si and Gr at different Si/Gr ratios ...	82
4.3.5. Dimensionless competing factor and its implications for strategies for mitigating Si/Gr electrode degradation.....	84
4.4. Interim conclusion	89
Chapter 5. Modelling the thermal behaviors of Si/Gr electrodes.....	91
5.1. Introduction.....	91
5.2. Electrochemical-thermal coupled multimaterial electrode model	92
5.2.1. Thermal equations and boundary conditions	92
5.2.2. Temperature dependent properties.....	93

5.2.3. Numerical procedures and model parameters.....	95
5.3. Results and discussion	95
5.3.1. Temperature variation and contribution of different heat sources.....	95
5.3.2. Effects of Si content on thermal behaviors	98
5.3.3. Thermal temporal-spatial inhomogeneity during delithiation	99
5.3.4. Thermal temporal-spatial inhomogeneity during lithiation	102
5.3.5. Effects of C rate on the thermal behaviors.....	105
5.3.6. Effects of heat transfer coefficient.....	106
5.4. Interim conclusion	107
Chapter 6. Conclusions and future works.....	109
6.1. Conclusions.....	109
6.2. Future works	112
Reference	114
Appendices.....	131
A1. Entropic coefficients	131
A2. Solution procedure of the developed battery model	133

List of Figures

Figure 1-1 Applications of LIBs [3]	1
Figure 1-2 A typical lithium-ion cell [7]. Scanning electron microscope (SEM) images of graphite anode, polyethylene (PE) electrolyte and NMC111 cathode are from referenced source [8–10].....	2
Figure 1-3 Commercialization of Lithium Battery Technologies for Electric Vehicles [7].	3
Figure 1-4 Total CO ₂ emissions of medium segment internal combustion engine (ICE) and battery electric vehicle (BEV) produced in 2020 and used for 250000 km [15]. ...	4
Figure 1-5 The average discharge potentials and specific capacity of multiple common anode materials. Reprinted (adapted) from publication [22] Copyright (2014), with permission from Elsevier.	6
Figure 1-6 Thesis structure.	11
Figure 2-1 Capacity-voltage profiles of electrodes with Gr (black) and 15 wt% amorphous Si in Gr, with cutoff potentials at 0.0 V (blue) and 0.075 V (magenta). The graphite electrode was cycled at ~C/120 rate, and the silicon-bearing electrode at ~C/140 rate, in coin cells with a Li-metal counter electrode [36].....	14
Figure 2-2 Electrochemical lithiation and delithiation curves of Si at room and high temperature. Black line: theoretical voltage curve at 450 °C. Red and green line: lithiation and delithiation of crystalline Si at room temperature, respectively [30]. ...	16
Figure 2-3 Progressive migration of the sharp amorphous/crystalline interface (ACI) during solid-state amorphization (lithiation) of a crystalline Si nanowire [44].....	17
Figure 2-4 Electrode potentials and intensities of different Bragg peaks during the (a) first discharge and (b) first charge of a crystalline Si composite electrode at C/100. The	

top panel in each figure shows the Bragg peak intensity as a function of capacity. The bottom panel shows the potential as a function of capacity [45].	18
Figure 2-5 (a) Voltage curves of a silicon electrode discharged to 0 V. (b) Voltage curves of a silicon electrode discharged to 50 mV for the first two cycles, then to 70 mV for later cycles (Reproduced from[41]).	19
Figure 2-6 The differential capacity curve (vs. electrode potential) for the charge-discharge cycle of a thin film electrode of Si [47].	21
Figure 2-7 Electrode potential and intensities of Bragg peaks during lithiation of amorphous Si at C/100 rate. The top panel in each figure shows the Bragg peak intensity as a function of capacity. The bottom panel shows the potential as a function of capacity [45].	21
Figure 2-8 Schematic of constantly built-up SEI layer on silicon surfaces [54].	23
Figure 2-9 Electrode potentials and differential capacity curves for pure graphite electrodes (as a reference) and Si/Gr composite electrodes with 15 wt% Si. (a) and (b) for lithiation, while (c) and (d) for delithiation. Electrode potentials use logarithmic scale [65][69].	25
Figure 2-10 Capacity change of Gr and Si components in the Si/Gr composite electrode containing 15wt% of Si. The circled numerals indicate different (de)lithiation regions [65].	26
Figure 2-11 Electrochemical potential curves vs. specific capacity for first eight cycles for different silicon compositions. Figure (a)-(f) refer to curves for different electrode compositions SiG00, SiG03, SiG05, SiG07, SiG10, SiG15 and SiG20 respectively. The numerals represent the silicon weight fractions in the composite electrode [70].	27
Figure 2-12 Temperature variations of a NMC-811/SiGr full cell at different ambient temperatures during (a) charge and (b) discharge [72].	28

Figure 2-13 Entropic coefficient of (a) SiGr and (b) NMC-811 electrodes [72].....29

Figure 2-14 Entropy profiling of Gr [74] and reversible heat flow of Si [75].....30

Figure 2-15 Comparison of different Li-ion battery models with respect to their computational complexity (CPU time) and predictability [76].31

Figure 2-16 Schematics of the SPM and P2D model for (a) a full cell and (b) a half cell [87].....33

Figure 3-1 Reaction pathways for electrochemical lithiation and delithiation of Si at room temperatures.45

Figure 3-2 Comparison of model predictions with the experimental data [40] for an amorphous silicon electrode operating at voltages above 0.05 V.....55

Figure 3-3 Comparison of model predictions with the experimental data [45] below 0.05 V: (a) charge/discharge curves and concentration variation of c-Li₁₅Si₄ during (b) charge and (c) discharge.56

Figure 3-4 Electrochemical behaviors and phase transformations of Si in the absence of crystallization during discharge and charge: (a) voltage curves; (b) differential voltage curves; and composition variations during (c) charge and (d) discharge.58

Figure 3-5 Electrochemical behaviors and phase transformations of Si in the presence of crystallization during discharge and charge: (a) voltage curves; (b) differential voltage curves; and composition variations during (c) charge and (d) discharge.....60

Figure 3-6 Electrochemical behaviors of Si cycled between different voltage limits: (a) current density vs time; (b) voltage vs time; (c) voltage loops.....60

Figure 3-7 The effect of crystallization rate constant on the growth of (a) crystalline phase and (b) critical nuclei during charge.62

Figure 3-8 (a) Voltage curves, (b) differential voltage curves, and molar fraction variation of (c) $c\text{-Li}_{15}\text{Si}_4$, and (d) $a\text{-Li}_x\text{Si}$ at different values of surface energy barrier during discharge.....64

Figure 4-1 Schematics of the computational domain.68

Figure 4-2 Open circuit potentials of (a) Gr and (b) Si as a function of SOC. The experimental data for Gr is taken from Ref. [35] and the experimental data for Si is taken from Ref. [120].....70

Figure 4-3 Comparison of simulated and experimental voltage curves of Si/Gr blended electrodes with different Si/Gr mass ratios ($r_{\text{Si/Gr}} = 05:90, 07:88, 10:85, 15:80$ and $20:75$) during (a) delithiation and (b) lithiation. Both the experiments and simulations run at $1/20$ C.....77

Figure 4-4 Electrochemical behaviors of Si/Gr blended electrodes with different Si/Gr mass ratios during (a) lithiation and (b) delithiation, and (c) voltage hysteresis of the Si/Gr electrodes.....79

Figure 4-5 Distributions of (a) electrolyte concentration, (b) electrolyte potential, (c) state of charge and (d) solid-phase potential across the thickness of the half-cell domain during lithiation at $r_{\text{Si/Gr}} = 0.1$81

Figure 4-6 SOC variation in Si and Gr during lithiation and delithiation of electrodes with (a) $r_{\text{Si/Gr}} = 0.1$, (b) $r_{\text{Si/Gr}} = 0.01$ and (c) $r_{\text{Si/Gr}} = 1.0$84

Figure 4-7 Competing factors as a function of electrode potential during lithiation and delithiation of electrodes with (a) $r_{\text{Si/Gr}} = 0.1$, (b) $r_{\text{Si/Gr}} = 0.01$ and (c) $r_{\text{Si/Gr}} = 1.0$86

Figure 4-8 Galvanostatic micro-cycling of the Si/Gr electrode with $r_{\text{Si/Gr}} = 0.1$: (a) voltage, (b) SOC, (c) competing factors in the first cycle and (d) competing factors in the second cycle as a function of time, and (e) capacity usage for Si and Gr during the two successive micro cycles.88

Figure 5-1 Temperature variation and electrode potential during (a) delithiation and (b) lithiation for an electrode with $r_{Si/Gr} = 0.2$ at a galvanostatic 2C delithiation condition, and $h = 1 \text{ W m}^{-1} \text{ K}^{-1}$. The heat contribution attributed to active materials is shown during (c) delithiation and (d) lithiation. Label S1 to S3 indicate the three phase transition processes of Gr.....96

Figure 5-2 Temperature variation of electrodes with different Si content during (a) lithiation (b) delithiation at a galvanostatic 2C condition, and $h = 1 \text{ W m}^{-1} \text{ K}^{-1}$98

Figure 5-3 Current density of (a) Gr and (b) Si for electrode with $r_{Si/Gr} = 0.2$ at a galvanostatic 2C delithiation condition. Label S1 to S3 indicate the three phase transition processes of Gr.....100

Figure 5-4 Ohmic heat generation of (a) working electrode and (b) separator for composite electrode with $r_{Si/Gr} = 0.2$ at a galvanostatic 2C delithiation condition. Label S1 to S3 indicate the three phase transition processes of Gr.101

Figure 5-5 Reversible heat generation of (a) Gr. and (b) Si, and irreversible heat generation of (c) Gr and (d) Si for electrode with $r_{Si/Gr} = 0.2$ at a galvanostatic 2C delithiation condition. Label S1 to S3 indicate the three phase transition processes of Gr.102

Figure 5-6 Current density of (a) Gr and (b) Si for electrode with $r_{Si/Gr} = 0.2$ at a galvanostatic 2C lithiation condition. Label S1 to S3 indicate the three phase transition processes of Gr.....103

Figure 5-7 Ohmic heat generation of (a) separator and (b) composite electrode for electrode with $r_{Si/Gr} = 0.2$ at a galvanostatic 2C lithiation condition. Label S1 to S3 indicate the three phase transition processes of Gr.....104

Figure 5-8 (a) Reversible and (b) irreversible heat generation of Gr. (c) reversible and (d) irreversible heat generation of Si for electrode with $r_{Si/Gr} = 0.2$ at a galvanostatic 2C

lithiation condition. Label S1 to S3 indicate the three phase transition processes of Gr.
..... 105

Figure 5-9 Temperature variation for the electrode with $r_{\text{Si/Gr}} = 0.2$ with a rising C-rate from 1C, 2C to 3C during (a) lithiation and (b) delithiation..... 106

Figure 5-10 Temperature variation of the electrode with $r_{\text{Si/Gr}} = 0.1$ during a (a) lithiation and (b) delithiation galvanostatic 3C condition. The ambient temperature remains a constant 298.15K with different external heat transfer rate ($h = 0, 0.1$ and $1 \text{ W m}^{-1} \text{ K}^{-1}$). 107

Figure A1-1 Evolution of entropic coefficient ($\frac{\partial E_{\text{eq,Gr}}}{\partial T}$) with state of charge during (de)lithiation for graphite electrodes. Data retrieved from Ref. [74], where θ_{Gr} is valid in the range of [0.28, 0.91] and [0.28, 0.83] during lithiation and delithiation respectively. 131

Figure A1-2 Evolution of entropic coefficient ($\frac{\partial E_{\text{eq,Si}}}{\partial T}$) with state of charge during (de)lithiation for silicon electrodes. Data retrieved from Ref. [75], where θ_{Si} is valid in the range of [0, 1] during both lithiation and delithiation..... 132

Figure A2-1 Programming flowchart of the developed battery solver. 133

List of Tables

Table 1-1 Innovators of silicon anode [31].....	8
Table 2-1. Governing equations of P2D model [87].....	37
Table 3-1 Parameter values used in base case simulations.....	53
Table 4-1 Parameter values used in base case simulations.....	75
Table 5-1 Parameter values of thermal properties.	95

List of Symbols & Acronyms

a_s	Specific surface area of active solid material particles (m^{-1})
c_{rate}	C-rate (h^{-1})
C_p	specific heat capacity ($\text{J kg}^{-1} \text{K}^{-1}$)
C_e	Electrolyte concentration (mol m^{-3})
C_s	Average lithium concentration in solid phase (mol m^{-3})
C_s^{max}	Maximum lithium concentration in solid phase (mol m^{-3})
C_s^{surf}	Lithium concentration at electrode/electrolyte interface (mol m^{-3})
C_z	Molar fraction of amorphous phase z
C_{cryst}	Molar fraction of c- $\text{Li}_{15}\text{Si}_4$
cap	Specific capacity (mAh g^{-1})
D_e	Electrolyte diffusivity ($\text{m}^2 \text{s}^{-1}$)
D_s	Diffusivity of lithium in solid phase ($\text{m}^2 \text{s}^{-1}$)
E	Electrode potential (V)
E_a	Activation energy (J mol^{-1})
E_{eq}	Equilibrium potential (V)
$E_{(j)}$	Equilibrium potential of electrochemical reaction j (V)
$E_{(j),0}$	Standard equilibrium potential of reaction j (V)
E^*	Extra potential increase induced by surface energy barrier (V)
f_{\pm}	Mean molar activity coefficient of electrolyte
F	Faraday constant (C mol^{-1})
ΔG^*	Surface energy barrier of amorphization (eV)
h	Heat transfer coefficient ($\text{W m}^{-2} \text{K}^{-1}$)
i	Reaction current density (A m^{-2})

i_0	Exchange current density (A m^{-2})
i_{app}	Applied current density (A m^{-2})
I	Total current density (A m^{-2})
j^{Li}	Volumetric current density (A m^{-3})
J	Nucleation rate (mol s^{-1})
k_0	Nucleation rate constant (m s^{-1})
k_{cryst}	Crystallization rate constant (s^{-1})
k_{react}	Rate constant ($\text{m}^{2.5} \text{mol}^{-0.5} \text{s}^{-1}$)
l	Characteristic length of active solid material particles (m)
L	Thickness (m)
$m_{\text{t,Si}}$	Total specific mass of Si (g m^{-2})
M_{Si}	Molar mass of Si (g mol^{-1})
n_s^*	Concentration of critical nuclei (mol m^{-3})
\dot{Q}	Volumetric heat generation rate (W m^{-3})
\dot{Q}^{areal}	Areal heat generation rate (W m^{-2})
$Q_{(j)}$	Total capacity obtained through reaction j (C m^{-2})
r	Particle radius (m)
$r^{\text{Si/Gr}}$	Mass ratio of Si to Gr in electrode
R	Universal gas constant ($\text{J mol}^{-1} \text{K}^{-1}$)
S	Surface area of nuclei (m^2)
t	Time (s)
t_+^0	Transference number
T	Temperature (K)
V	Electrode potential (V)

$w_{(j)}$	Interaction coefficient between neighboring ions in a host lattice
W^*	Impingement rate on the nuclei ($\text{m}^3 \text{s}^{-1}$)
$x_{(j)}$	Fraction of occupied sites through reaction j
x_{cryst}	Molar fraction of c-Li ₁₅ Si ₄
$\Delta x_{(j)}$	Fraction of the maximum inserted lithium ions through reaction j

Greek symbols

$\alpha_a \alpha_c$	Anodic and cathodic transfer coefficients
δ	Stoichiometry of super-alloyed lithium
ε_e	Volume fraction of electrolyte
ε_s	Volume fraction of active solid material
η	Overpotential (V)
λ	Thermal conductivity ($\text{W m}^{-1} \text{K}^{-1}$)
θ	State of charge (SOC)
θ^{surf}	State of charge at the surface of solid material
κ	Ionic conductivity (S m^{-1})
κ_D	Diffusion conductivity (A m^{-1})
ρ	Density (kg m^{-3})
σ	Solid phase conductivity (S m^{-1})
ϕ_e	Liquid phase potential (V)
ϕ_s	Solid phase potential (V)
χ	Competing factor

Subscripts and superscripts

0	Standard state
---	----------------

amb	Ambient
avg	Averaged
CE	Counter electrode
eff	Effective
ele	Electronic
gen	Total heat generation rate
high	Higher limit
init	Initial
ion	Ionic
irr	Irreversible heat generation rate
(j)	Reaction index
low	Lower limit
m	Material index, m = Gr, Si
ohm	Ohmic heat generation rate
ref	Reference status
rev	Reversible heat generation rate
SEP	Separator
SEP/CE	Interface between separator and counter electrode
WE	Working electrode
WE/SEP	Interface between working electrode and separator
z	Amorphous phase index

0 for a-Si, 1 for a-Li_xSi₂, 2 for a-Li₁₅Si₄, 3 for a-Li_{15+δ}Si₄

Chapter 1. Introduction

1.1. Why do we need lithium-ion batteries

The Nobel Prize in Chemistry 2019 is awarded to three scientists for the development of lithium-ion batteries (LIBs) [1]. Figure 1-1 shows the diversified applications of LIBs in three main fields including consumer electronics and devices, transportation, as well as grid energy and industry [2,3]. We all enjoy our lives with evermore ease benefiting from the use of mobile phones, laptops, cameras and vehicles which are powered by lithium-ion batteries.

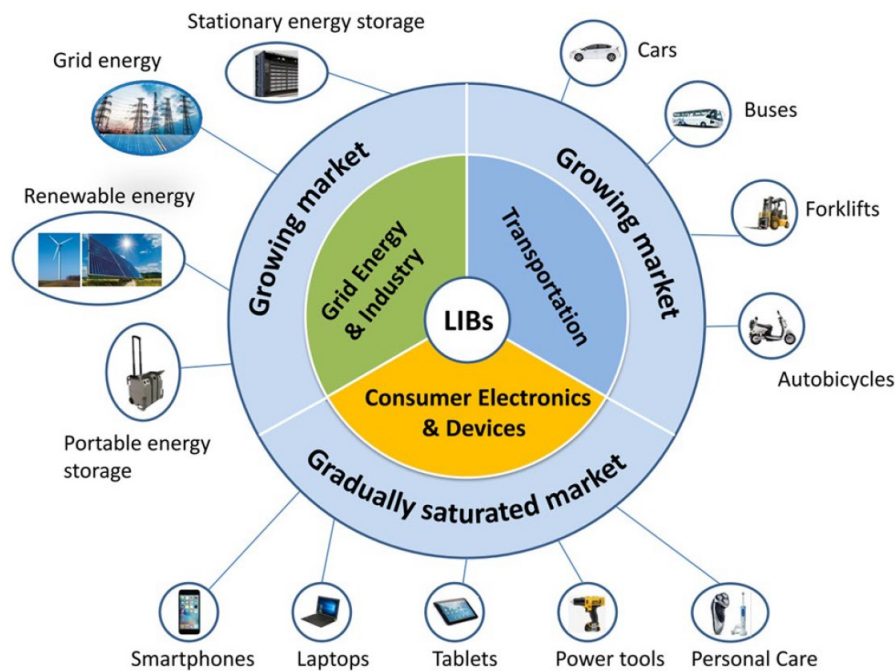


Figure 1-1 Applications of LIBs [3]

As shown in Figure 1-2, a typical lithium-ion cell consists of two porous electrodes (negative and positive electrodes) with an electrolyte-soaked separator in between. Typical negative electrode active materials include graphite, $\text{Li}_4\text{Ti}_5\text{O}_{12}$ and silicon [4], typical positive electrode active materials include transition metal oxides or phosphate active materials (LiCoO_2 , LiMn_2O_4 , $\text{LiCo}_{1/3}\text{Mn}_{1/3}\text{Ni}_{1/3}\text{O}_2$, LiFePO_4 , etc.) [5], and the electrolyte normally contains LiPF_6 salt mixed with organic carbonates such as

propylene carbonate, ethylene carbonate, dimethyl carbonate and ethyl methyl carbonate [6]. The electrodes are connected to current collectors (aluminum as the positive current collector, copper as the negative current collector) through which the electrons can be transferred to an external electric circuit. The separator, typically made of polyethylene or polypropylene, is electronically insulated and used to prevent the electrodes from coming into physical contact with each other, thus avoiding short-circuit of the cell. At the same time, the separator retains electrolyte and allows rapid ionic transport that are needed to complete the circuit during the passage of current in the lithium-ion battery.

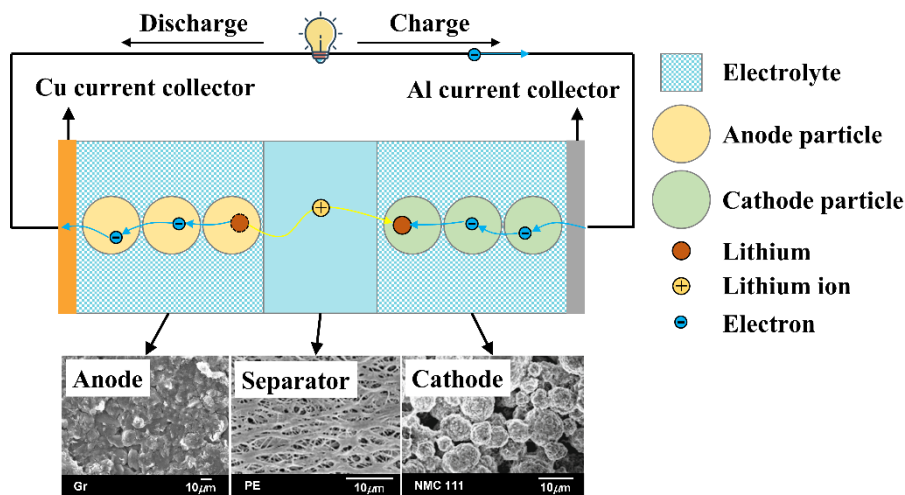


Figure 1-2 A typical lithium-ion cell [7]. Scanning electron microscope (SEM) images of graphite anode, polyethylene (PE) electrolyte and NMC111 cathode are from referenced source [8–10].

Lithium-ion batteries are now leading a great revolution in the automotive sector, and we are in the middle of a dramatic switch away from vehicles powered by fossil fuels. As shown in Figure 1-3, global lithium-ion cell manufacturing will see exponential growth in the years ahead, reaching a staggering fivefold increase to 2000 GWh in 2030 compared to 500 GWh in 2023 [7]. To date, passenger electric vehicles have surpassed electronics as the biggest user of lithium-ion batteries and they will

continuously dominate the major market in the years to come, accounting for over 70% of cell manufacturing volume in all applications in 2030 for an example.

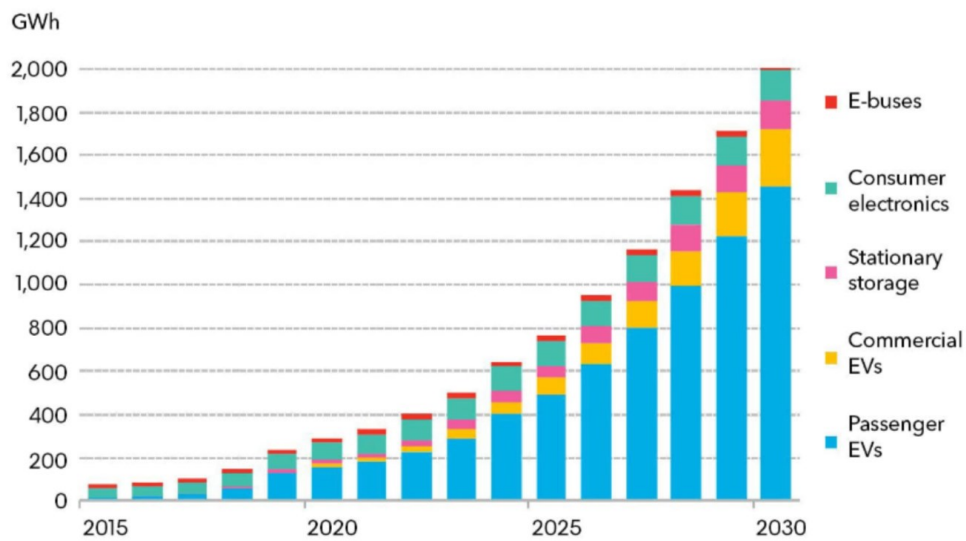


Figure 1-3 Commercialization of Lithium Battery Technologies for Electric Vehicles [7].

The rising popularity of battery-driven electric vehicles (EVs) is indicative of the growing demand for cleaner and more sustainable transportation alternatives. Conventional fossil fuel vehicles can emit pollutants, such as diesel particulate matter (PM10s), incompletely burned hydrocarbons, and nitrogen oxides (NO_x) [11]. In comparison, electric vehicles do not release harmful exhaust gases during driving, making them a practical solution to the pollution problem. Several European countries (such as the United Kingdom, France, Germany, and the Netherlands) have therefore set timetables for phasing out the production of fossil fuel vehicles [12], in response to the growing concern over the harmful effects of combustion-powered vehicles on the environment.

Electric vehicles powered by lithium-ion batteries have also become a crucial technology towards the decarbonisation in the transport sector. According to the 2021 report from the International Energy Agency (IEA) [13,14], transportation contributes

to almost one quarter of global energy-related greenhouse gas emissions. Therefore, by replacing traditional vehicles with electric alternatives, significant strides in reducing carbon footprint can be made.

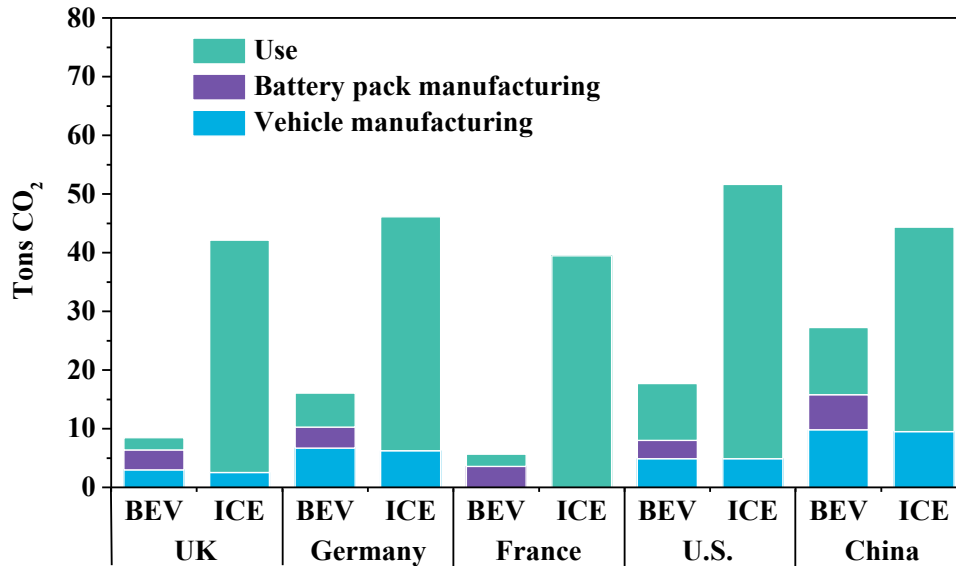


Figure 1-4 Total CO₂ emissions of medium segment internal combustion engine (ICE) and battery electric vehicle (BEV) produced in 2020 and used for 250000 km [15].

Although battery electric vehicles are not carbon-free over their whole life cycle from manufacturing to miles on the road, they release less CO₂ than that of fossil fueled vehicles. Figure 1-4 from the report [15] indicates that medium segment battery electric cars produced in 2020 and driven for 250,000 km would generate between 38% and 87% less CO₂ emissions throughout their life cycle compared to equivalent internal combustion engine vehicles in the five countries examined. The lifecycle CO₂ emissions vary from different countries depending on the energy source used to recharge batteries. For instance, electric vehicles in France, where nuclear power plants are prevalent, can reduce their carbon footprint by 87% compared to ICE vehicles. However, in China, the carbon footprint of an electric vehicle is equivalent to two-thirds of a fossil-fuel vehicle, as the electricity is mainly generated from coal-fired power stations. The proliferation of renewable energy plants worldwide is leading to an

increase in the use of renewable energy to power electric vehicles, which is further enhancing their advantages over traditional vehicles.

The commercialization of LIB-powered EVs is not built-up from zero as it benefits from the mature technology of both consumer electronics and fossil fuel vehicles. Vehicle lithium-ion batteries have already made great improvements in their energy and power through the past years, but new material inventions and designs are still required for lithium-ion batteries to win competitiveness with ICEVs in both performance and costs [7].

1.2. Why use silicon-based electrodes

Lithium-ion batteries can be evaluated on multiple metrics, including energy density, power density, safety, lifespan, and cost, which collectively determine their overall performance [16]. Of all the performance factors, energy density is among the most critical, as it directly impacts the driving range and costs of an electric vehicle.

Two critical metrics for evaluating the energy density of lithium-ion batteries are gravimetric energy density (or specific energy) and volumetric energy density. Gravimetric energy density refers to the amount of energy that can be stored per unit mass of the battery. A higher gravimetric energy density means that a battery can store more energy in the same amount of weight, which enables longer runtimes or lighter weight designs. Therefore, a higher gravimetric energy density battery can provide a longer driving range for an electric vehicle. Volumetric energy density reflects the amount of energy that can be stored per unit volume of the battery, and a higher volumetric energy density allows for smaller and more compact battery designs. Volumetric energy density is therefore important for applications where space is a limiting factor.

The United States Advanced Battery Consortium (USABC) has set a target of 500 Wh kg⁻¹ for lithium-ion batteries used in EVs, known as the Battery500 Consortium, to extend the driving range and make EVs more competitive with fossil-fueled cars [17]. This initiative of energy density target encourages innovation in developing next-generation high-energy-density batteries for future needs.

One of the important factors that can affect the energy density is the active materials used in battery electrodes and their specific capacities. Traditional vehicle lithium-ion batteries adopt carbonaceous anodes and transition metal oxides for cathodes, but the estimated limit of this type of battery is 350 Wh kg⁻¹ at the cell level [18,19], which is far less than the target. The graphite structure can accommodate only one lithium per 6 carbons (LiC₆) to a maximum extent due to its intercalation nature. Since conventional graphite-based LIBs cannot meet the high energy density demand, attention has been paid to exploiting alternative anode materials such as Li metal [20] and silicon (Si) [21].

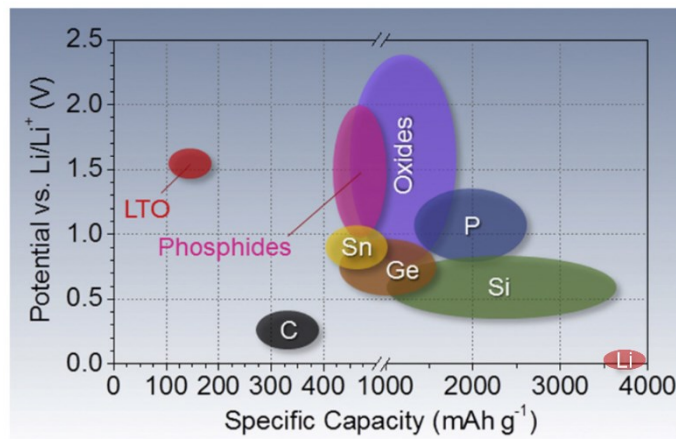


Figure 1-5 The average discharge potentials and specific capacity of multiple common anode materials. Reprinted (adapted) from publication [22] Copyright (2014), with permission from Elsevier.

Figure 1-5 shows the respective discharge potentials and specific capacity that can be achieved by different anode materials, where Li metal and silicon have the highest





































theoretical specific storage capacities. Li metal is a promising anode candidate due to its ultrahigh theoretical specific capacity of 3862 mAh g^{-1} . However, Li metal batteries have been plagued by several notorious issues, including dendrite formation, lithium corrosion, dead lithium, and volume expansion [20]. These problems cause severe capacity loss and even pose safety hazards after long periods of operation. Although the use of artificial SEI [23], solid electrolytes [24], and 3D anode hosts [25] has somewhat mitigated these issues, there is still a significant gap between current lithium metal batteries and their commercial viability.

Silicon is another promising alternative material to carbon and it has an impressive gravimetric capacity that can reach up to 3579 mAh g^{-1} , which is about 10 times larger than that of carbonaceous materials (372 mAh g^{-1}) [22,26]. In addition, silicon has a relatively low average potential of around $0.5 \text{ V vs. Li/Li}^+$, which is comparable to carbon [22]. Since the gravimetric energy density is the product of specific capacity and electrode potential, the ideal gravimetric energy density of Si could be approximately 10 times larger than carbon, offering a promising avenue for high-energy density batteries. It is estimated that the full lithiation of Si results in the specific and volumetric capacity of about 3600 mAh g^{-1} and 2194 Ah L^{-1} respectively [27,28], which is more than sufficient compared to the targeted energy density at an electrode level. In addition to the high energy density, silicon is also the second most abundant element in the earth's crust, with environmental benignity [29]. Moreover, the processing and production of Si have been well developed in the semiconductor sector with a large and mature infrastructure [30]. These favorable characteristics assure low costs of both materials and manufacturing for silicon-based batteries.

Owing to these advantages over traditional carbonaceous materials, silicon has now become a popular research topic with a surge of a five-fold increase in publications

over the past decade. In addition, the innovators of silicon anodes are making significant strides, with a host of companies like Sila, Enovix, and Enevate at the forefront of this technology. These companies have raised a total of over \$2000 million (about £1850 million) in funding, as highlighted in Table 1-1 below, which provides a non-exhaustive list of their primary technologies.

Table 1-1 Innovators of silicon anode [31].

Company	Main Technology	Tot. Funding	Partnerships/Investments
 SILA	Si nanocomposite	\$930M	    
 ENOVIX	3D Si architecture	\$254M	 
 ENEVATE	Si porous film	\$192M	  
 StoreDot	Si nanoparticles	\$172M	     
 nexeon	Si porous columns	£130M	 
 OneD	Si nanowires on graphite	\$125M	Financial VCs
 amplus	Si nanowires	\$191M	 
 ADVANO	Si nanoparticles	\$38.8M	
 GROUP14	Si/C nanocomposite	\$41.5M	    
 LeydenJar	Si nanopillars	£33.2M	Financial VCs

Despite the extremely high lithium storage capacity of silicon materials, a significant volume expansion (up to 280%) of silicon-based electrodes occurs during lithium insertion, leading to negative effects such as cracking and loss of electric contact between neighboring particles and conductive additives. The cracked surface on Si can further lead to the constant buildup of the solid electrolyte interface (SEI),

which not only increases the electrode impedance, but also reduces the effective lithium inventory and causes capacity fade. As a result, the service life of silicon-based lithium-ion batteries is seriously reduced. New understandings and technologies need to be developed to address these limitations.

1.3. Why modelling is important

Mathematical modelling has long been used as a crucial tool complementary to experimental in battery research. The major advantage of mathematical modelling over experimental tests is that it is cheaper, safer, and faster to run [32]. Computational modelling also enables an easy analysis of the internal status of a battery such as concentration and temperature distributions which experiments can hardly measure. Furthermore, modelling provides the ability to extrapolate beyond the range of experimental tests, and therefore allows simulating and testing of many more hypotheses than an experiment can do with equivalent resources [32,33]. The benefits of modelling make it widely used in various applications such as battery control, design, online prediction and diagnosis. However, most of the existing battery models are developed for graphite electrodes, there lacks a suitable modelling tool for silicon-based electrodes.

1.4. Thesis aim and objectives

The rapid growth of the electric vehicle market necessitates the development of high-energy-density lithium-ion batteries to enable extended driving range. A promising way is to use silicon-based anode in lithium-ion batteries, which can increase the theoretical energy density by nearly 10 times at an electrode level compared to the existing carbon-based electrodes. However, the dramatic volume change and consequent cracking of Si heavily reduces its lifespan. Moreover, the thermal characteristics and safety issues related to Si-based electrodes are not yet fully

understood. Battery models have proven to be useful tools to guide for effective battery design and management, which can enhance battery performance and cycle life to a certain extent. However, most of the existing battery models are developed for graphite electrodes, there lacks a suitable modelling tool for silicon-based electrodes. As an alloying material, silicon exhibits distinct electrochemical and thermal properties and behaviors compared to the intercalation carbon-based materials. The overall aim of the PhD thesis is therefore to develop physics-based fundamental modelling tools for silicon-based electrodes. These tools are able to describe and predict the electrochemical and thermal behaviors of LIBs with Si-based electrodes, as well as provide guidance for their design and optimization. The specific objectives are:

(1) Exploring the mechanisms behind the hysteresis unique to silicon materials and developing a model to correlate this voltage hysteresis phenomenon to the phase changes and crystallization of Li-Si phases.

(2) Developing an electrochemical model for Si/Gr composite electrodes which is capable of differentiating the contributions of each active material to the overall electrode performance. This model will serve as a valuable tool for analyzing the individual effects of each active material and guiding the optimization of Si/Gr composite electrodes.

(3) Integrating the thermal sub-model to the electrochemical model for Si/Gr electrodes. Specifically, the respective thermal characteristics and behaviors of Si and Gr will be considered, as well as their combined effects on the overall thermal behaviors. Additionally, the impact of design parameters (such as silicon content), working conditions (such as c-rates), and external heat transfer coefficients on the electrode thermal behaviors will be investigated.

1.5. Thesis structure

The thesis progresses by conducting a comprehensive review of literature to pinpoint the research gaps, and then developing modeling techniques in a roughly sequential manner to address the research aim and objectives.

The structure of the thesis and linkages between each chapter are illustrated in the following figure.

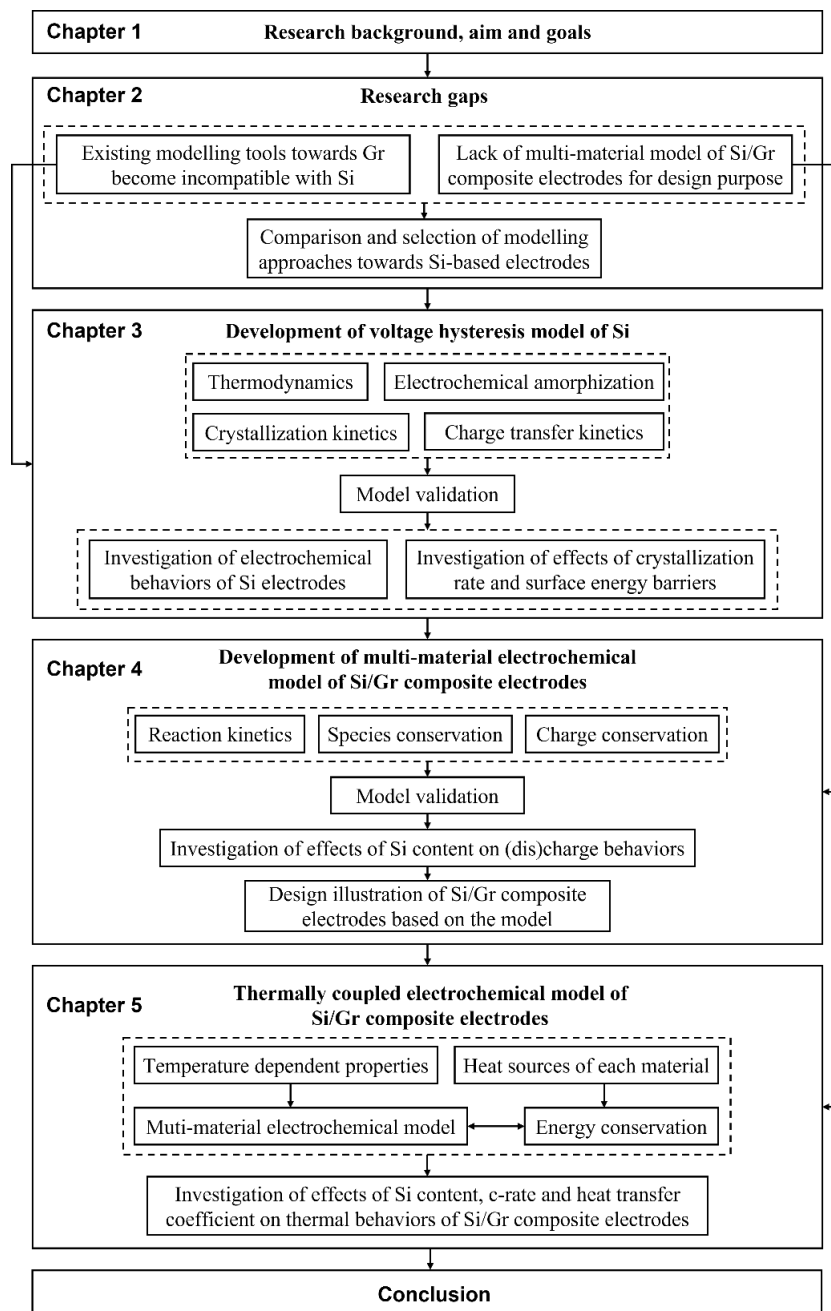


Figure 1-6 Thesis structure.

Chapter 1: Introduction

- Introduction of the context surrounding silicon-based lithium-ion batteries and the imperative to create novel modeling tools for these types of batteries. Additionally, outline the main objectives and fundamental research questions of the thesis.

Chapter 2: Literature reviews

- A focused literature review on the unique electrochemical and thermal behaviors of Si and Si/Gr composite electrodes exclusive to conventional carbonaceous electrodes.
- Overview of the commonly used physics-based modelling approaches of batteries and their basic frameworks.

Chapter 3: Modelling voltage hysteresis of silicon electrodes

- Develop a novel model that integrates thermodynamic and kinetic theories of electrochemical reactions, as well as crystallization and amorphization phenomena.
- Perform quantitative comparisons between simulation outcomes and experimental data.
- Based on the model, explain the underlying mechanism of electrochemical voltage hysteresis of Si and investigate the effects of crystallization rate and surface energy barriers.

Chapter 4: Modeling the role of Si in Si/Gr composite electrodes

- Build a multi-material model framework for Si/Gr composite electrodes, which accounts for the distinct kinetic characteristics of each active material.
- Utilize this model to demonstrate the impact of silicon content on the electrochemical performance of these composite electrodes.

- Present a strategy for designing and optimizing the cycling protocol of these composite electrodes to potentially mitigate their degradation.

Chapter 5: Modelling the thermal behaviors of Si/Gr electrodes

- Integrate a thermal sub-model into the electrochemical model of Si/Gr electrodes, taking into account the distinct thermal properties of each material.
- Explore the origin of the thermal peaks and their correlation with the phase transitions of Gr.
- Demonstrate the capabilities of this model in analyzing the impacts of silicon content, c-rates, and external heat transfer coefficients on the thermal behaviors of Si/Gr electrodes.

Chapter 2. Literature Review

2.1. Electrochemical behaviors of silicon

2.1.1. Voltage hysteresis

In contrast to conventional carbonaceous materials, silicon has many unique behaviors, among which voltage hysteresis phenomenon is a most well-known one. As shown in Figure 2-1, the voltage hysteresis appears as voltage difference between charge and discharge voltage curves for both Gr and Si containing electrodes and it sustains even at a very small c-rate. As a kind of intercalation material, Gr displays three observable voltage plateaus during charge and discharge, corresponding to the staging processes of Gr [34,35]. Although the charge and discharge voltage curves of Gr do not converge exactly at the same value, the voltage difference is less than 0.02V. Thereby, the open circuit potential for Gr is normally considered as reversible during cycling.

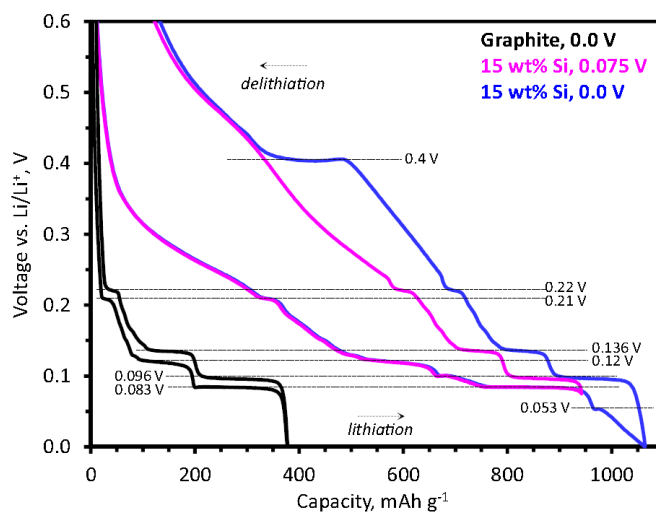


Figure 2-1 Capacity-voltage profiles of electrodes with Gr (black) and 15 wt% amorphous Si in Gr, with cutoff potentials at 0.0 V (blue) and 0.075 V (magenta). The graphite electrode was cycled at $\sim C/120$ rate, and the silicon-bearing electrode at $\sim C/140$ rate, in coin cells with a Li-metal counter electrode [36].

Compared to pure Gr, the existence of only 15 wt% silicon additives can significantly enlarge the voltage gap between charge and discharge curves to a maximum of around 0.3 V especially at the low-capacity region. More interestingly, the residual hysteresis of silicon-based electrodes appears to be path dependent in Figure 2-1, where the delithiation voltage branches of silicon containing electrodes at different lithiation depths cannot overlap. In addition, comparing to the magenta curves with cutoff potential at 0.075 V, the blue curves display another short new lithiation voltage plateau at around 0.053 V as well as a new broad plateau at 0.4 V on the reverse voltage branch if the lithiation voltage drops to 0 V.

Unlike Gr, silicon is an alloying material and thus its unique electrochemical phenomena cannot be translated by the previously known mechanisms of Gr. To better comprehend the unique voltage hysteresis of Si, it is necessary to understand how pure silicon electrodes perform during electrochemical cycling and what underlying mechanisms result in these new features. In the following sections, studies on the lithiation and amorphization of crystalline Si, as well as electrochemical behaviors of amorphous Si will be presented.

2.1.2. Two-phase lithiation and electrochemical amorphization of crystalline silicon

Crystalline Si has been widely utilized as the active material in electrochemical tests. Early studies [37–39] found that the crystalline Si (c-Si) can form successive crystalline Li-Si compounds during equilibrium Coulometric titration experiments at a temperature of 450 °C. As shown by the black line in Figure 2-2, the intermediate reaction crystalline products upon lithiation are $\text{Li}_{12}\text{Si}_7$, Li_7Si_3 , $\text{Li}_{13}\text{Si}_4$ and $\text{Li}_{22}\text{Si}_5$ with respective onset potentials of 332, 288, 158 and 44 mV, displaying stepped voltage profiles within each phase transformation process [30]. The voltage profile and reaction phases remain the same during the corresponding delithiation process.

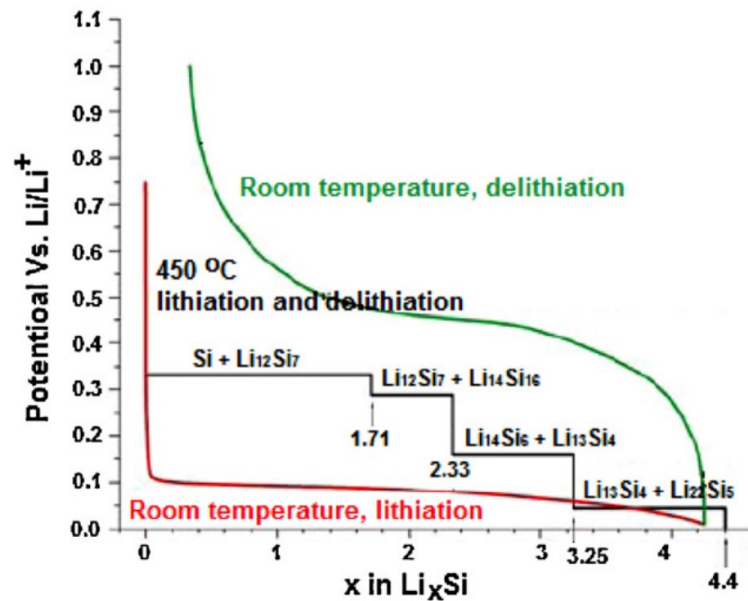


Figure 2-2 Electrochemical lithiation and delithiation curves of Si at room and high temperature. Black line: theoretical voltage curve at 450 °C. Red and green line: lithiation and delithiation of crystalline Si at room temperature, respectively [30].

However, these equilibrium phases appear kinetically hindered during electrochemical cycling at room temperature. Instead, room temperature lithiation of crystalline Si involves an electrochemical solid-phase amorphization which leads to the formation of a metastable amorphous Li-Si phase (denoted as a- Li_xSi , $x \sim 3.4 \pm 0.2$). Figure 2-2 shows the amorphization process featured a broad flat voltage plateau at around 0.1 V (vs. Li/Li^+) [40,41] during the initial lithiation. In the reverse process, the terminal composition Li_xSi undergoes another amorphization process showing a wide voltage plateau at around 0.4V. Previous studies proposed that the amorphization of crystalline Si occurs because the metastable amorphous Li-Si intermediate phases have lower free energy (less negative) compared to the equilibrium crystalline phases [42].

The two-phase amorphization phenomenon at room temperature between the a- Li_xSi and c-Si have been captured experimentally using scanning electron microscopy (SEM) [43] and high-resolution transmission electron microscopy (TEM) [44]. Clear

phase boundary between a-Li_xSi/c-Si was imaged in Figure 2-3, where the progressive migration of the amorphous/crystalline interface (ACI) follows a layer-by-layer peeling-off mechanism (or ledge mechanism) during lithiation. As a result, the amorphous phase region grew and thickened with a grey contrast, while the ACI (in a darker striped contrast) did not change much in thickness (~1 nm).

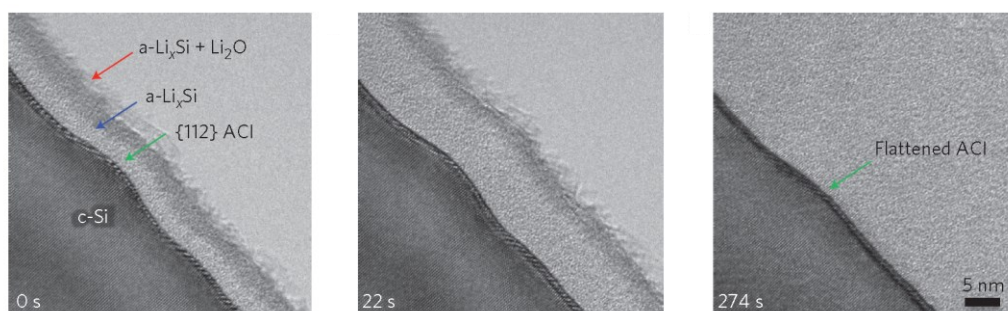


Figure 2-3 Progressive migration of the sharp amorphous/crystalline interface (ACI) during solid-state amorphization (lithiation) of a crystalline Si nanowire [44].

The amorphization process of c-Si at room temperature has also been investigated using in situ X-ray diffraction (XRD) techniques [45]. Figure 2-4 (a) shows that during the first discharge, the Bragg peaks of Si(111) and Si(220) decline linearly with cell capacity, corresponding to the solid amorphization process of c-Si. The coexistence of crystalline Si and amorphous Li_xSi phase proceeds over the whole voltage plateau at around 0.1 V (vs. Li⁺/Li) until capacity reaching about 3350 mAh g⁻¹ [45]. Surprisingly, a new crystalline Li-Si phase (i.e. c-Li₁₅Si₄) appears abruptly once the discharge potential drops below ~60 mV, with a set of Bragg peaks occurring within a narrow capacity range. This recrystallization phenomenon explains the appearance of the short lithiation voltage plateau at 0.053 V for the highly lithiated Si containing electrode in Figure 2-1.

Figure 2-4 (b) shows that the intensities of Li₁₅Si₄(332) and Li₁₅Si₄(431) decrease linearly with cell capacity, indicative of the amorphization of this newly formed

crystalline Li-Si phase. Interestingly, a wide flat plateau at about 0.4 V appears as lithium atoms extract from the Li-Si phases, and the voltage plateau shown here is highly consistent with the one exhibited in the delithiation voltage branch in Figure 2-1.

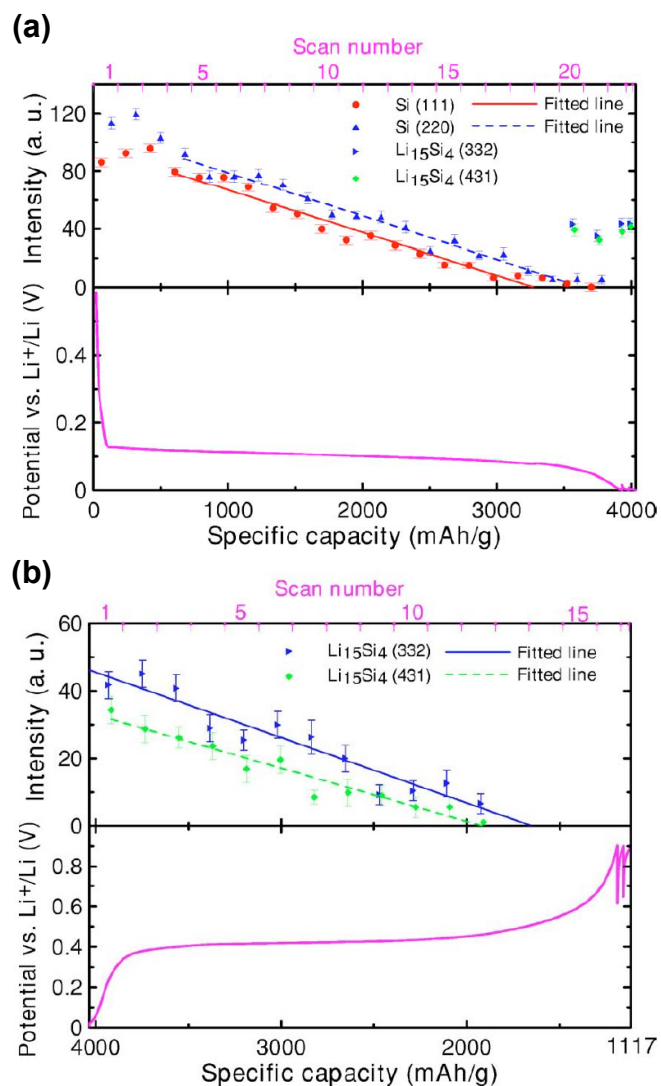


Figure 2-4 Electrode potentials and intensities of different Bragg peaks during the (a) first discharge and (b) first charge of a crystalline Si composite electrode at C/100. The top panel in each figure shows the Bragg peak intensity as a function of capacity. The bottom panel shows the potential as a function of capacity [45].

So far, the XRD experimental results of crystalline Si have indicated that the appearance of new voltage plateaus on voltage curves for silicon-containing electrodes should correspond to the two-phase transformation between a-Li_xSi and c-Li₁₅Si₄.

However, during a long-term cycling at room temperature, the crystalline Si will transform to be amorphous and this process is irreversible [46]. Hence, understanding the electrochemical behaviors of amorphous Si has more implications in battery applications. What's more, the path-dependent voltage hysteresis as discussed in section 2.1.1 (Figure 2-1) is also associated with the behaviors of amorphous Si, thus obtaining a basic knowledge of the features for amorphous Si is necessary.

2.1.3. Electrochemical behaviors of lithiated amorphous Si

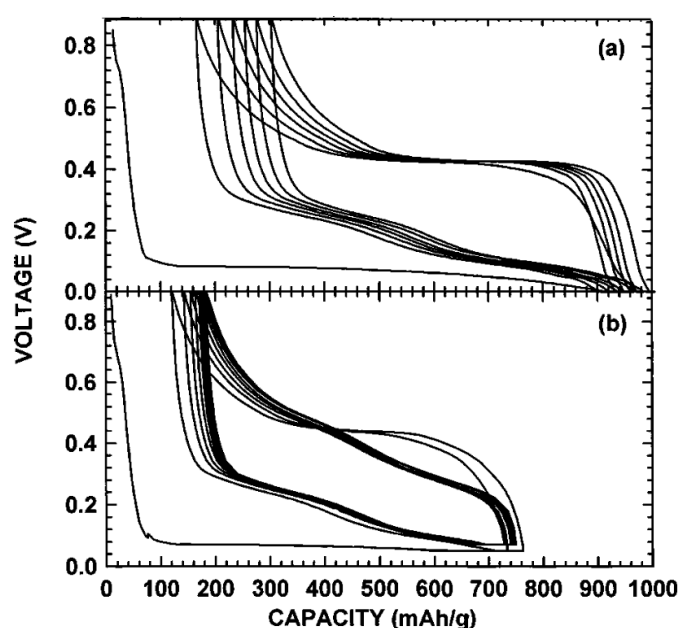


Figure 2-5 (a) Voltage curves of a silicon electrode discharged to 0 V. (b) Voltage curves of a silicon electrode discharged to 50 mV for the first two cycles, then to 70 mV for later cycles (Reproduced from[41]).

Figure 2-5 shows voltage curves in successive cycles of amorphous Si after crystalline Si becomes amorphous in the first lithiation. In contrast to the lithiation of crystalline Si, no significant voltage plateau appears in the lithiation curve of the amorphous Si. Instead, sloping-shaped [40] curves were observed in the lithiation voltage branch with two quasi-plateaus in both Figure 2-5(a) and (b).

Figure 2-5(b) shows that the electrochemical behaviors of amorphous silicon electrodes depend on lithiation depth [45]. The charge and discharge voltage curves were found to be round shaped without any distinct voltage plateau when the lower cut-off voltage was 70 mV. However, further alloying silicon electrodes to below 50 mV would lead to a single wide voltage plateau at about 0.4 V in their delithiation process, resulting in an asymmetric voltage hysteresis.

Figure 2-6 shows a typical differential capacity curve for (de)lithiation of amorphous Si without crystallization. Differential capacity [47] or cyclic voltammetry [48] approaches were commonly used to investigate the reduction and oxidation processes, as well as the active material phase transformations during cycling of batteries. Two broad peaks are observed in both the charge and discharge regimes corresponding to the two quasi-plateaus displayed in the sloping voltage curves in Figure 2-5(b). In the cathodic branch (Li alloy) the two peaks distribute at $\sim 0.06\text{V}$ (Aa) and $\sim 0.25\text{V}$ (Ab) responsible for lithiation from amorphous Si to Li-Si amorphous phases. In the reverse process, two peak potentials at $\sim 0.3\text{V}$ (Da) and $\sim 0.5\text{V}$ (Db) are shown, implying two underlying structural changes. However, these structural changes have not been clearly identified due to the amorphous nature of those Li-Si phases [47], in which case the diffraction technique is not available. Instead, first principle simulations and nuclear magnetic resonance (NMR) experiments [49,50] have been carried out and found that the amorphous structural changes might be attributed to short-range ordering in the amorphous Li-Si structures, where silicon atoms are well dispersed and mostly surrounded by Li atoms.

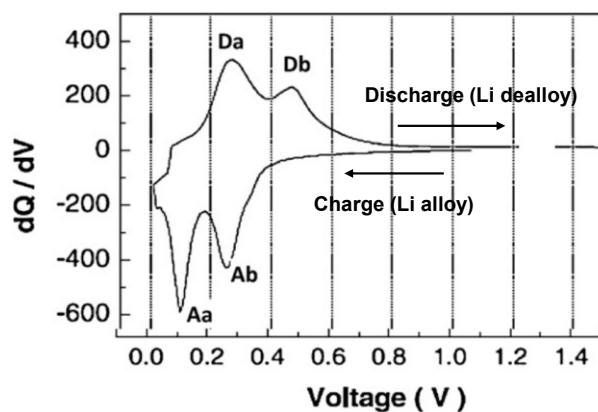


Figure 2-6 The differential capacity curve (vs. electrode potential) for the charge-discharge cycle of a thin film electrode of Si [47].

Using in situ X-ray diffraction, Li and Dahn [45] showed the whole recrystallization process of amorphous Si in Figure 2-7 with crystalline $\text{Li}_{15}\text{Si}_4$ emerging quickly at the end of discharge.

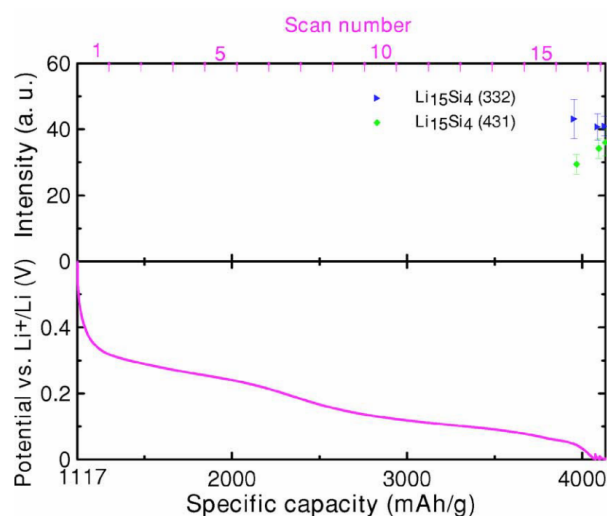


Figure 2-7 Electrode potential and intensities of Bragg peaks during lithiation of amorphous Si at C/100 rate. The top panel in each figure shows the Bragg peak intensity as a function of capacity. The bottom panel shows the potential as a function of capacity [45].

Together with the XRD results shown in Figure 2-4, it is clear to see that the asymmetric voltage hysteresis is highly associated to the formation of c- $\text{Li}_{15}\text{Si}_4$ which results in the single wide plateau at ~ 0.4 V in the delithiation curves during its two-

phase amorphization process. When the lower cut-off voltage was higher than 0.05 V, the formation of $\text{Li}_{15}\text{Si}_4$ was avoided and only a solid-solution reaction happened [45], thereby giving a sloping voltage curve.

The size of silicon particles was also found to affect the voltage hysteresis behaviors. Using Si/C composite electrodes made of silicon powders, Saint et al. [51] found that electrodes with micron-sized Si (1-10 μm) exhibited flat delithiation voltage curves with a voltage plateau at ~ 0.4 V, while those with nanosized Si (10-100 nm) showed sloping curves even if fully lithiated to 0 V [51]. Interestingly, when the Si particle size was reduced to less than 20 nm, even the flat voltage plateau in the first lithiation process became a sloping shape [42,52]. Zhang [42] proposed a qualitative explanation that the crystallization of small silicon particles might be hindered due to the additional interface energies required for the nucleation, but quantitative studies on this phenomenon still lack.

2.2. Si/Gr composite electrodes

2.2.1. Advantages and limitations of Si/Gr composite electrodes

Though silicon (Si) delivers an impressively high theoretical specific capacity of 3579 mAh g^{-1} (for $\text{Li}_{3.75}\text{Si}$) [29], which is approximately 10 times that of the traditional graphite electrode, the use of Si in lithium-ion batteries has been hindered by its poor cycle life [53]. The cycle life of pure silicon electrodes made of coarse particles (micrometer) is limited to be roughly 20 cycles [54]. Different from the commonly used carbonaceous negative electrodes which have relatively stable structures during cycling, Si-based electrodes will undergo an alloy reaction [26] which involves breaking the bonds between host atoms, thus resulting in dramatic structural changes and low capacity retention [55]. A large volume change of up to 280 vol% for the highest lithiated silicon phase ($\text{Li}_{15}\text{Si}_4$) were observed during cycling of silicon electrodes at

room temperature, compared with a much smaller volume change of Gr (10 vol%) [40,56]. This dramatic increase in size induces stress in electrodes and exacerbates the particle fracture effect, to the extent that the initial thin passivation layer, namely the solid electrolyte interface (SEI), cracks during contraction of a solid silicon particle and new SEI forms on the exposed surfaces, resulting in a very thick SEI layer after many cycles [54,57]. Figure 2-8 below illustrates the schematic of constantly built-up SEI layer on silicon surfaces.

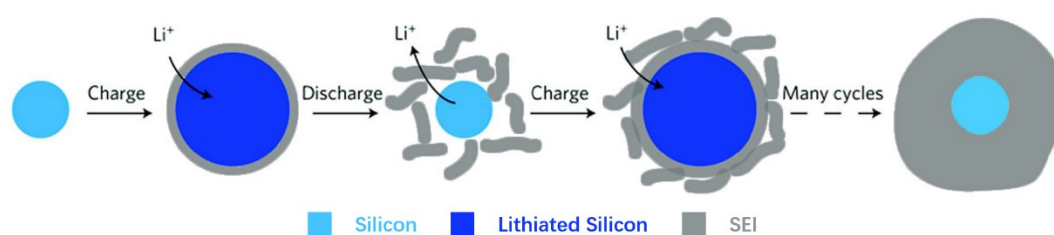


Figure 2-8 Schematic of constantly built-up SEI layer on silicon surfaces [54].

To better adapt to commercial needs, tremendous efforts have been made to optimize silicon anode. Among all strategies, developing blended electrodes with a mixture of Si and Gr has become a viable compromise between energy density, cost and cycle life [58–60]. Although pure silicon electrodes typically degrade within a few hundred cycles [61], it is claimed that the Gr in a blended electrode serves as a buffering matrix to volume changes of Si, thereby reducing mechanical fade and improving electrode integrity [62]. The carbonaceous matrix can also enhance the electrode conductivity [62]. As a result, some cutting-edge Si/Gr composite electrodes can reach over 500 mAh g⁻¹ of specific capacity and over 600 Wh kg⁻¹ of energy density, with an incredibly improved lifetime of hundreds of cycles or more [63,64].

2.2.2. Effects of Si on electrochemical behaviors of Si/Gr electrodes

Since both Si and Gr can electrochemically react with the lithium-ions during cycling, the electrochemical behaviors of Si/Gr composite electrodes are subject to

contributions from both materials. As Si has entirely different characteristics from Gr in electrochemical lithiation/delithiation [54], it brings about new features to the overall performance of composite electrodes compared to pure Gr electrodes. This section will introduce what role silicon plays in the behaviors of Si/Gr composite electrodes in terms of the electrochemical and thermal characteristics.

The active voltage range of Si is known to be between 0-1 V during the electrochemical cycling, whereas that of Gr is mainly below about 0.25 V [36,41]. In order to understand how the relative (de)lithiation of Si and Gr behaves in a blended electrode, Yao et al. [65] conducted in-operando measurements of Si/Gr electrodes containing 15wt% Si with energy dispersive X-ray diffraction (EDXRD), where a reaction competition between Si and Gr was revealed during electrode cycling. In Figure 2-9, cycling of Si/Gr electrodes is shown to lead to three graphite potential plateaus on a sloped Si voltage curve during both lithiation and delithiation. Compared with the potential curve of pure graphite electrode, the three plateaus of Gr still appear in the potential curves of the composite electrodes at nearly the same potential levels, but the addition of Si weakens this feature as shown by the lower peaks in the differential capacity curves in Figure 2-9 (b) and (d). The two sloping plateaus of Si is captured in the lithiation curve with two dQ/dV peaks Si1 and Si2, and one another silicon plateau Si3 occurs at $\sim 0.4V$ in the reverse process referring to the solid amorphization of $c\text{-Li}_{15}\text{Si}_4$. The charge/discharge behaviors of Si/Gr electrodes with other types of structures have also been extensively studied experimentally [66–68], and all exhibit similar electrochemical voltage curves featured by a superposition of both the contribution of Gr and Si.

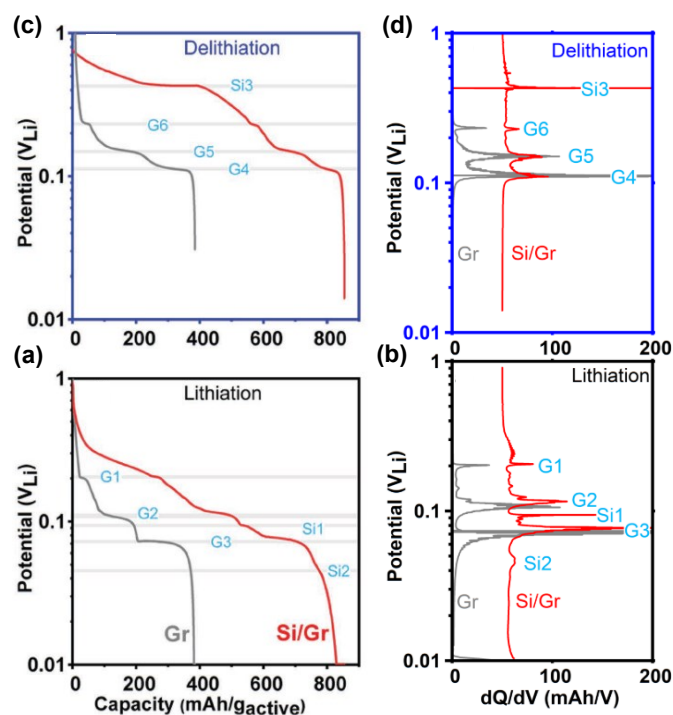


Figure 2-9 Electrode potentials and differential capacity curves for pure graphite electrodes (as a reference) and Si/Gr composite electrodes with 15 wt% Si. (a) and (b) for lithiation, while (c) and (d) for delithiation. Electrode potentials use logarithmic scale [65][69].

The huge voltage hysteresis of Si implies different electrochemically active potential regions of Si during Li insertion and extraction, which consequently results in asymmetric lithiation and delithiation processes of Si/Gr composite electrodes. Based on the in-operando measurements [65], the lithiation began with alloying with Si in region ① shown in Figure 2-10, and lithiation of Gr only occurred at voltages below 0.2 V mainly in region ②. In contrast, the delithiation occurred sequentially first from Gr and then Si, corresponding to the region ③ and ④ respectively in Figure 2-10.

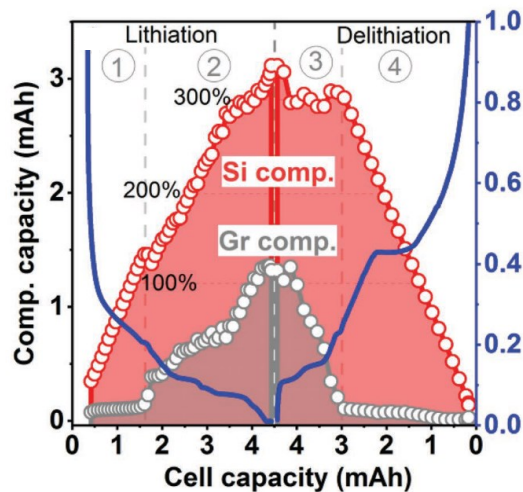


Figure 2-10 Capacity change of Gr and Si components in the Si/Gr composite electrode containing 15wt% of Si. The circled numerals indicate different (de)lithiation regions [65].

The presence of Si also introduces voltage hysteresis in Si/Gr composite electrodes, where silicon content has demonstrated to be an important influence factor. Figure 2-11 [70] shows the electrochemical voltage curves of Si/Gr composite electrodes with different silicon fractions. An elevated silicon content introduces larger voltage difference between charge and discharge curves, and more hysteresis appears. In addition, an increasing silicon content can level up the specific capacity remarkably from less than $400 \text{ mAh g}_{\text{AM}}^{-1}$ (SiG00) to over $1000 \text{ mAh g}_{\text{AM}}^{-1}$ (SiG20) for the beginning of life of the composite electrodes. However, higher relative capacity loss is observed with higher silicon fraction, indicating that silicon additives can accelerate the decay of the composite electrodes.

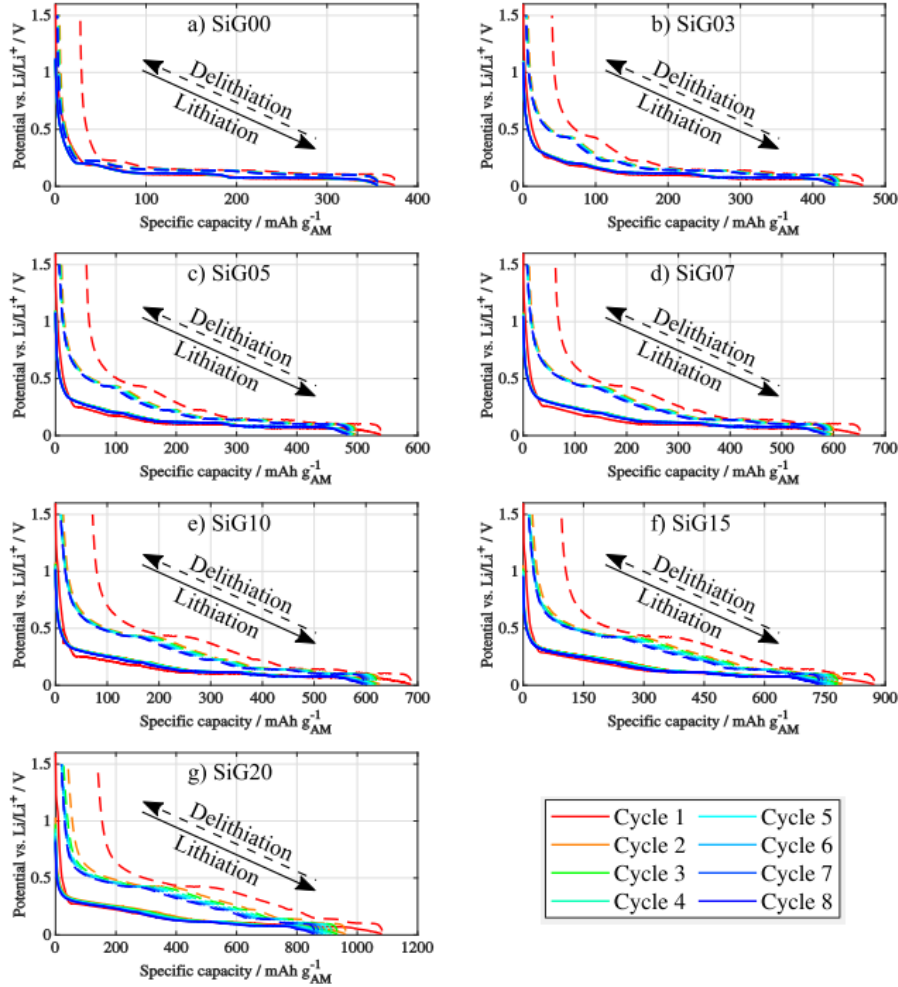


Figure 2-11 Electrochemical potential curves vs. specific capacity for first eight cycles for different silicon compositions. Figure (a)-(f) refer to curves for different electrode compositions SiG00, SiG03, SiG05, SiG07, SiG10, SiG15 and SiG20 respectively. The numerals represent the silicon weight fractions in the composite electrode [70].

In conclusion, the electrochemical characteristics of Si/Gr composite electrodes appear as a complicated convolution of the effects of both Si and Gr, implying that each active material in a composite cannot be considered independent from one another in studying the overall electrochemical behaviors.

2.2.3. Thermal behaviors of Si/Gr electrodes

In addition to the electrochemical characteristics, investigating the thermal behaviors of Si/Gr composite electrodes is important especially for such high energy

density electrodes which may release a larger amount of heat during battery operation than traditional graphite electrodes. The optimal operating temperature interval is 15-35°C, while exposing batteries at abnormal operating temperature can exacerbate battery degradation and even trigger safety issues such as thermal abuse and fire hazard [71].

The thermal behaviors of Si/Gr electrodes can be different from Gr electrodes in that the thermal and chemical properties of Si are different in terms of thermal conductivity, entropy profiling and solid phase conductivity, etc. However, so far there is rare studies on thermal analysis of the Si/Gr composite anode at an electrode level, while most relevant studies focus on a silicon-based full cell paired with high energy density NMC cathode. Sturm et al. [72] measured the heat flux and temperature variations of a high-energy 18650 NMC-811/SiGr lithium-ion batteries during (dis)charge by using infrared thermography and calorimetry.

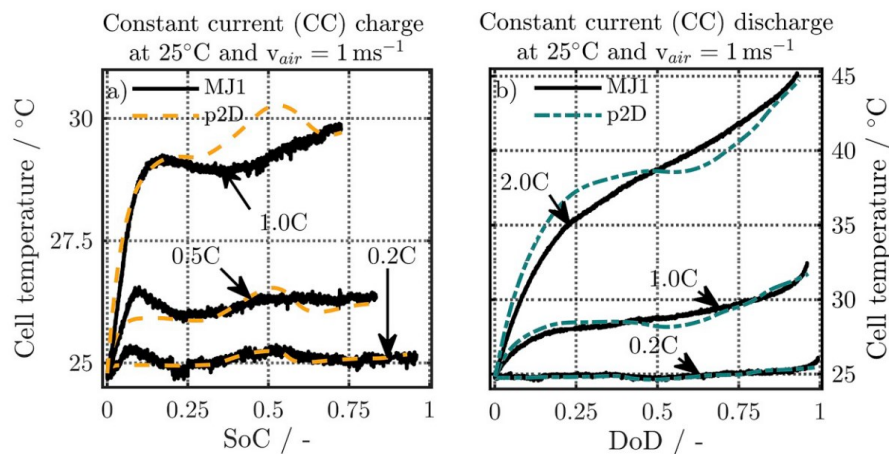


Figure 2-12 Temperature variations of a NMC-811/SiGr full cell at different ambient temperatures during (a) charge and (b) discharge [72].

As shown in Figure 2-12, several thermal peaks were observed in both the temperature and heat flow curves during both charge and discharge. However, this feature was not mentioned and analyzed in this study. Although the modelling results show good consistency with experimental results, the model is largely limited to

analyzing thermal behaviors of a given battery compositions since it only considers each electrode as a single lumped material.

In Figure 2-13, the entropic coefficients of both Si/Gr and NMC electrodes provide evidence of the emerging thermal peaks. Several observable peaks appear in the entropy profiling of Si/Gr electrodes, while the cathode NMC electrode only presents a flat entropy profiling. It is therefore reasonable to speculate that the thermal peaks of this full cell only derive from the reversible heat generation of the anode Si/Gr electrode, which highly relies on the entropy variation of the electrode materials. Malgorzata et al. [73] found similar peaks in the entropy profiling of Si/Gr electrodes which they believed were attributed to be the structural changes of Gr.

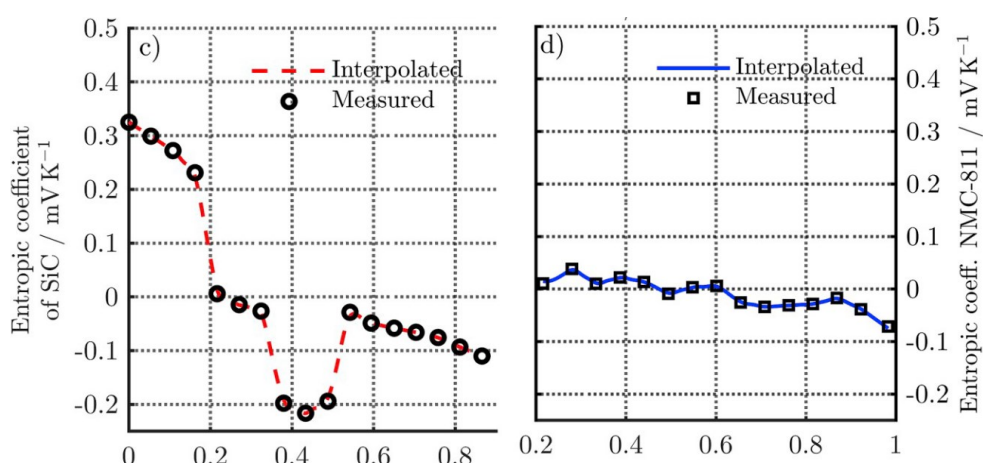


Figure 2-13 Entropic coefficient of (a) SiGr and (b) NMC-811 electrodes [72].

As Si and Gr have distinct reaction nature, they should have different effects on thermal behaviors of their composite electrodes. To clarify this point, the respective entropy profiling of Si and Gr are presented in Figure 2-14. It is evident to see that the entropy profiling of Gr [74] varies from stage (I) to stage (IV) with filling fraction of lithium, indicating the respective staging processes of Gr. Within each stage, the entropy curve exhibits a flat shape suggesting a coexistence of two Li-C phases. In contrast, silicon (without deep lithiation) [75] presents relatively flat reversible heat

flow (due to entropic variation) curves during the whole charge and discharge processes, implying no significant structural changes.

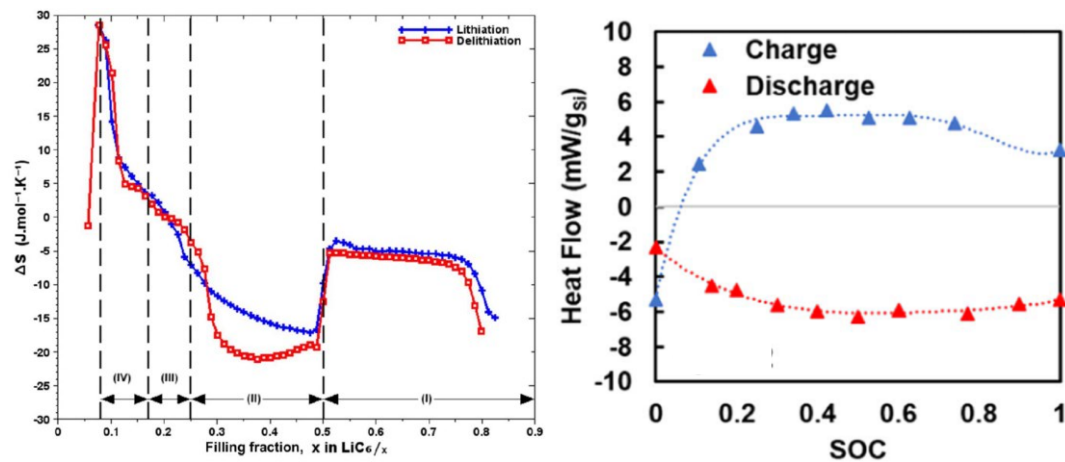


Figure 2-14 Entropy profiling of Gr [74] and reversible heat flow of Si [75].

Based on the experimental facts, the thermal behaviors of Si/Gr are a superposition of effects of both Si and Gr due to their different thermal characteristics.

2.3. Modelling of lithium-ion batteries

2.3.1. Overview of different modelling approaches

The existing LIB models can be classified into two categories, empirical models, and physics-based models [76].

The favorable empirical models of batteries are electrical equivalent circuit network (ECN) models and data-driven models which have been widely used in the battery management system (BMS) in vehicle industries due to their simple construction and high computational efficiency. An ECN model [77–79] uses a combination of resistors, capacitors and voltage sources in an electrical circuit to describe LIB dynamics, but they can only provide little insight into the battery internal states and cannot cope with the variation of battery designs. The shortcomings of empirical models are offset by physics-based models. Data-driven models are developed by different approaches such as machine learning methods, filtering techniques, stochastic methods, and time series methods [80,81], and the model can be

trained to represent the relationship between inputs and outputs even without prior knowledge of data nature and interactions. However, the reliability of such data-driven models strongly relies on the fidelity of the input data, and the models cannot reveal the internal relationship between each parameter and the output performance due to their “black-box” nature [82].

Physics-based electrochemical models [83,84] solve the fundamental principles of underlying battery physics, and the macroscopic model include single particle model (SPM) and Doyle-Fuller-Newman P2D model. When the simulation scale reduces to microscopic or atomic level, molecular dynamics (MD) and kinetic Monte Carlo (KMC) modelling offer another predictive tool which puts specific focus on simulations of material and interface properties such as transport properties of electrolyte [85] and the mixing mechanism of Li and electrode materials [86]. However, the geometry size is largely limited in a MD or KMC simulation because of the high computational cost, thus making this kind of model unfeasible for battery design and optimization.

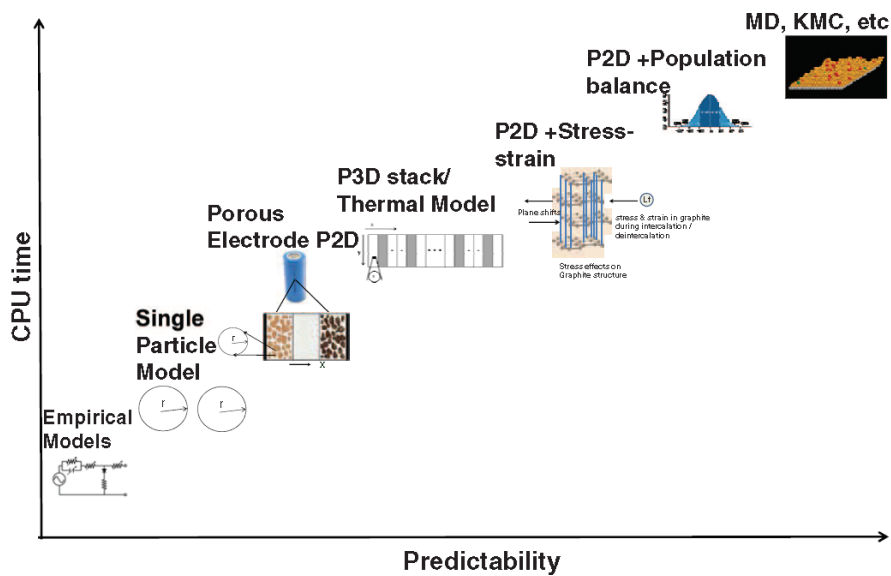


Figure 2-15 Comparison of different Li-ion battery models with respect to their computational complexity (CPU time) and predictability [76].

The comparison of different kinds of models in terms of their computational costs and predictability is shown in Figure 2-15 [76].

As the aim of this thesis is to develop models able to capture the unique physics and link the physics to the electrode and cell behaviors, macroscopic physics-based models are the ideal approach.[87]

2.3.2. *Physics-based models*

This section is based on “Yang Jiang=, Lingding Zhang=, Gregory Offer, Huizhi Wang*, A user-friendly lithium battery simulator based on open-source CFD, Digital Chemical Engineering, 2022, 5 / 100055” [87]. Yang Jiang: Methodology, Software, Validation, Formal analysis, Writing - original draft, Visualization, Project administration. Lingding Zhang: Methodology, Software, Writing – original draft, Visualization. Gregory Offer: Supervision, Writing –review & editing. Huizhi Wang: Conceptualization, Supervision, Writing –review & editing, Funding acquisition, Project administration.

It is worth gaining a complete understanding of the architecture and physio-chemical processes involved in a lithium-ion battery system before developing a model of it. The working performance of a lithium-ion battery strongly depends on the highly coupled charge/mass transport and electrochemical kinetics. The schematics of the basic SPM and P2D models in a single full cell and half-cell framework are illustrated in Figure 2-16. Note that the electrochemical behaviors of LIB materials are usually characterized in a half-cell setup (Figure 2-16 (b)), in which a working electrode (made of an electrode material of interest) is paired with lithium metal as both the reference and counter electrode [88].

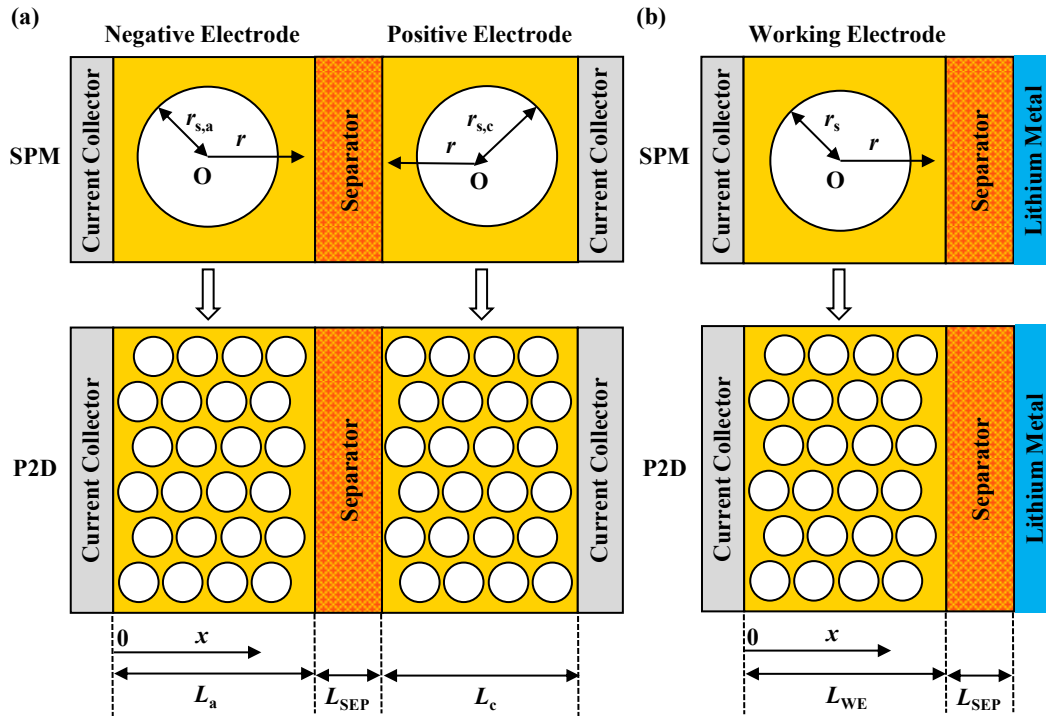


Figure 2-16 Schematics of the SPM and P2D model for (a) a full cell and (b) a half cell [87].

For modern lithium-ion batteries, typical negative electrode active materials include Gr, Li metal, $\text{Li}_4\text{Ti}_5\text{O}_{12}$ and Si [4], typical positive electrode active materials include transition metal oxides or phosphate active materials (LiCoO_2 , LiMn_2O_4 , $\text{LiCo}_{1/3}\text{Mn}_{1/3}\text{Ni}_{1/3}\text{O}_2$, LiFePO_4 , etc.) [5], and the electrolyte normally contains LiFP_6 salt mixed with organic carbonates such as propylene carbonate (PC), ethylene carbonate (EC), dimethyl carbonate (DMC) and ethyl methyl carbonate (EMC) [6]. During discharge, the negative electrode (or anode) is oxidized to release electrons to the external circuit, while the positive electrode (or cathode) is reduced by taking the electrons from the external circuit. Lithium-ions in the electrolyte moves from anode to cathode through migration and diffusion as a result of the presence of potential and concentration gradients. The process is reversed during charge. The detailed theories and equations of SPM and P2D models are introduced in the following sections.

Single particle model

The SPM considers each electrode in a LIB cell as a single particle as shown in the top panel of Figure 2-16 [87], and it solves the diffusion and electrochemical reactions within the single particles [89]. This type of electrochemical model is featured by simplicity and low computational costs, and thus commonly used for online estimation and lifetime simulation of LIBs [90,91]. However, the SPM exhibits poor accuracies at high current densities and thick electrodes because it normally ignores the concentration and potential variations in the electrolyte phase [92].

The lithium diffusion within a single electrode particle is solved by the following conservation equation

$$\frac{\partial C_s}{\partial t} = \nabla \cdot (D_s \nabla C_s) \quad (2-1)$$

where C_s is the lithium concentration in the solid phase (mol m^{-3}), and D_s is the lithium diffusivity in the solid phase ($\text{m}^2 \text{s}^{-1}$).

The lithium flux at the particle surface is driven by the electrochemical reaction, which is expressed as

$$\left. \frac{\partial C_s}{\partial r} \right|_{r=r_s} = -\frac{i_{Li}}{D_s F} \quad (2-2)$$

where r_s is the electrode particle radius (m), F is the Faraday constant ($F = 96485 \text{ C mol}^{-1}$), and i_{Li} is the reaction current density (A m^{-2}) determined by the Butler-Volmer equation [93]

$$i_{Li} = i_0 \left(e^{\alpha_a F \eta / RT} - e^{-\alpha_c F \eta / RT} \right) \quad (2-3)$$

where η is the overpotential (V) defined as the deviation between the electrode and the equilibrium potential, R is the universal gas constant ($R = 8.314 \text{ J mol}^{-1} \text{ K}^{-1}$), T is the

temperature (K), and α_a and α_c are charge transfer coefficients. i_0 is the exchange current density (A m^{-2}), given by

$$i_0 = k_{\text{react}} F \sqrt{C_e C_s^{\text{surf}} (C_s^{\text{max}} - C_s^{\text{surf}})} \quad (2-4)$$

where k_{react} is reaction rate constant ($\text{m}^{2.5} \text{mol}^{-0.5} \text{s}^{-1}$), C_e is electrolyte concentration (mol m^{-3}), C_s^{max} is the maximum lithium concentration (mol m^{-3}) in active materials, and C_s^{surf} is the interfacial lithium concentration (mol m^{-3}).

A symmetric boundary condition of lithium diffusion is applied at the center of the electrode particle, thus having

$$\left. \frac{\partial C_s}{\partial r} \right|_{r=0} = 0 \quad (2-5)$$

The total applied current density can be related to the reaction current per unit particle surface i_{Li} considering the geometry of the battery as

$$i_{\text{app}} = i_{\text{Li}} a_s \delta \quad (2-6)$$

which can be further written as a function of C-rate as

$$i_{\text{app}} = \frac{C_s^{\text{max}} F c_{\text{rate}} \delta \varepsilon_s}{3600} \quad (2-7)$$

where δ is the working electrode thickness (m), and a_s is the specific surface area of active particles (m^{-1}) given by

$$a_s = \frac{3\varepsilon_s}{r_s} \quad (2-8)$$

where ε_s is the solid phase fraction in the electrode, which adds up to 1 with porosity ε_e .

By assuming that α_a and α_c are both 0.5 [91] as most literatures did, rearranging Eq. (2-3) gives

$$\eta = \frac{2RT}{F} \sinh^{-1} \left(\frac{i_{\text{app}}}{2i_0 a_s \delta} \right) \quad (2-9)$$

For the full-cell configuration, the output voltage is defined as the potential difference between the positive electrode and the negative electrode considering their respective overpotentials [91]

$$E = (E_{\text{eq}}^{\text{PE}} + \eta^{\text{PE}}) - (E_{\text{eq}}^{\text{NE}} + \eta^{\text{NE}}) \quad (2-10)$$

where $E_{\text{eq}}^{\text{PE}}$ and $E_{\text{eq}}^{\text{NE}}$ are the equilibrium potentials (V) of the positive and negative electrodes respectively, which depend on the lithiation state and electrode materials used.

For the half-cell configuration, a zero potential is applied to the lithium metal which is used as the counter and reference electrode. Hence, the cell voltage E (V) is calculated as

$$E = E_{\text{eq}}^{\text{WE}} + \eta^{\text{WE}} \quad (2-11)$$

where $E_{\text{eq}}^{\text{WE}}$ and η^{WE} are respectively the equilibrium potential (V) and the overpotential (V) of the working electrode.

Doyle-Fuller-Newman P2D model

As the other important type of physics-based electrochemical models, the P2D model is more commonly used for analyzing LIB internal states and optimizing LIB design parameters. As shown in the bottom panel of Figure 2-16, this modelling approach considers two dimensions in space: one macroscopic x direction that measures

the distance across the cell, and the other microscopic radial direction of electrode particles as its pseudo-second dimension. Each electrode is treated as macro-homogeneous superimposed continua. The concentrated solution theory [84] is applied to model the transport in electrolyte, assuming a binary electrolyte and solvent. The solid phase in each electrode is assumed to be made up of uniformly distributed spherical particles of the same size.

Table 2-1. Governing equations of P2D model [87].

Domain	Description	ψ	Γ	ε	S
Electrolyte	Charge conservation	ϕ_e	κ^{eff}	0	$\nabla \cdot (\kappa_D^{\text{eff}} \nabla \ln C_e) + j^{\text{Li}}$
			$\kappa^{\text{eff}} = \kappa \times \varepsilon_e^{\text{brugg}}$ (2-12)		
			$\kappa = 10^{-4} \times C_e \left(\begin{array}{l} -10.5 + 0.668 \times 10^{-3} C_e + 0.494 \times 10^{-6} C_e^2 + \\ (0.074 - 1.78 \times 10^{-5} C_e - 8.86 \times 10^{-10} C_e^2) T + \\ (-6.96 \times 10^{-5} + 2.8 \times 10^{-8} C_e) T^2 \end{array} \right)$ [94] (2-13)		$\kappa_D^{\text{eff}} = \frac{2RT\kappa^{\text{eff}}}{F} (t_+^0 - 1)$ (2-14)
			where $C_e \in [0, 4500] \text{ mol m}^{-3}$		
	Conservation of Li^+	C_e	D_e^{eff}	ε_e	$\frac{1-t_+^0}{F} j^{\text{Li}}$
			$D_e^{\text{eff}} = D_e \varepsilon_e^{\text{brugg}}$ (2-15)		
Solid phase	Charge conservation	ϕ_s	σ_s^{eff}	0	j^{Li}
			$\sigma_s^{\text{eff}} = \sigma_s \varepsilon_s$ (2-16)		
	Conservation of lithium	C_s	0	ε_s	$\frac{-j^{\text{Li}}}{F}$

The equations of the classic Doyle Fuller Newman (DFN) P2D model [83,84,95] can be represented by a general Eq. (2-17) with the details summarized in Table 2-1.

$$\frac{\partial \psi}{\partial t} + \nabla \cdot (v\Psi) = \nabla \cdot (\Gamma \nabla \psi) + S \quad (2-17)$$

The transport coefficients in porous regions are corrected for their porosities using the Bruggeman's correlation. The volumetric current density j^{Li} (A m^{-3}) arising from electrochemical reactions in the source terms of different conservation equations is given by

$$j^{\text{Li}} = i^{\text{Li}} a_s \quad (2-18)$$

where i^{Li} (A m^{-2}) is obtained by the Butler-Volmer equation as shown in Eq. (2-3) with the overpotential determined by

$$\eta = \phi_s - \phi_e - E_{\text{eq}} \quad (2-19)$$

where ϕ_s and ϕ_e are the potentials (V) respectively in the solid and electrolyte phases.

The lithium distribution along the radial direction of each electrode particle is assumed here to follow the two-term polynomial approximation [94]

$$C_s^{\text{surf}} - C_s^{\text{avg}} = -\frac{r_s}{D_s} \frac{i^{\text{Li}}}{5F} \quad (2-20)$$

where C_s^{avg} means the averaged lithium concentration in the solid particles (mol m^{-3}) and C_s^{surf} is the surface lithium concentration (mol m^{-3}).

For full-cell modeling, at the interface between anode and current collector ($x = 0$) where no electrolyte and ions can pass through, the boundary conditions are shown as follows

$$\left. \frac{\partial \phi_e}{\partial x} \right|_{x=0} = 0 \quad (2-21)$$

$$\left. \frac{\partial C_e}{\partial x} \right|_{x=0} = 0 \quad (2-22)$$

where σ_s^{eff} refers to the effective electronic conductivity in the electrode (S m^{-1}).

The electrode potential ϕ_s at $x = 0$ is set to be the reference potential, thus having

$$\phi_s = 0 \quad (2-23)$$

At the interface between cathode and current collector ($x = L_a + L_{SEP} + L_c$), where only electrons can pass through to the exterior circuit, the boundary conditions are listed as follows

$$\left. \frac{\partial C_e}{\partial x} \right|_{x=L_a+L_{SEP}+L_c} = 0 \quad (2-24)$$

$$\left. \frac{\partial \phi_e}{\partial x} \right|_{x=L_a+L_{SEP}+L_c} = 0 \quad (2-25)$$

$$\left. \frac{\partial \phi_s}{\partial x} \right|_{x=L_a+L_{SEP}+L_c} = -\frac{i_{app}}{\sigma_s^{eff}} \quad (2-26)$$

The output voltage is defined as the difference between the two terminal electrode potentials

$$E = \phi_s \Big|_{x=L_a+L_{SEP}+L_c} - \phi_s \Big|_{x=0} \quad (2-27)$$

For half cells, Eqs. (2-21) and (2-22) can still apply, but the electrode potential gradient is dependent on the external applied current density

$$\left. \frac{\partial \phi_s}{\partial x} \right|_{x=0} = -\frac{i_{app}}{\sigma_s^{eff}} \quad (2-28)$$

At the interface between the separator and lithium metal ($x = L_{WE} + L_{SEP}$), the solid-phase potential is set to be zero, and the gradients of electrolyte potential and electrolyte concentration depend on the Faradaic current that is generated by the electrochemical reaction occurring at the surface of lithium metal, thus yielding [96,97]

$$\phi_s \Big|_{x=L_{WE}+L_{SEP}} = 0 \quad (2-29)$$

$$\frac{\partial C_e}{\partial x} \Big|_{x=L_{WE}+L_{SEP}} = -\frac{(1-t_+^0)i_{CE}}{D_e^{\text{eff}} F} \quad (2-30)$$

$$\frac{\partial \phi_e}{\partial x} \Big|_{x=L_{WE}+L_{SEP}} = -\frac{i_{CE}}{\kappa^{\text{eff}}} - \frac{\kappa_D^{\text{eff}}}{\kappa^{\text{eff}}} \frac{\partial \ln C_e}{\partial x} \quad (2-31)$$

where i_{CE} is the current density caused by lithium plating/stripping at the lithium metal (A m^{-2}).

The output voltage for a half-cell is calculated by

$$E = \phi_s \Big|_{x=0} - \phi_s \Big|_{x=L_{WE}+L_{SEP}} = \phi_s \Big|_{x=0} \quad (2-32)$$

2.3.3. Physics-based modelling of lithium-ion batteries with Si-based electrodes

Despite many experimental understanding of the electrochemical performance and lithiation/delithiation mechanisms of silicon electrodes, no comprehensive modelling tool has yet been developed to quantify the phase transformations during cycling and link them to the cycling behaviors of these electrodes. Macroscopic models have been developed for simulating the charge/discharge curves of silicon-based LIBs [98–101], however, none of them have considered the multi-step phase transformations and crystallization/amorphization involved in the silicon electrodes. A few studies [49,102] described the lithiation-induced amorphization of crystalline Si based on first-principles and molecular dynamics simulations, but they can hardly be used for battery cell design and optimization due to their small computational domains. Zhang [42] reviewed the lithiation/delithiation mechanisms of alloy electrode materials for LIBs and suggested that the surface (or interface) energy could play a crucial role in determining the unique behaviors of alloy materials like Si, but they provided no quantitative evidence.

Several models have been reported so far regarding the modelling of Si/Gr composite electrodes. Sturm et al. [103] modeled a commercial 18650 cell with a Si/Gr electrode, and they studied the non-uniformity in temperature and potential distributions by comparing a pseudo-two-dimensional (P2D) model and a multi-dimensional model. However, the Si/Gr electrode in their model was simplified as a single material with a fixed Si/Gr ratio, so their model was not able to reflect the effects of Si/Gr ratios on the internal state distributions and electrode/cell performance. Dhillon et al. [104] developed a model to describe the capacity fade of a Si/Gr electrode considering its porosity change and SEI growth, and the relationship between porosity changes and capacity fading was established with the consideration of the impact of micro cracks. Again, the model relied on the lumped properties of the Si/Gr electrode and thus can lead to observable discrepancies between the simulated voltage curves and the measured ones because of the ignorance of the difference between Gr and Si in cycling behaviors and degradation rates. Recently, Lory et al. [105] made an attempt to simulate the lithiation competition between different active components in a Si/Gr electrode with nano flakes of Si embedded in a carbon matrix. In their model, they equated the Si reaction rate to the lithium flux from the carbon matrix nearby without a detailed description of the electrochemical kinetics of the Si phase. Hence, key phase transition features and the corresponding sloping voltage behaviors of Si cannot be captured by their model. Many electrochemical-mechanical coupled models were developed, which highlighted the contributions of the individual materials to the overall mechanical behaviors of Si/Gr electrodes [106–108]. However, the same set of thermodynamic and kinetic properties were applied to Si and Gr in these mechanically coupled models. Since the mechanical and electrochemical behaviors are tightly coupled, the guidance capability of these models is therefore largely limited.

Consequently, there is a need for a Si/Gr electrode model capable of deconvoluting the electrochemical processes of the individual active materials from the overall electrode behaviors.

2.4. Summary

This chapter provides a focused literature review on the unique electrochemical and thermal properties exhibited by Si and Si/Gr composite electrodes. Additionally, different modelling approaches for lithium-ion batteries are outlined and their respective pros and cons are compared. Previous experimental observations have shown that silicon has clearly different electrochemical characteristics from graphite, the existing physics-based models towards traditional graphite materials become incompatible with silicon-based batteries. Despite many experimental advances in understanding the electrochemical performance and lithiation/delithiation mechanisms of silicon electrodes, there has been no mathematical description for the physics of phase transformations during cycling and correlating them with the cycling behaviors of silicon electrodes.

Due to the substantial volume change and concomitant cracking with pure silicon, composite electrodes with a mixture of silicon and graphite have been more common, which takes advantage of the high capacity of silicon and the good structural stability of graphite. In experiments, the Si/Gr composite electrodes behave differently from the Si electrodes and Gr electrodes. There is a need for understanding the behaviors of composite electrodes and how each active material contributes to the overall performance of composite electrodes. To address this issue, a multi-material model is required to establish mechanistic insights into how material properties and structures affect overall battery performance, guiding the design of such composite electrodes.

There are various approaches available for battery modeling, including empirical ECN and data-based models, as well as macroscopic physics-based SPM and P2D models, and microscopic MD and KMC models. Among these modeling approaches, macroscopic physics-based modeling is the most appropriate for designing and optimizing silicon-based electrodes while preserving physical accuracy. These models can provide valuable insights into the internal status of batteries while maintaining a relatively low computational cost.

Chapter 3. Modelling voltage hysteresis of silicon electrodes

3.1. Introduction

The literature review identified that a new model is required to capture the voltage hysteresis phenomenon in Si and link the hysteresis with the underlying physics. In this chapter, I therefore develop a mechanistic model of silicon anodes to describe their unique voltage hysteresis, considering the multi-step phase transformations, crystallization and amorphization of different lithium-silicon phases during cycling. Using the hysteresis model, the following research questions are answered:

(1) Why do Si anodes exhibit a broad single voltage plateau when lithium-ions insert/extract into/from the crystalline phase?

(2) Why does the crystalline $\text{Li}_{15}\text{Si}_4$ appear abruptly at the end of alloying (near 0 V), while disappears gradually through nearly the whole dealloying process?

(3) How will the particle size affect the electrochemical performance of Si?

This chapter is based on “Yang Jiang, Gregory Offer, Jun Jiang, Monica Marinescu, Huizhi Wang*, Voltage hysteresis model for silicon electrodes for lithium ion batteries, including multi-step phase transformations, crystallization and amorphization, Journal of The Electrochemical Society, 2020, 167(13) / 130533” [109]. Yang Jiang: Methodology, Software, Validation, Formal analysis, Investigation, Writing - original draft, Visualization, Data curation. Gregory Offer: Conceptualization, Supervision, Writing –review & editing, Resources, Funding acquisition, Project administration. Jun Jiang: Conceptualization, Writing –review & editing, Resources. Monica Marinescu: Conceptualization, Writing – review & editing, Software. Huizhi Wang: Conceptualization, Supervision, Writing –review & editing, Software, Resources, Funding acquisition, Project administration, Data curation.

3.2. Reaction pathways and physical mechanisms

3.2.1. Reaction pathways when the lower cut-off voltage is above 0.05 V

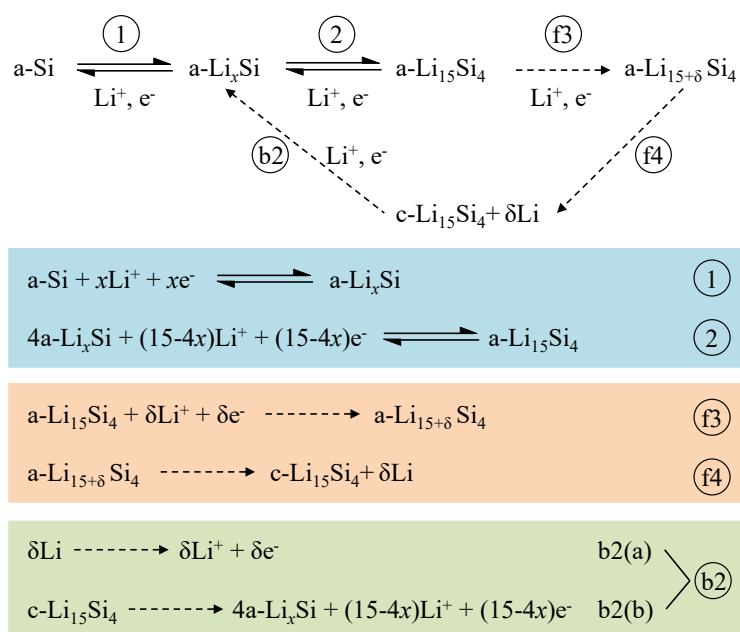


Figure 3-1 Reaction pathways for electrochemical lithiation and delithiation of Si at room temperatures.

When silicon is lithiated to above 0.05 V vs. Li/Li⁺, two distinguishable characteristic voltage peaks occur in incremental capacity analyses [40,110,111], indicating that there exist two major structure transformations during the cycling within this voltage range. The details of the two structure transformations have been confirmed in the in-situ TEM experiment by Wang et al. [43]. The first step is a heterogeneous two-phase transformation from amorphous Si (a-Si) to amorphous Li_xSi (a-Li_xSi), through which a distinct phase boundary was observed in the study of Wang et al. [40]. So far, no agreement has been reached on the exact value of *x*, and *x* is generally considered less than 2 [29,45]. The second step of lithiation was found to proceed without a visible interface, forming the final amorphous product a-Li₁₅Si₄. Based on the above evidence from the literatures, as shown in Figure 3-1, a two-step reaction mechanism consisting

of two reversible electrochemical steps 1 and 2 is proposed for cycling of Si in a voltage range above 0.05 V.

3.2.2. Reaction pathways when the lower cut-off voltage is below 0.05 V

When the voltage of Si falls below 0.05 V vs. Li/Li⁺, another voltage plateau which is visibly short appears at the end of charge [36], accompanied by an abrupt formation of crystalline c-Li₁₅Si₄ [29]. The rapid appearance of a crystalline phase suggests a homogeneous crystallization from the amorphous composition of Li₁₅Si₄. This homogeneous crystallization process is analogous to the freezing of super-cooled water where liquid water can stay completely free of ice for a long period before being instantaneously crystallized to ice. However, the process is too fast to have been captured in any in-situ studies. A homogeneous crystallization typically involves a preceding nucleation from bulk composition and a subsequent grain growth based on the existing nuclei sites [112]. Hence, it is reasonable to describe the process using a two-step mechanism, i.e., an electrochemical step f3 that forms critical nuclei of Li_{15+δ}Si₄ (δ represents a very small increment of lithium) from bulk solid solution followed by a chemical step f4 that grows the nuclei to the metastable crystalline phase c-Li₁₅Si₄. Using the super-cooled water analogy, a “super-alloyed” phase a-Li_{15+δ}Si₄ is assumed as the product of the reaction step f3 [113], which is assumed to have the local highest energy and an unstable structure. The electrochemical step f3 is driven by overpotentials which push a-Li₁₅Si₄ phase to overcome the surface energy barrier of forming a nucleus[114]. During the process, the original bulk phase of Li₁₅Si₄ is expected to grow to its critical size by accommodating more lithium-ions, which explains the slight capacity increase during crystallization of Li₁₅Si₄ [36]. The extra lithium atoms (represented by δ) are believed to act as a “catalyst” which enables the crystallization process by activating the amorphous Li₁₅Si₄, despite the small amount.

In contrast to the sloping voltage curve in the charge process, the discharge process exhibits a single distinct voltage plateau at ~0.4 V [29,41]. It was found by Li et al. [29] using in situ XRD that the crystalline $\text{Li}_{15}\text{Si}_4$ disappeared linearly with time under a galvanostatic condition. These experimental findings indicate a two-phase heterogeneous amorphization process of c- $\text{Li}_{15}\text{Si}_4$. The linear decrease of crystalline phase under constant current conditions implies that this amorphization process is rate determining. Previous studies [29] suggested that the product of the amorphization process could be a- Li_xSi . Ignoring the reaction of the extra lithium atoms b2(a) ($\delta \ll 15$), here it is assumed that the amorphization of c- $\text{Li}_{15}\text{Si}_4$ follows the reaction step b2(b) to end up with the same product of the reaction step 1, in view of the metastable structure of the intermediate product.

3.2.3. Pathway diagram

The proposed pathways of electrochemical lithiation/delithiation of Si at room temperatures are summarised in Figure 3-1. The lithiation/delithiation process follows a two-step mechanism consisting of two reversible electrochemical steps 1 and 2 when the electrode potential is maintained above 0.05 V, and will undergo homogeneous crystallization steps f3 and f4 for lithiation and heterogeneous amorphization b2 for delithiation when the electrode potential goes below 0.05 V.

3.3. Development of voltage hysteresis model

3.3.1. Thermodynamics

The equilibrium potentials of electrochemical reactions 1, 2, f3 and b2 are calculated as [115,116]:

$$E_{(j)} = E_{(j),0} + \frac{w_{(j)}}{f} \ln \left(\frac{\Delta x_{(j)} - x_{(j)}}{x_{(j)}} \right) \quad (3-1)$$

$$(3-2)$$

$$f = F/RT$$

where $E_{(j)}$ and $E_{(j),0}$ are respectively the equilibrium potential (V) and standard equilibrium potential (V) of reaction j ($j = 1, 2, f3, b2$), F is the Faraday constant ($F = 96485 \text{ s A mol}^{-1}$), R is the universal gas constant ($R = 8.314 \text{ J mol}^{-1} \text{ K}^{-1}$), T is temperature (K) and $w_{(j)}$ is an adjustable parameter describing the interactions between transferred electric charge and its surrounding in reaction j . It is noted that Eq. (1) is a general description of equilibrium potential, which accounts for the short-range interactions between neighboring ions (via $w_{(j)}$) and has been widely used in the literatures. An detailed interpretation of the parameter $w_{(j)}$ can be found in the literatures [115,116]. The term $(\Delta x_{(j)} - x_{(j)})$ represents the remaining vacant sites for lithium through reaction j , where $\Delta x_{(j)}$ is the fraction of total host sites for lithium-ions through reaction j and $x_{(j)}$ is the fraction of the already occupied sites in that reaction. For each electrochemical reaction, the fraction of total host sites for lithium-ions, $\Delta x_{(j)}$, is calculated as the ratio of the maximum capacity through that reaction ($Q_{(j)}$) to the total capacity when silicon is fully lithiated (Q_{tot}) and can be further expressed in terms of the compositions of reactants and products

$$\Delta x_{(1)} = \frac{Q_{(1)}}{Q_{\text{tot}}} = \frac{x}{3.75 + \delta/4} \quad (3-3)$$

$$\Delta x_{(2)} = \Delta x_{(b2)} = \frac{Q_{(2)}}{Q_{\text{tot}}} = \frac{3.75 - x}{3.75 + \delta/4} \quad (3-4)$$

$$\Delta x_{(f3)} = \frac{Q_{(f3)}}{Q_{\text{tot}}} = \frac{\delta/4}{3.75 + \delta/4} \quad (3-5)$$

The values x , 3.75 and $(3.75 + \delta/4)$ on the right hand side of the above equations are the average lithium/silicon ratios of host structures $[\text{a-Li}_x\text{Si}]$, $[\text{a-Li}_{15}\text{Si}_4]$ and $[\text{a-Li}_{15+\delta}\text{Si}_4]$.

The total capacity, Q_{tot} , is related to the specific mass of Si, $m_{\text{t,Si}}$, by

$$Q_{\text{tot}} = (3.75 + \delta / 4) \frac{m_{\text{t,Si}} F}{M_{\text{Si}}} \quad (3-6)$$

where M_{Si} is the molar mass of Si ($M_{\text{Si}} = 28 \text{ g mol}^{-1}$). It is noted that the sum of $\Delta x_{(j)}$ ($j = 1, 2, \text{f}3$) should be equal to 1.

3.3.2. Electrochemical amorphization

Reaction b2, the heterogeneous amorphization of c-Li₁₅Si₄, occurs only on the crystalline surface where the atoms have higher free energy than the interior ones, thereby following a “peeling off” pattern. Compared to the conversion of a-Li₁₅Si₄ to a-Li_xSi in reaction 2, the amorphization of c-Li₁₅Si₄ to a-Li_xSi needs to overcome an extra energy barrier ΔG^* (eV)

$$\Delta G_{(\text{b}2),0} = \Delta G_{(2),0} + \Delta G^* \quad (3-7)$$

where $\Delta G_{(\text{b}2),0}$ and $\Delta G_{(2),0}$ respectively denote the standard Gibbs energy changes of reactions b2 and 2. The change in the Gibbs free energy leads to a higher equilibrium potential of reaction b2 than that of reaction 2

$$E_{(\text{b}2),0} = \frac{\Delta G_{(\text{b}2),0}}{(3.75 - x)e} = \frac{\Delta G_{(2),0} + \Delta G^*}{(3.75 - x)e} = E_{(2),0} + E^* \quad (3-8)$$

where e is the elementary charge ($e = 1.6 \times 10^{-19} \text{ A s}$), and E^* is an extra voltage increase induced by the surface energy barrier (V). In Eq. (3-8), the Gibbs free energy changes are all positive since the delithiation process is nonspontaneous.

3.3.3. Charge transfer kinetics

The reaction rate for each electrochemical steps 1, 2, f3 and b2 is assumed to follow a simplified Butler-Volmer equation,

$$i_{(j)} = -2i_{(j),0} \sinh\left(\frac{f\eta_{(j)}}{2}\right) \quad (3-9)$$

where $i_{(j)}$ is the current density (A m^{-2}) for reaction j and $i_{(j),0}$ is the reference current density (A m^{-2}) of reaction j . $i_{(j)}$ is defined to be positive for charge and negative for discharge. $\eta_{(j)}$ is the overpotential (V) of reaction j , and expressed as

$$\eta_{(j)} = V - E_{(j)} \quad (3-10)$$

where V is the electrode potential (V).

The total current density of the silicon electrode, I , is the sum of the partial current densities

$$I = \sum_j i_{(j)} \quad (3-11)$$

3.3.4. Crystallization kinetics

As discussed in section 3.2, the crystallization of a- $\text{Li}_{15}\text{Si}_4$ involves an electrochemical nucleation step (f3) followed by a crystal growth step (f4). The kinetics of the reaction f4 can be described using the classical nucleation theory [112]

$$J = W^* n_s^* \quad (3-12)$$

where J is nucleation rate (mol s^{-1}) and n_s^* is the near equilibrium concentration of critical nuclei (mol m^{-3}). W^* is the rate of the condensable species upon these nuclei through impingement ($\text{m}^3 \text{s}^{-1}$), which is proportional to the surface area of the nuclei S [112]

$$W^* = k_0 S \quad (3-13)$$

where k_0 is the rate constant of crystallization (m s^{-1}).

Based on the classical nucleation theory, here a heuristic kinetic expression for reaction step f4 is developed

$$\frac{dx_{\text{cryst}}}{dt} = k_{\text{cryst}} x_{\text{cryst}} \left(\frac{x_{(\text{f3})}}{\Delta x_{(\text{f3})}} - x_{\text{cryst}} \right) \quad (3-14)$$

where $\left(\frac{x_{(\text{f3})}}{\Delta x_{(\text{f3})}} - x_{\text{cryst}} \right)$, analogous to n^* , represents the remaining fraction of critical

nuclei which should minus the already crystallized portion x_{cryst} ; x_{cryst} , analogous to S , represents the surface for crystal growth. The crystallization growth rate can also be

lumped to $k_{\text{cryst}}^* = k_{\text{cryst}} \left(\frac{x_{(\text{f3})}}{\Delta x_{(\text{f3})}} - x_{\text{cryst}} \right)$, which implies that the real growth rate is restricted

by the depletion of the parent nuclei [a-Li_{15+δ}Si₄].

3.3.5. Time evolution of species

By ignoring spatial heterogeneity within silicon electrode, the rate of change in the molar fraction of the inserted lithium for each electrochemical reaction is given by

$$\frac{dx_{(j)}}{dt} = \frac{i_{(j)}}{Q_{\text{tot}}} \quad (3-15)$$

In the absence of crystallization, the normalized concentrations of a-Si, a-Li_xSi and a-Li₁₅Si₄ are expressed in the fraction of occupied sites

$$C_0 = 1 - \frac{x_{(1)}}{\Delta x_{(1)}} \quad \text{for a-Si} \quad (3-16)$$

$$C_1 = \frac{x_{(1)}}{\Delta x_{(1)}} - \frac{x_{(2)}}{\Delta x_{(2)}} \quad \text{for a-Li}_x\text{Si} \quad (3-17)$$

$$C_2 = \frac{x_{(2)}}{\Delta x_{(2)}} \quad \text{for a-Li}_{15}\text{Si}_4 \quad (3-18)$$

In the presence of crystallization, the normalized concentration of a-Li₁₅Si₄ becomes

$$C_2 = \frac{x_{(2)}}{\Delta x_{(2)}} - \frac{x_{(f3)}}{\Delta x_{(f3)}} \quad (3-19)$$

and the normalized concentrations of the critical nuclei and crystalline phase are calculated by

$$C_3 = \frac{x_{(f3)}}{\Delta x_{(f3)}} - x_{\text{cryst}} \text{ for critical nuclei} \quad (3-20)$$

$$C_{\text{cryst}} = x_{\text{cryst}} \quad (3-21)$$

3.3.6. Computational implementation and initial conditions

The model consists of differential equations Eqs. (3-1), (3-9), (3-10), (3-11), (3-14) and (3-15) for $(4j + 2)$ unknowns: $x_{(j)}$, x_{cryst} , $i_{(j)}$, V , $\eta_{(j)}$ and $E_{(j)}$. The fractions C_z and C_{cryst} are further determined using Eqs. (3-16) - (3-21) with the values of $x_{(j)}$ and x_{cryst} solved from the differential equation system. Due to the apparent stiffness of the problem, as evidenced by Eqs (3-1), (3-9), and (3-14), which display exponential relationships, several techniques have been implemented to ensure numerical stability during the calculation of this stiff problem:

1. Nondimensional concentration of different phases was employed to avoid occurrence of ill-conditioned coefficient matrices.
2. The initial conditions for all variables were calculated self consistently from chosen values of V and x_{cryst} for charge and V for discharge. The partial current densities were initialized as $i_{(1)} = I$, $i_{(j)} = 0$ ($j = 2, f3$) for charge and $i_{(2)}/i_{(b2)} = I$, $i_{(1)} = 0$ for discharge.
3. The equation system was solved by the Runge-Kutta method using MATLAB ode23t. The trapezoidal rule and backward differentiation formula (BDF) implicit numerical method were also employed.

4. The relative tolerance was reduced to around 1×10^{-8} to achieve high calculation accuracy during numerical iteration within each time step.

The values of model parameters used for base case simulations are summarized in Table 3-1. The lithium/silicon ratio in a-Li_xSi is fitted to be 1.6 from the experimental data [45] used in this study. The potential increase in amorphization E^* is set to be 0.15 V, corresponding a surface energy gap of 0.3225 eV/atom. This has the same order of magnitude as the energy gap between amorphous and crystalline bulk Si [117,118]. The values of reference current densities vary dramatically in the literatures [119–122], ranging from 1 to 10^9 A m⁻². Here the values of reference current density are estimated to be 0.002, 0.008, 0.008 and 0.004 A m⁻² respectively for reactions 1, 2, f3 and b2 due to the lack of precise experimental data. Although internal stress can also be attributed to the voltage gap between lithiation and de-lithiation curves of silicon electrodes [120,123], we only consider the kinetic contribution to the hysteresis in this study. The adjustable parameter $w_{(j)}$ were reported in a range of 0.7-6.0 [110], and we take the values of 1.5 and 1.0 for different reaction steps. All simulations are performed at 298 K.

Table 3-1 Parameter values used in base case simulations.

Parameter	Unit	Value	Comment/reference
δ		0.01	Assumed
$E_{(1),0}/E_{(2),0}$	V	0.375/0.18	Ref. [42]
$E_{(f3),0}$	V	0.053	Ref. [36]
E^*	V	0.15	Estimated based on the surface energy gap between amorphous and crystalline Si reported in references [117] and [118]
$i_{(1),0}/i_{(2),0}$	A m ⁻²	0.002/0.008	Assumed
$i_{(f3),0}/i_{(b2),0}$	A m ⁻²	0.008/0.004	Assumed
k_{cryst}	s ⁻¹	0.00036	Assumed
$w_{(1)}/w_{(2)}$		1.5/1.0	Ref. [110]
$w_{(f3)}/w_{(b2)}$		1.0/1.0	Ref. [110]
x		1.6	Fitted for reference [45]

3.4. Results and discussion

3.4.1. Model-experiment comparisons

Figure 3-2 compares the model results with the experimental data reported in the literature [40]. The simulated charge-discharge curves agree well with the measured ones. As can be seen in the figure, the model successfully reproduces the sloping voltage curves of both charge and discharge processes when the amorphous silicon electrode is cycled above 0.05 V (vs. Li/Li⁺). The voltage curves of discharge and charge processes appear to be approximately parallel to each other with a huge voltage hysteresis in between which is caused by sluggish kinetics (small i_0). The model is further validated against the experimental data for deep lithiation of Si [45]. It can be seen in Figure 3-3(a) that the model results are consistent with experimental results by showing the same asymmetric feature, where the charge curve exhibits a sloping shape and the discharge curve has a single voltage plateau. For both scenarios of >0.05 V and <0.05 V, it is noted that the biggest difference between our model and experimental results occurs at the end of discharge (EOD) and the end of charge (EOC). This can be caused by asymmetric internal stress, which makes a larger voltage hysteresis at the EOD than that at the EOC [123]. Hence, the neglect of stress effect in this study may lead to an underestimation of voltage hysteresis at the EOD and an overestimation of voltage hysteresis at the EOC.

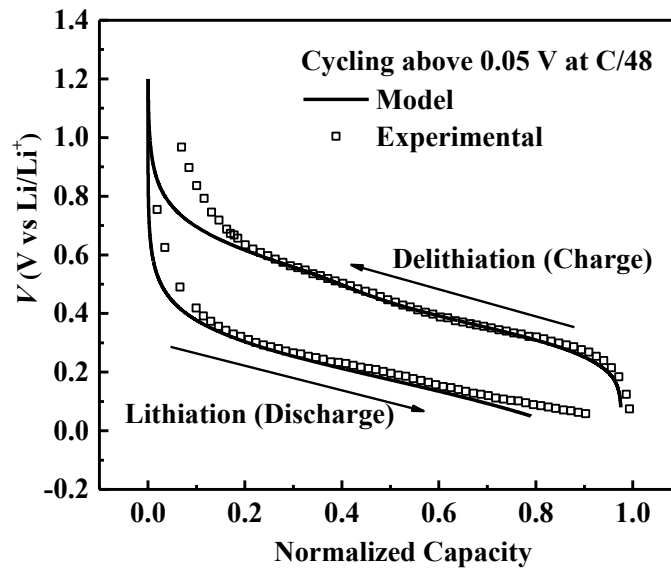


Figure 3-2 Comparison of model predictions with the experimental data [40] for an amorphous silicon electrode operating at voltages above 0.05 V.

The predicted composition change during deep cycling is compared with the XRD results in Figure 3-3(b) and (c). As shown in Figure 3-3(b), a sudden formation of $c\text{-Li}_{15}\text{Si}_4$ at a charge voltage of 0.05 V is shown in both the model predictions and experimental measurements. Figure 3-3(c) shows that the linear decrease of $c\text{-Li}_{15}\text{Si}_4$ observed by in situ XRD is also well captured by our model.

It is worth mentioning that the asymmetric voltage hysteresis as well as phase changes of silicon electrodes have never been well described by previous models which have taken into account various types of overpotential (i.e., charge-transfer, diffusion and ohmic overpotentials) and internal mechanical stresses [123,124].

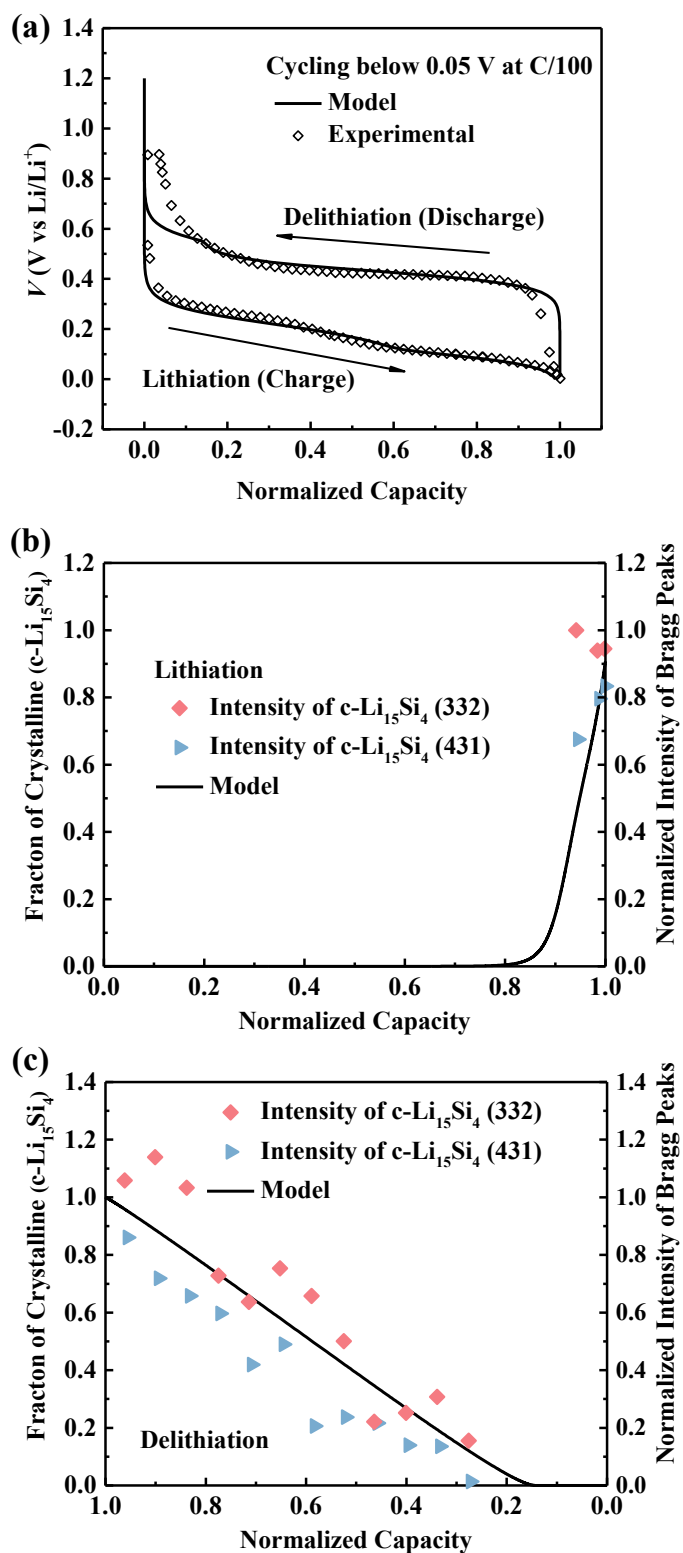


Figure 3-3 Comparison of model predictions with the experimental data [45] below 0.05 V: (a) charge/discharge curves and concentration variation of $c\text{-Li}_{15}\text{Si}_4$ during (b) charge and (c) discharge.

3.4.2. Charge/discharge behavior

The model is used to study the charge/discharge behaviors of Si in details. Figure 3-4(a) and (b) respectively show the charge/discharge curves and the corresponding differential voltage spectroscopy when silicon is lithiated above 0.05 V. The sigmoidal shaped voltage curve with two sloping plateaus in Figure 3-4(a) as well as its associated characteristic peaks in Figure 3-4(b) have been widely reported in experimental studies on silicon electrodes [47,125]. This sigmoidal shape is a typical feature of electrochemical phase changes, and the voltage tends to hold during each phase transformation process, thus exhibiting a voltage plateau during charge/discharge. In Figure 3-4(a), both the charge and discharge curves have two voltage plateaus which imply two transformation reactions, i.e., reactions 1 and 2. The voltage characteristic peaks in Figure 3-4(b) suggest that the two discharge reactions respectively happen at 0.25 and 0.52 V vs Li/Li^+ , while the two charge reactions occur at 0.11 and 0.22 V vs. Li/Li^+ . The variations of different silicon phases during cycling are further examined in Figure 3-4(c) and (d). When silicon is charged from D_1 to D_2 (Figure 3-4(a)), it is seen in Figure 3-4(c) that a-Si declines almost linearly and a- Li_xSi increases at the same time, and reaction 1 dominates over reaction 2. It is also found that a- $\text{Li}_{15}\text{Si}_4$ grows slower than a- Li_xSi in the D_1 - D_2 regime, confirming that reaction 2 is a slower step in this regime. When silicon is further charged from D_2 to D_3 , a- Li_xSi stops growing and transforms to a- $\text{Li}_{15}\text{Si}_4$ via reaction 2. These two electrochemical reactions proceed in the reverse direction during discharge. It is shown in Figure 3-4(d) that a- $\text{Li}_{15}\text{Si}_4$ will firstly transform to a- Li_xSi , followed by the phase transformation from a- Li_xSi to a-Si.

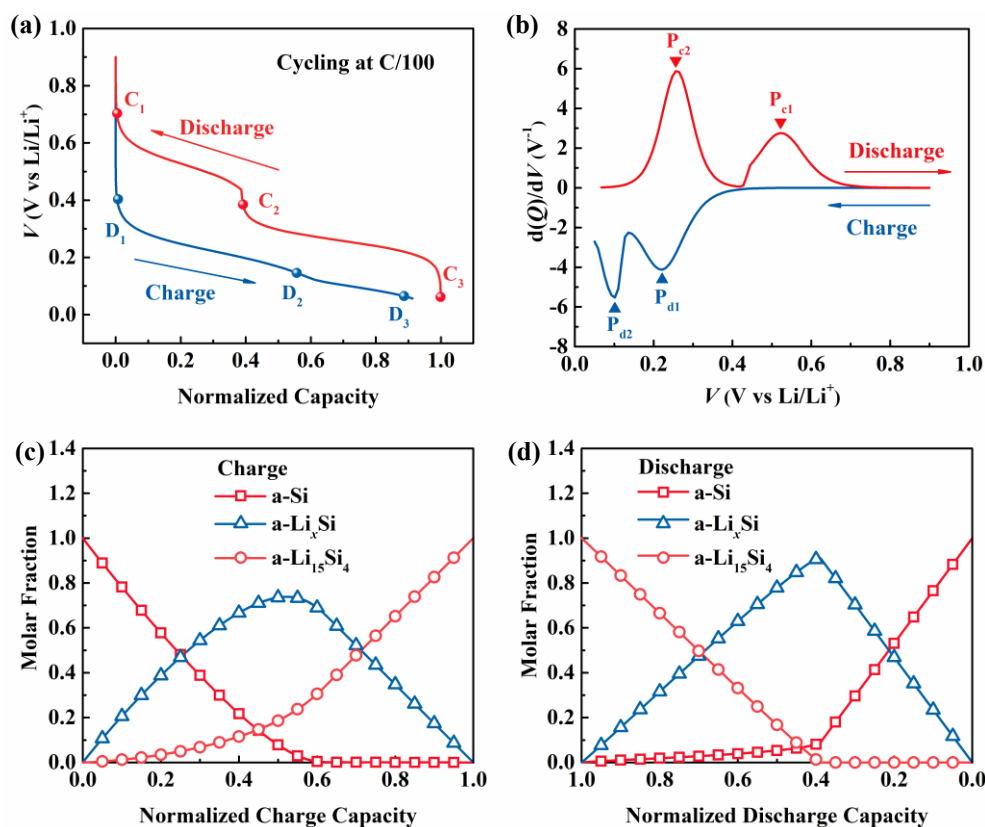


Figure 3-4 Electrochemical behaviors and phase transformations of Si in the absence of crystallization during discharge and charge: (a) voltage curves; (b) differential voltage curves; and composition variations during (c) charge and (d) discharge.

The charge/discharge behaviors and the corresponding phase transformations for cycling Si below 0.05 V are studied in Figure 3-5. In contrast to Figure 3-4(a), the lower voltage plateau is elevated and even merges with the higher plateau during the discharge process in Figure 3-5(a), which displays a wide voltage plateau at ~ 0.4 V. This phenomenon is confirmed in Figure 3-5(b), where P_{c2} moves to a higher voltage level and P_{c1} becomes unnoticeable. Figure 3-5(a) and (b) confirm that the electrochemical behaviors of silicon electrodes are path-dependent: (a) When the voltage remains higher than 0.05 V, silicon only follows the lithiation steps 1 and 2, leading to two sloping plateaus during both charge and discharge; (b) When the voltage falls below 0.05 V, silicon will undergo an additional crystallization process, thereby showing a distinct flat voltage plateau during de-lithiation. Figure 3-5(c) shows variation of different

silicon phases during charge. It is found that the initial two electrochemical steps are similar to those in Figure 3-4(c), where a-Si is firstly lithiated to form a-Li_xSi before transforming to a-Li₁₅Si₄. The nucleation step f3 starts at a normalized capacity of ~0.5, slowing down the formation of a-Li₁₅Si₄ in the second half of the capacity range. At the same time, the critical nuclei a-Li_{15+δ}Si₄ starts to grow until it reaches to a fraction of 0.3, and then the fraction of c-Li₁₅Si₄ starts to increase exponentially. For the reverse process, Figure 3-5(d) shows that c-Li₁₅Si₄ is firstly amorphized to a-Li_xSi which is further delithiated to form a-Si. Compared to the case in Figure 3-4(d), the fraction of a-Si in the reverse process grows at the beginning, indicating that the reaction rate of step 1 is comparable to that of step b2 through the discharge process. In addition, the maximum fraction of a-Li_xSi is found to be less than 0.4, which is less than half of that in Figure 3-4(d). Surprisingly, the depletion of Li₁₅Si₄ delays from the normalized capacity of 0.4 to 0.15. During the whole discharge process, the silicon electrode is composed of a mixture of a-Li_xSi and a-Si during amorphization, which implies that there may be no pure intermediate component.

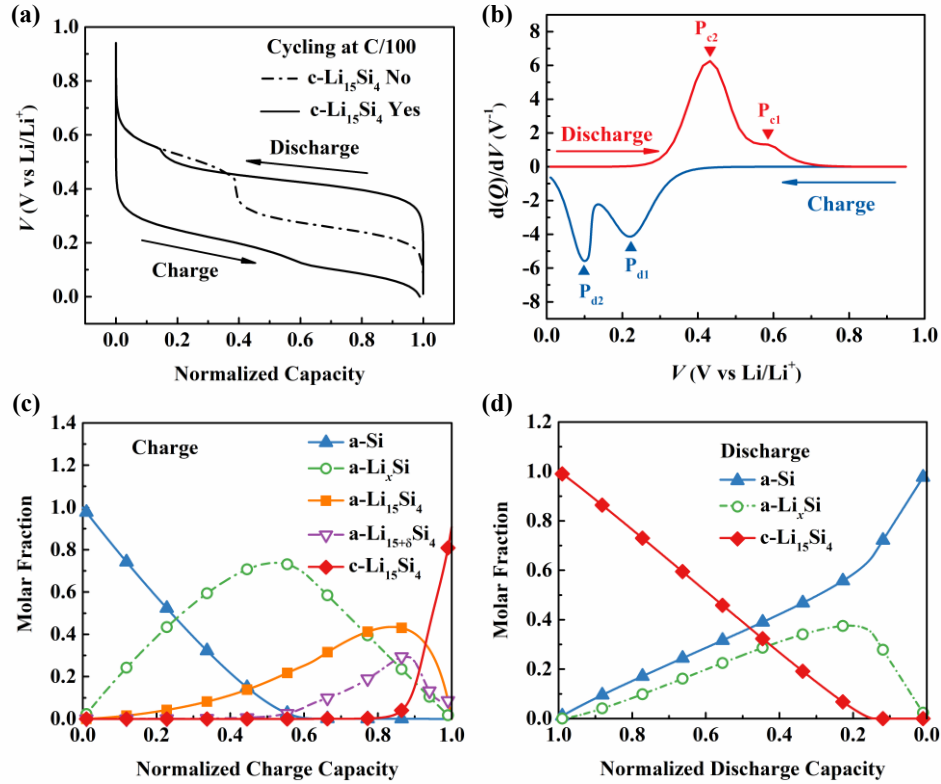


Figure 3-5 Electrochemical behaviors and phase transformations of Si in the presence of crystallization during discharge and charge: (a) voltage curves; (b) differential voltage curves; and composition variations during (c) charge and (d) discharge.

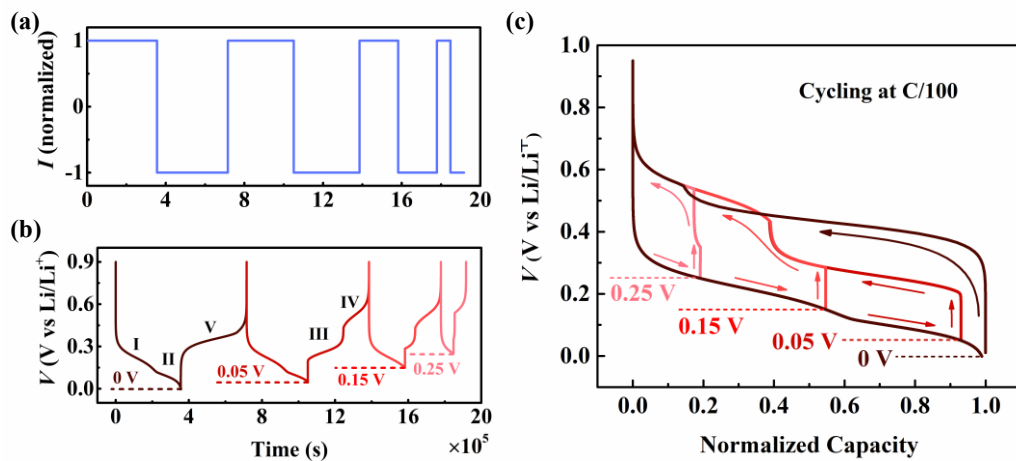


Figure 3-6 Electrochemical behaviors of Si cycled between different voltage limits: (a) current density vs time; (b) voltage vs time; (c) voltage loops.

Figure 3-6 shows the electrochemical behaviors of Si during micro-cycling operation between different voltage limits.

The transition from the lower lithiation voltage branch to the upper lithiation voltage branch for silicon electrodes was well identified and explained by Baker et al. [126] in a slow voltage scan. In Figure 3-6, the silicon electrode is cycled at C/100, and the current is reversed immediately after the lower voltage limit is reached. In Figure 3-6(b), during the first cycle when the voltage falls to 0 V, the silicon electrode undergoes two phase transformation stages I and II, respectively corresponding to the reaction steps 1 and 2. After the current is reversed, the voltage curve presents a distinct plateau V which suggests the amorphization process b4. In the subsequent cycles, at lower voltage limits of 0.05 V, 0.15 V and 0.25 V, the lower voltage branch (lithiation branch) follows the same trace as that in the first cycle, while the higher voltage branch turns to be sigmoidal. The last three cycles do not involve crystallization thus exhibit two sloping plateaus in de-lithiation voltage curves as shown in Figure 3-6(b) and (c), where the stages III and IV respectively correspond to the reaction steps 1 and 2. It is worth mentioning that when the lower voltage limit increases, the first voltage plateau III in the higher voltage trace becomes shorter and can even vanish. This is because the reaction step 2 dominates at lower voltages, and the voltage plateau of the step 2 becomes less observable as the lower voltage limit increases. It is noted that in Figure 3-6(c) the voltage increases abruptly at the step change of the current. This implies that the silicon electrode has not yet reached equilibrium when the voltage limit is reached, the voltage increase is due to the kinetic loss.

3.4.3. Effect of crystallization rate

Figure 3-7(a) and (b) respectively show the effect of crystallization rate constant k_{cryst} on the growth of c-Li₁₅Si₄ and a-Li_{15+ δ} Si₄.

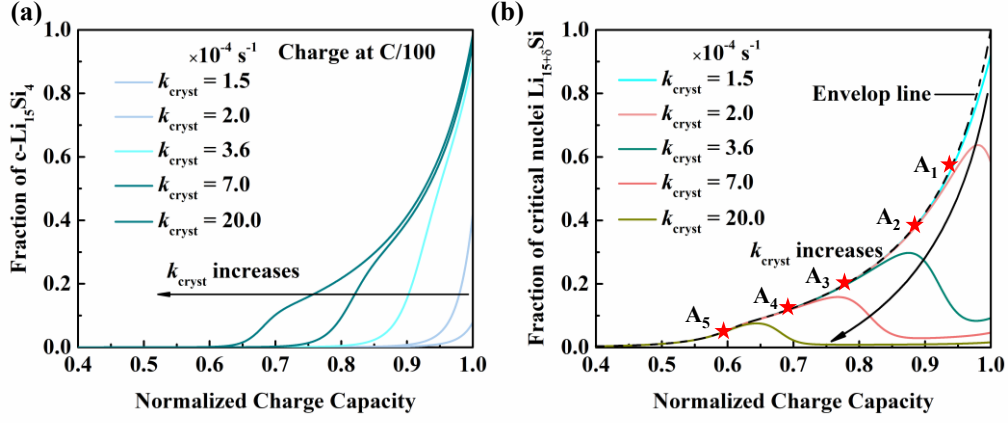


Figure 3-7 The effect of crystallization rate constant on the growth of (a) crystalline phase and (b) critical nuclei during charge.

It is seen in Figure 3-7(a) that the slower the crystallization happens, the more abruptly the crystalline phase will appear. If k_{cryst} is very small ($<0.0002 \text{ s}^{-1}$), as shown in Figure 3-7(b), there will be excessive nuclei due to the slow f4, which lead to an exponential growth in silicon crystalline following the relationship

$$\frac{dx_{\text{cryst}}}{dt} = k_{\text{cryst}} x_{\text{cryst}} \quad (3-22)$$

As k_{cryst} increases to 0.00036 s^{-1} , the reaction rate of step f4 becomes comparable to that of step f3. The growth curve presents a characteristic s-shaped, or sigmoidal profile where the transformation rates are low at the beginning and the end of the process, but fast in between. This s-shaped growth curve is a typical characteristic of homogeneous crystallization [127]. If k_{cryst} is larger than 0.0007 s^{-1} , c-Li₁₅Si₄ grows fast initially until most nuclei are consumed. In this case, the crystallization rate is limited by the nucleation step f3. The envelop line plotted in Figure 3-7(b) is determined by $x_{(3)}/\Delta x_{(3)}$, which is equal to the total fraction of a-Li₁₅₊₈Si₄ and c-Li₁₅Si₄. The intersection points A₁-A₆ in Figure 3-7(b) correspond to the starting points of the appearance of c-Li₁₅Si₄ in Figure 3-7(a), which tend to start earlier with increasing k_{cryst} .

3.4.4. Amorphization with different surface energy barriers

The effects of surface energy barriers are studied in Figure 3-8. As shown in Figure 3-8(a), with increasing E^* , the voltage curve during the discharge process changes from a sloping shape to a flat shape. As E^* is proportional to the extra surface energy barrier to overcome for amorphization, a larger E^* means higher surface energy barrier. When the particle size is smaller, more free surfaces of silicon phases are exposed and the silicon phases are more active on average. This elevated activity means less surface energy barrier per atom to be overcome, corresponding to a smaller E^* . Hence, a sloping voltage curve is expected during the discharge process even if the silicon particle is crystallized. This well explains the effect of particle size, which is consistent with the experimental observations in the literatures.

Figure 3-8(b) indicates that a higher surface energy barrier will shift the voltage peak to a higher level and increase its width. Furthermore, when E^* is large enough, the higher voltage peak will vanish. Hence, only one visible voltage characteristic peak can be detected in the differential analysis even though there are two phase transformation reactions. This may lead to a failure to detect the phase transformation step b2. To unveil the underlying reactions, it is necessary to use other more reliable experimental techniques to complement the results from differential analyses.

Figure 3-8(c) shows that the decrease of crystalline phase is decelerated with increasing E^* because of the slowing down in amorphization. Correspondingly, as shown in Figure 3-8(d), the growth of a-Li_xSi during amorphization also slows down, and the amorphization process can thus last for a longer time.

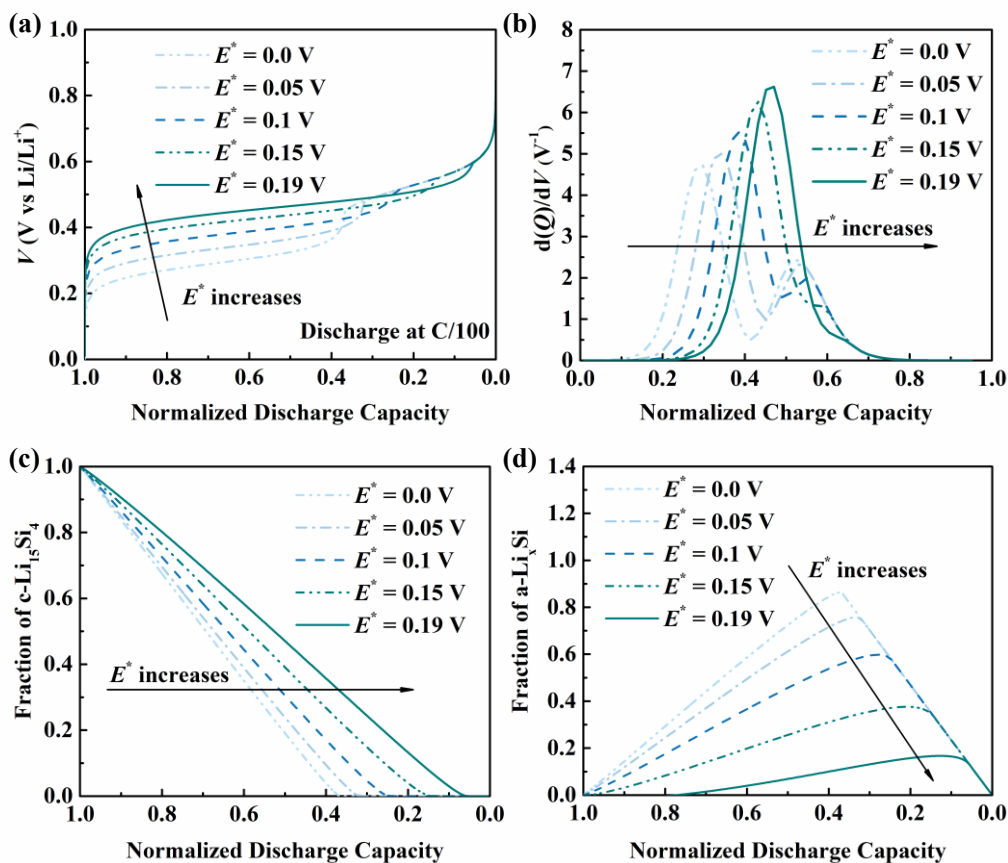


Figure 3-8 (a) Voltage curves, (b) differential voltage curves, and molar fraction variation of (c) $c\text{-Li}_{15}\text{Si}_4$, and (d) $a\text{-Li}_x\text{Si}$ at different values of surface energy barrier during discharge.

3.5. Interim conclusion

A zero-dimensional mechanistic voltage model is developed for silicon anodes in LIBs. The model is able to capture key electrochemical phenomena during cycling of silicon electrodes for the first time, including the sloping voltage curve with voltage hysteresis at small lithiation depths and the shift to a single distinct voltage plateau on discharge from the initial sloping curve upon deep lithiation. Comparisons show a good agreement between the model and experimental results. The processes of phase transformations, crystallization and amorphization underlying the electrode behaviors are resolved in the model. The model correlates the electrochemical behaviors of Si

with the underlying reaction processes in a quantitative manner. It is shown that the voltage hysteresis is path-dependent and the asymmetric hysteresis originates from asymmetric reaction pathways. The model is then used to study the effects of crystallization rate and surface energy barriers. The crystallization rate constant k_{cryst} can affect the shape of the crystalline growth curve, and a lower k_{cryst} will delay the appearance of the crystalline phase. The extra potential increase E^* induced by surface energy barriers between crystalline and amorphous phases is shown to be the underlying cause of the elevated voltage plateau for silicon electrodes. Even though there are two electrochemical reactions, the differential analysis can only detect one visible voltage peak when E^* is large enough. The surface energy barrier also explains qualitatively why smaller silicon particles present a sloping voltage curve even charged to 0 V. The model is a necessary tool for future design and development of high-energy-density, longer-life silicon-based LIBs.

Chapter 4. Modeling the role of Si in Si/Gr composite electrodes

4.1. Introduction

As discussed in the literature review, Si/Gr composite electrodes are commonly used instead of pure silicon electrodes to mitigate the degradation of pure silicon and retain a relatively high energy density, taking advantage of the high specific capacity of Si and the stable structure of Gr. In the experiments, the Si/Gr composite electrodes behave differently from the Si electrodes and Gr electrodes. There is a need for understanding the electrochemical behaviors of composite electrodes and how each active material contributes to the overall performance of composite electrodes. This chapter presents a model for Si/Gr electrodes taking into account different properties and electrochemical kinetics of the individual active materials. The model offers theoretical insights into the interactions between silicon and graphite behaviors and how the competing lithiation/delithiation processes of the two different active materials contribute to the overall performance of Si/Gr blended electrodes with different Si/Gr ratios. In particular, a dimensionless competing factor is proposed to quantify the lithiation/delithiation competition between the two active materials, which can be used to effectively identify the active operating regions of each individual active material and offers a potentially useful indicator for designing cycling protocols for mitigating degradation of Si/Gr electrodes. The developed electrode model can be readily implemented into the existing full-cell models and coupled with other physics to guide further development of lithium-ion batteries with Si-based electrodes. Specifically, this chapter focuses on the following research questions:

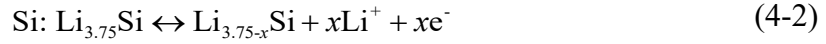
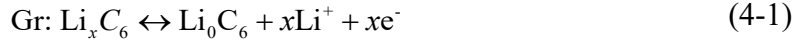
- (1) How does the voltage hysteresis of Si affect the (de)lithiation sequence and process of Si and Gr during cycling?
- (2) What is the effect of the Si/Gr ratio?

(3) To what degree do Si and Gr contribute to the electrochemical behaviors of Si/Gr composite electrodes under different conditions?

This chapter is based on “Yang Jiang, Zhiqiang Niu, Gregory Offer, Jin Xuan, Huizhi Wang*, Insights into the role of silicon and graphite in the electrochemical performance of silicon/graphite blended electrodes with a multi-material porous electrode model, Journal of The Electrochemical Society, 2022, 169 (2) / 020568” [97]. Yang Jiang: Conceptualization, methodology, software, validation, formal analysis, writing - original draft. Zhiqiang Niu: Methodology, software, writing - review & editing, funding acquisition. Gregory Offer: Conceptualization, resources, writing - review & editing, supervision, funding acquisition. Jin Xuan: Writing-review & editing, supervision. Huizhi Wang: Conceptualization, resources, writing - review & editing, supervision, funding acquisition. I made contributions to the model methodology and data curation in another paper here: “Weilong Ai, Niall Kirkaldy, Yang Jiang, Gregory Offer, Huizhi Wang, Billy Wu, A composite electrode model for lithium-ion batteries with silicon/graphite negative electrodes, Journal of Power Sources, 2022, 527 / 231142”. However, it's important to note that these two papers were produced independently without any overlap in other aspects, and my thesis is solely based on the previous one.

4.2. Multi-material electrochemical model

Since the study focuses on Si/Gr electrode behaviors rather than full cell performance, a half cell consisting of a porous Si/Gr electrode as a working electrode (WE) and a non-polarized lithium metal counter electrode (CE) separated by an electrolyte-soaked separator is selected as the computational domain of the study, as shown in Figure 4-1. Different from previous models which treat Si/Gr electrodes as a single “lumped” material, this study considers the lithiation/delithiation reactions of Gr and Si as follows



Crystallization in lithiated Si [128] is not considered here because the crystallization regime is normally avoided in battery operation to prevent huge volume changes and the associated degradation.

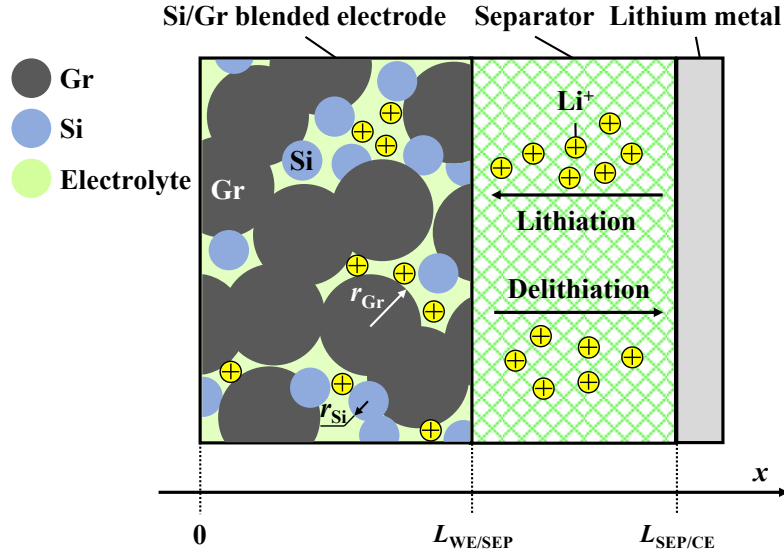


Figure 4-1 Schematics of the computational domain.

The model presented in this study is based on Newman's P2D framework [95] with the porous Si/Gr electrode described using the volume averaged approach, where Si, Gr and electrolyte phases are treated as macro-homogeneous superimposed continua with different physicochemical properties. This is sensible as the size of pores in a typical Si/Gr electrode is significantly smaller than the electrode dimension. For simplicity, the binder effects are neglected. The half-cell process is assumed to be isothermal. The silicon and graphite phases in a same representative volume are assumed to have the same electric potential because of excellent electrical connections.

4.2.1. Reaction kinetics

At the WE, the electrochemical reactions of lithium with the individual active materials (as described in Eqs. (4-1) and (4-2)) are described using Butler-Volmer kinetic equation [95]

$$i_m^{\text{Li}} = i_{0,m} \left(e^{\alpha_{a,m} F \eta_m / RT} - e^{-\alpha_{c,m} F \eta_m / RT} \right) \quad (4-3)$$

where subscript m stands for Si and Gr, i_m^{Li} is the current density (A m^{-2}) of lithium reaction with active material m , $\alpha_{a,m}$ and $\alpha_{c,m}$ are charge transfer coefficients, F is the Faraday constant ($F = 96485 \text{ C mol}^{-1}$), R is the universal gas constant ($R = 8.314 \text{ J mol}^{-1} \text{ K}^{-1}$), T is the temperature (K), and $i_{0,m}$ is the exchange current density (A m^{-2}) for active material m , expressed as

$$i_{0,m} = k_{\text{react},m} F (C_e)^{\alpha_{a,m}} \left(C_{s,m}^{\text{max}} - C_{s,m}^{\text{surf}} \right)^{\alpha_{a,m}} \left(C_{s,m}^{\text{surf}} \right)^{\alpha_{c,m}} \quad (4-4)$$

where $k_{\text{react},m}$ is rate constant, C_e is electrolyte concentration (mol m^{-3}), $C_{s,m}^{\text{max}}$ is the maximum lithium concentration (mol m^{-3}) in active material m , and $C_{s,m}^{\text{surf}}$ is the lithium concentration (mol m^{-3}) at the surface of active material m .

The overpotential on active material m , η_m (V), is defined as the deviation of the potential difference between the solid and liquid phases from the equilibrium potential for that material

$$\eta_m = \phi_s - \phi_e - E_{\text{eq},m} \left(\theta_m^{\text{surf}} \right) \quad (4-5)$$

The dependence of equilibrium potential of material m on the interfacial state of charge (SOC), $E_{\text{eq},m} \left(\theta_m^{\text{surf}} \right)$, is obtained by using linear interpolation/extrapolation of the experimental data as shown in Figure 4-2 [35,120]. In Figure 4-2(a), the experimental open circuit potential (OCP) of Gr obtained at 25°C by Mercer et al. [35] exhibits three distinct voltage plateaus at around 0.21 V, 0.125 V and 0.09 V within the

voltage limits between about 0.05 V and 0.25 V. Since voltage hysteresis of Gr is negligible (less than 0.023 V), an averaged OCP is fitted to the lithiation and delithiation processes. In Figure 4-2(b), the OCP of Si measured by Sethuraman et al. [120] shows two sloping voltage plateaus in both lithiation and delithiation branches with huge voltage gap in between. This path-dependent voltage hysteresis of Si has been demonstrated to be inevitable [128], and two different OCPs are used in our model for lithiation and delithiation processes.

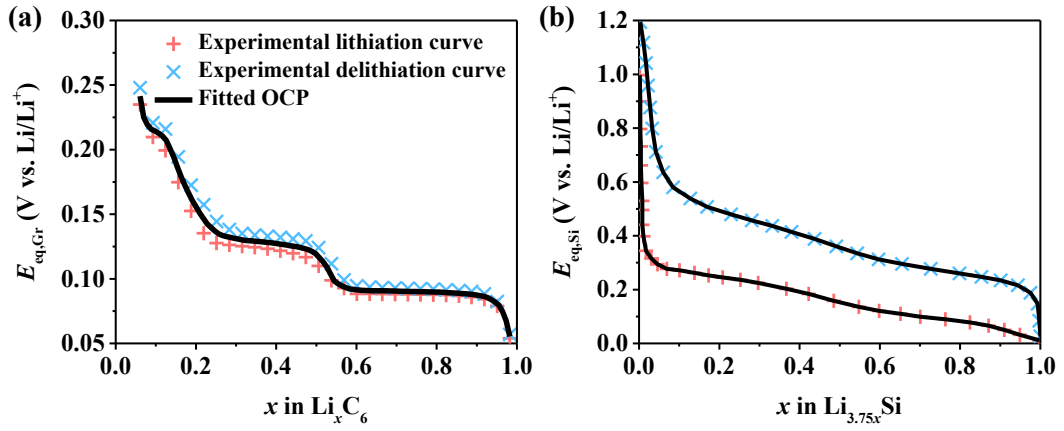


Figure 4-2 Open circuit potentials of (a) Gr and (b) Si as a function of SOC. The experimental data for Gr is taken from Ref. [35] and the experimental data for Si is taken from Ref. [120].

The volumetric current density of the Si/Gr electrode, j^{Li} (A m^{-3}), is the sum of the contributions of the individual active materials

$$j^{\text{Li}} = \sum_m (i_m^{\text{Li}} a_{s,m}) \quad (4-6)$$

where $a_{s,m}$ is the specific surface area for solid particles (m^{-1}), given by

$$a_{s,m} = \frac{3\varepsilon_{s,m}}{r_m} \quad (4-7)$$

where $\varepsilon_{s,m}$ is the volume fraction of active material m , and r_m is the solid particle radius (m).

At the CE, the electrode kinetics is described by [96]

$$i_{\text{CE}} = Fk_{\text{react}}^{\text{CE}} C_e^{0.5} \left(e^{\alpha_{\text{a,CE}} F(\phi_s - \phi_e) / RT} - e^{-\alpha_{\text{c,CE}} F(\phi_s - \phi_e) / RT} \right) \quad (4-8)$$

where $k_{\text{react}}^{\text{CE}}$ is the reaction rate constant ($\text{m}^{2.5} \text{mol}^{-0.5} \text{s}^{-1}$), which is sufficiently high to minimize the polarization at the lithium metal electrode.

The average SOC for the Si/Gr electrode is

$$\theta_{\text{WE}} = \frac{\sum_m (C_{s,m} \varepsilon_{s,m})}{\sum_m (C_{s,m}^{\text{max}} \varepsilon_{s,m})} \quad (4-9)$$

and the specific capacity of the Si/Gr electrode is estimated as

$$\text{cap} = \frac{C_{s,\text{WE}} F \sum_m \varepsilon_{s,m}}{3600 \sum_m (\varepsilon_{s,m} \rho_m)} \quad (4-10)$$

where ρ_m is material density (kg m^{-3}). The volume fractions of active solid materials, Si and Gr, are determined from the mass ratio of Si to Gr ($r_{\text{Si/Gr}}$) and the electrolyte volume fraction (ε_e) in the Si/Gr electrode by

$$\varepsilon_{s,\text{Gr}} + \varepsilon_{s,\text{Si}} + \varepsilon_e = 1 \quad (4-11)$$

$$r_{\text{Si/Gr}} = \rho_{\text{Si}} \varepsilon_{s,\text{Si}} / \rho_{\text{Gr}} \varepsilon_{s,\text{Gr}} \quad (4-12)$$

$C_{s,\text{WE}}$ in Eq. (4-10) is the average lithium concentration in the Si/Gr electrode, given by

$$C_{s,\text{WE}} = \frac{\sum_m (C_{s,m} \varepsilon_{s,m})}{\sum_m \varepsilon_{s,m}} \quad (4-13)$$

4.2.2. Species conservation

The lithium conservation in each active solid phase is given by

$$\frac{\partial (\varepsilon_{s,m} C_{s,m})}{\partial t} = \frac{-a_{s,m} i_m^{\text{Li}}}{F} \quad (4-14)$$

where t is time (s) and a_s is specific surface area of solid particles (m^{-1}).

The lithium flux at the solid/liquid interface is modelled using the two-term polynomial approximation method as previous Li-ion models did [33,94]

$$\frac{D_{s,m}}{l_m} (C_{s,m}^{\text{surf}} - C_{s,m}) = \frac{-i_m^{\text{Li}}}{F} \quad (4-15)$$

where the surface and averaged lithium concentrations are assumed to be linearly related via a diffusion length l_m (m) [33] which depends on the dimensions and the morphology of the electrode particle. For spherical particles, the diffusion length is

$$l_m = \frac{r_m}{5} \quad (4-16)$$

The lithium conservation in the electrolyte is given by

$$\frac{\partial(\varepsilon_c C_e)}{\partial t} = \nabla \cdot (D_e^{\text{eff}} \nabla C_e) + \frac{1-t_+^0}{F} j^{\text{Li}} \quad (4-17)$$

where t_+^0 denotes transference number, and D_e^{eff} is effective electrolyte diffusivity (m^2/s) which is related to bulk electrolyte diffusivity D_e by the Bruggeman correction

$$D_e^{\text{eff}} = D_e \varepsilon_c^{1.5} \quad (4-18)$$

4.2.3. Charge conservation

Since Gr and Si phases are assumed to have the same potential, the charge conservation in solid phase is described by

$$\nabla \cdot (\sigma^{\text{eff}} \nabla \phi_s) - j^{\text{Li}} = 0 \quad (4-19)$$

where σ^{eff} (S m^{-1}) is the weighted average of conductivities of the different active solid materials in the electrode

$$\sigma^{\text{eff}} = \sum_m \sigma_m \varepsilon_{s,m} \quad (4-20)$$

The charge conservation in the electrolyte is given by

$$\nabla \cdot (\kappa^{\text{eff}} \nabla \phi_c) + \nabla \cdot (\kappa_D^{\text{eff}} \nabla \ln C_e) + j^{\text{Li}} = 0 \quad (4-21)$$

where κ^{eff} and $\kappa_{\text{D}}^{\text{eff}}$ are respectively effective ionic conductivity and effective diffusion conductivity corrected in the same way as in Eq. (4-18) to reflect the effects of porosity and tortuosity in porous regions (i.e., the WE and the separator). The bulk ionic conductivity κ is a function of electrolyte concentration and temperature as follows [94]

$$\kappa = 10^{-4} \times C_e \left(\begin{array}{l} -10.5 + 0.668 \cdot 10^{-3} \cdot C_e + 0.494 \cdot 10^{-6} C_e^2 + \\ (0.074 - 1.78 \times 10^{-5} C_e - 8.86 \times 10^{-10} C_e^2) T + \\ (-6.96 \times 10^{-5} + 2.8 \times 10^{-8} C_e) T^2 \end{array} \right)^2 \quad (4-22)$$

The polynomial relationship fitted to the experimental measurements is valid when C_e falls within the range of [0, 4500] mol m⁻³.

κ_{D} is related to κ by

$$\kappa_{\text{D}} = \frac{2RT\kappa}{F} (t_+^0 - 1) \left(1 + \frac{d \ln f_{\pm}}{d \ln C_e} \right) \quad (4-23)$$

where f_{\pm} is the mean molar activity coefficient of the electrolyte.

4.2.4. Boundary and initial conditions

At the WE current collector ($x = 0$), all the current is carried by electrons and no ions pass through, hence, the boundary conditions are defined as follows

$$\left. \frac{\partial C_e}{\partial x} \right|_{x=0} = 0 \quad (4-24)$$

$$\left. \frac{\partial \phi_e}{\partial x} \right|_{x=0} = 0 \quad (4-25)$$

$$\left. \frac{\partial \phi_s}{\partial x} \right|_{x=0} = -\frac{i_{\text{app}}}{\sigma^{\text{eff}}} \quad (4-26)$$

The separator is electrically insulated and there is no flux of electrons, however, ions can pass through the boundaries between the separator and electrodes. At the interface between the WE and separator ($x = L_{\text{WE/SEP}}$), a continuity condition is applied for ion flux, and a zero-flux condition is applied for electrons, giving

$$D_e^{\text{eff}} \frac{\partial C_e}{\partial x} \Big|_{x=L_{\text{WE/SEP}}^-} = D_e^{\text{eff}} \frac{\partial C_e}{\partial x} \Big|_{x=L_{\text{WE/SEP}}^+} \quad (4-27)$$

$$\kappa^{\text{eff}} \frac{\partial \phi_e}{\partial x} \Big|_{x=L_{\text{WE/SEP}}^-} = \kappa^{\text{eff}} \frac{\partial \phi_e}{\partial x} \Big|_{x=L_{\text{WE/SEP}}^+} \quad (4-28)$$

$$\frac{\partial \phi_s}{\partial x} \Big|_{x=L_{\text{WE/SEP}}} = 0 \quad (4-29)$$

where the superscript “-” and “+” for $L_{\text{WE/SEP}}$ means the left and right side of the WE/SEP boundary.

The solid-phase potential is set to be zero at the interface of the separator and the lithium metal electrode ($x = L_{\text{SEP/CE}}$):

$$\phi_s \Big|_{x=L_{\text{SEP/CE}}} = 0 \quad (4-30)$$

The electrolyte potential gradient at $x = L_{\text{SEP/CE}}$ depends on the Faradaic current that is generated by the electrode reactions and the diffusion current that is associated with the electrolyte concentration gradient, given by

$$\frac{\partial \phi_e}{\partial x} \Big|_{x=L_{\text{SEP/CE}}} = -\frac{i_{\text{CE}}}{\kappa^{\text{eff}}} - \frac{\kappa_{\text{D}}^{\text{eff}}}{\kappa^{\text{eff}}} \frac{\partial \ln C_e}{\partial x} \quad (4-31)$$

The lithium flux caused by lithium plating/stripping at the CE is related to the applied current density by [129]

$$\frac{\partial C_e}{\partial x} \Big|_{x=L_{\text{SEP/CE}}} = -\frac{(1-t_+^0)i_{\text{CE}}}{D_e^{\text{eff}} F} \quad (4-32)$$

The initial state of the half-cell is set to be at equilibrium, which means that the reaction rate is zero and the profiles of all the field variables (C_e , $C_{s,m}$, ϕ_s and ϕ_e) stays uniform across the computational domain with their initial values listed in Table 4-1. A consistent initial lithium concentration of $C_{s,m}^{\text{init}}$ is calculated from Eq. (4-5) with an initial overpotential to be zero. All other parameters are calculated self-consistently from chosen values of field variables.

Table 4-1 Parameter values used in base case simulations.

Parameter	Value	Comment/reference
$C_{s,Gr}^{init}$ (mol m ⁻³)	1854 for lithiation; 28405 for delithiation	
$C_{s,Si}^{init}$ (mol m ⁻³)	13025 for lithiation; 310090 for delithiation	
$C_{s,Gr}^{max}$ (mol m ⁻³)	30555	Ref. [94]
$C_{s,Si}^{max}$ (mol m ⁻³)	311000	Ref. [119]
C_e^{init} (mol m ⁻³)	1000	Ref. [94]
δ_{WE} (μm)	35	Ref. [130]
δ_{SEP} (μm)	22	Ref. [105]
ρ_{Gr} (kg m ⁻³)	2267	Ref. [105]
ρ_{Si} (kg m ⁻³)	2329	Ref. [105]
$D_{s,Gr}$ (m ² s ⁻¹)	3.9×10^{-14}	Ref. [94]
$D_{s,Si}$ (m ² s ⁻¹)	3×10^{-16}	Ref. [119]
D_e (m ² s ⁻¹)	7.5×10^{-10}	Ref. [94]
ε_s	0.4824	Ref. [94]
ε_e	0.41 in the working electrode; 0.724 in the separator	Ref. [105]
F (C mol ⁻¹)	96485	
ϕ_e^{init} (V)	0	
ϕ_s^{init} (V)	0.3 for lithiation; 0.085 for delithiation	
$k_{react,Gr}$ (m ^{2.5} mol ^{-0.5} s ⁻¹)	5.031×10^{-11}	Ref. [94]
$k_{react,Si}$ (m ^{2.5} mol ^{-0.5} s ⁻¹)	6×10^{-11}	Estimated
$k_{react,CE}$ (m ^{2.5} mol ^{-0.5} s ⁻¹)	1×10^{-4}	Estimated
α_a	0.5	
α_c	0.5	
R (J mol ⁻¹ K ⁻¹)	8.314472	
r_{Gr} (μm)	2	Ref. [130]
r_{Si} (μm)	0.3	Ref. [130]
σ_{Gr} (S m ⁻¹)	100	Ref. [94]
σ_{Si} (S m ⁻¹)	33	Ref. [119]
t_+^o	0.364	Ref. [94]
Lower voltage limit of Gr, $V_{low,Gr}$ (V)	0.056	
Lower voltage limit of Si, $V_{low,Si}$ (V)	0.012 for lithiation; 0.08 for delithiation	
Higher voltage limit of Gr, $V_{high,Gr}$ (V)	0.241	
Higher voltage limit of Si, $V_{high,Si}$ (V)	0.8 for lithiation; 1.2 for delithiation	
T (K)	298.15	

4.2.5. Numerical procedures and model parameters

The model consists of differential equations Eqs. (4-14) (4-17) (4-19) and (4-21) for $(m + 3)$ unknown field variables: $C_{s,m}$, C_e , ϕ_s and ϕ_e . Key performance metrics such as η_m , $i_{0,m}$, i_m^{Li} , i_{CE} and i^{Li} are further determined using Eqs. (4-3)-(4-8) with the values of field variables solved from the differential equations. The differential equations were discretized by a finite volume method and solved using a general-purpose computational fluid dynamics code implemented in OpenFOAM. The programming flow-chart of the solver is shown in Figure A2-1. A multidomain method is used to create the calculation fields and meshes based on the transient solver ChtMultiRegionFoam. All field variables are initialized to ensure self-consistency at any given initial equilibrium state of the battery. The PIMPLE (PISO-SIMPLE) algorithm is used to iteratively solve the model equations in sequence until the tolerance (10^{-6}) of all the physical quantities is met. The calculation proceeds to the next time step in the main loop until the stop criteria are triggered. For galvanostatic conditions, the cut-off voltages and the bounds of state of charge are two major stop events. The grid and time-step independence tests were performed, and the time step of 1ms and grid size of $1\mu\text{m}$ are employed. The values of model parameters used for base case simulations are summarized in Table 4-1, most of which are from the experimental work by Moyassari et al. [130] and simulation work in Ref. [94,119].

4.3. Results and discussion

4.3.1. Model-experiment comparison

This model is validated by comparing the simulation results with experimental measurements at different Si/Gr mass ratios [130]. As shown in Figure 4-3, the simulation results are in good agreement with the experimental data: all voltage curves during the lithiation/delithiation exhibit three distinct characteristic plateaus in line with

those of Gr, and the sloping-shaped voltage curves are observed at high voltage range (above 0.25 V) in accordance with the features of Si. Some slight discrepancies are noticed between the simulated curves and the measured ones. Figure 4-3(a) shows that the simulated curves shift to slightly higher specific capacities compared to the experimental data, particularly when Si content is high ($r_{\text{Si/Gr}} > 07:88$). This can be explained by Si-related degradation during the experiments, which are not included in our model. Another difference in Figure 4-3(a) is that the experimental curves have a voltage plateau at around 0.4 V, while the simulated curves do not have such a plateau. This voltage plateau is related to the amorphization of crystalline $\text{Li}_{3.75}\text{Si}$, as detailed in previous work [45,128]. Since the crystallization in lithiated Si is not considered in the present model, the simulated delithiation curves cannot reflect this feature. Finally, in the lithiation curves in Figure 4-3(b), the simulated voltage plateaus of Gr are a slightly higher than those measured in experiments, especially those below 0.15 V. This small deviation can be caused by the OCP curve of Gr used in the model, which is taken from Mercer et al. [35] to complement the missing part of the OCP curve in Ref. [130].

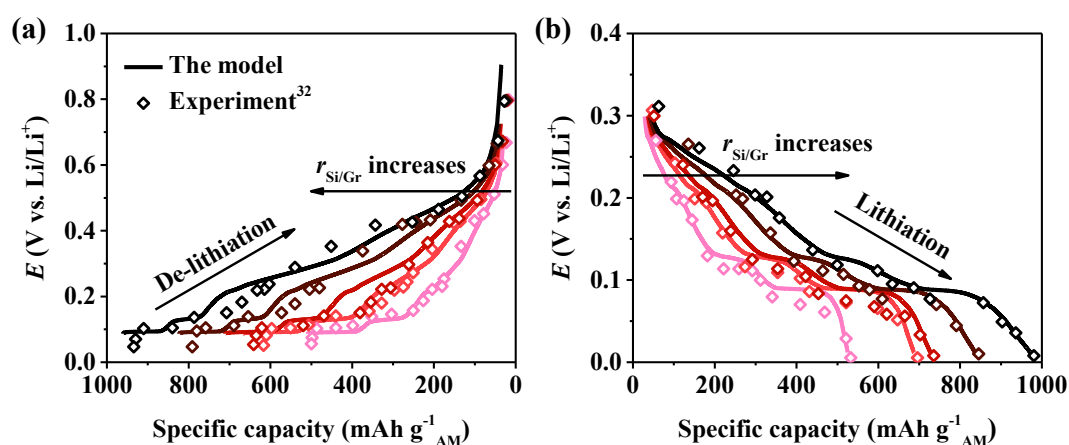


Figure 4-3 Comparison of simulated and experimental voltage curves of Si/Gr blended electrodes with different Si/Gr mass ratios ($r_{\text{Si/Gr}} = 05:90, 07:88, 10:85, 15:80$ and $20:75$) during (a) delithiation and (b) lithiation. Both the experiments and simulations run at $1/20$ C.

The same set of parameter values are used in the case studies in the following sections. All the simulations run at 1C unless specified, and the geometric configuration of the blended electrode including the thickness and the porosity is fixed. The particle sizes of Gr and Si are 2 μm and 0.3 μm respectively [130].

4.3.2. Charge/discharge behaviors of Si/Gr electrodes with different Si/Gr ratios

Figure 4-4(a) and (b) compare the charge/discharge characteristics of Si/Gr electrodes with different Si/Gr mass ratios. For comparison purposes, the voltage curves of pure Si and pure Gr at 1C are also plotted. Not surprisingly, the specific capacity of the Si/Gr electrode increases with increasing Si content. As $r_{\text{Si/Gr}}$ increases from 0.01 to 1.0, the specific capacity changes from 380 to 1910 $\text{mAh g}^{-1}_{\text{AM}}$. This is because the theoretical capacity of Si is much higher than that of Gr, referring to the maximum lithium concentrations of Si and Gr in Table 4-1. It is noted that a higher Si content in the blended electrode weakens the characteristic voltage plateaus of Gr and leads to sloping shaped curves. At $r_{\text{Si/Gr}} < 0.1$, the voltage curves show three distinct plateaus of Gr respectively at 0.21 V, 0.125 V and 0.09 V (respectively denoted by Gr1, Gr2 and Gr3 in Figure 4-4). However, these plateaus become less obvious at $r_{\text{Si/Gr}}$ higher than 1.0. This is consistent with the experimental observations by Moyassari et al. [130].

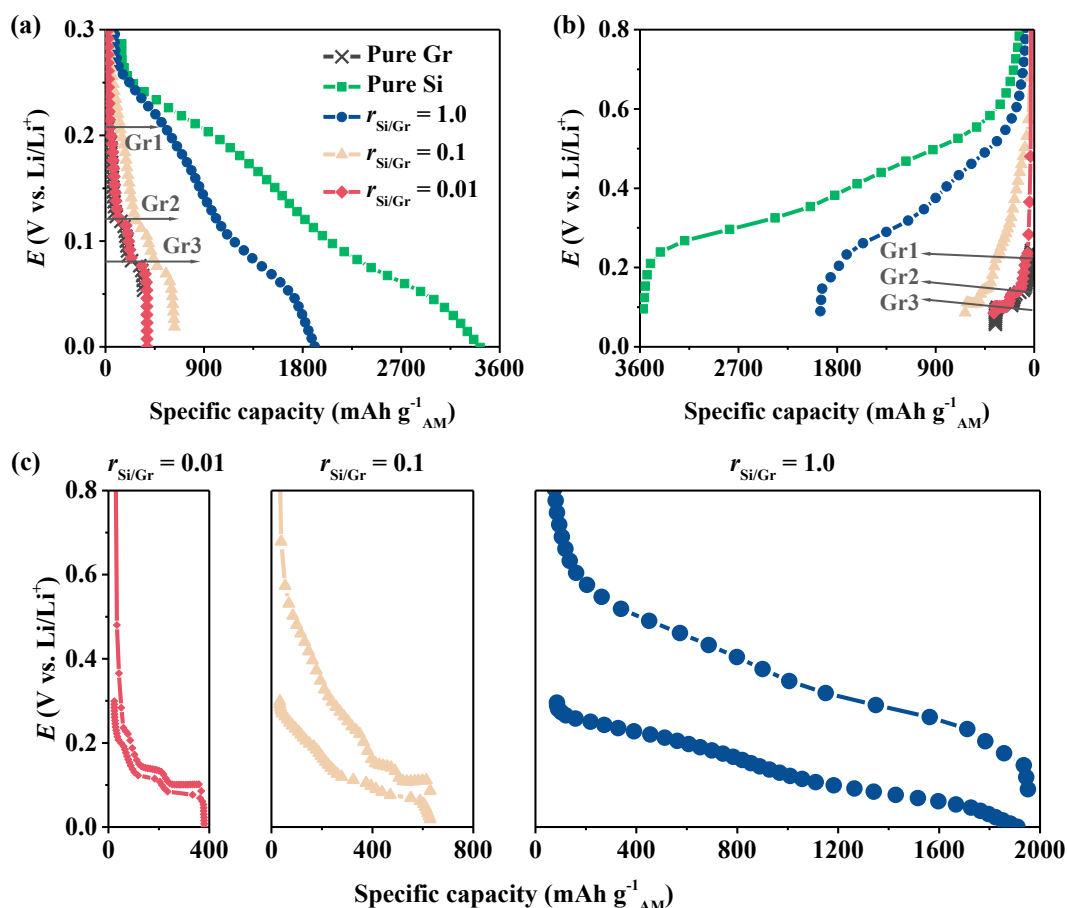


Figure 4-4 Electrochemical behaviors of Si/Gr blended electrodes with different Si/Gr mass ratios during (a) lithiation and (b) delithiation, and (c) voltage hysteresis of the Si/Gr electrodes.

During delithiation, interestingly, there are slight increases in the voltage plateaus of Gr with increasing Si content. However, no changes of these plateaus can be found in the lithiation voltage curves. The plateau shift phenomenon can be attributed to the voltage hysteresis of Si. As shown in Figure 4-2, the voltage hysteresis results in a big difference in voltages of Si during lithiation (< 0.3 V) and delithiation (> 0.3 V). However, the lithium reactions with Gr happen mostly below 0.23 V, which is lower than the delithiation voltages of Si. Therefore, the delithiation of the Si/Gr electrode starts from Gr particles at electrode potential lower than 0.23V, that is, the current density of Gr contributes to nearly all the current density of the blended electrode at

lower voltages. Because higher Si contents give greater current densities of electrodes, the current density of Gr increases when Si content increases. The increased Gr current density results in an increased overpotential of Gr, which shifts the plateaus of Gr to higher voltages. During lithiation, the voltage range of Si covers that of Gr, and reaction rates of Si and Gr are comparable for various $r_{\text{Si/Gr}}$ values. Hence, Si and Gr equally contribute to the overall current density, and the overpotentials of Gr at different $r_{\text{Si/Gr}}$ values have no big difference.

Figure 4-4(c) shows voltage hysteresis of Si/Gr electrodes at different $r_{\text{Si/Gr}}$. It is found that the voltage gap between lithiation and delithiation increases with increasing Si content, especially at lower SOC levels.

4.3.3. Concentration and potential distributions in Si/Gr electrodes

Figure 4-5 shows the potential and concentration distributions across the thickness of the half-cell during lithiation at $r_{\text{Si/Gr}} = 0.1$.

Figure 4-5(a) shows a linear distribution of the electrolyte concentration, C_e , in the separator domain, while it exhibits a downward convex shape in the WE domain due to the lithium consumption at the WE. The electrolyte concentration has a rapid response to time and reaches a steady distribution through the thickness of the half-cell after ~ 10 s.

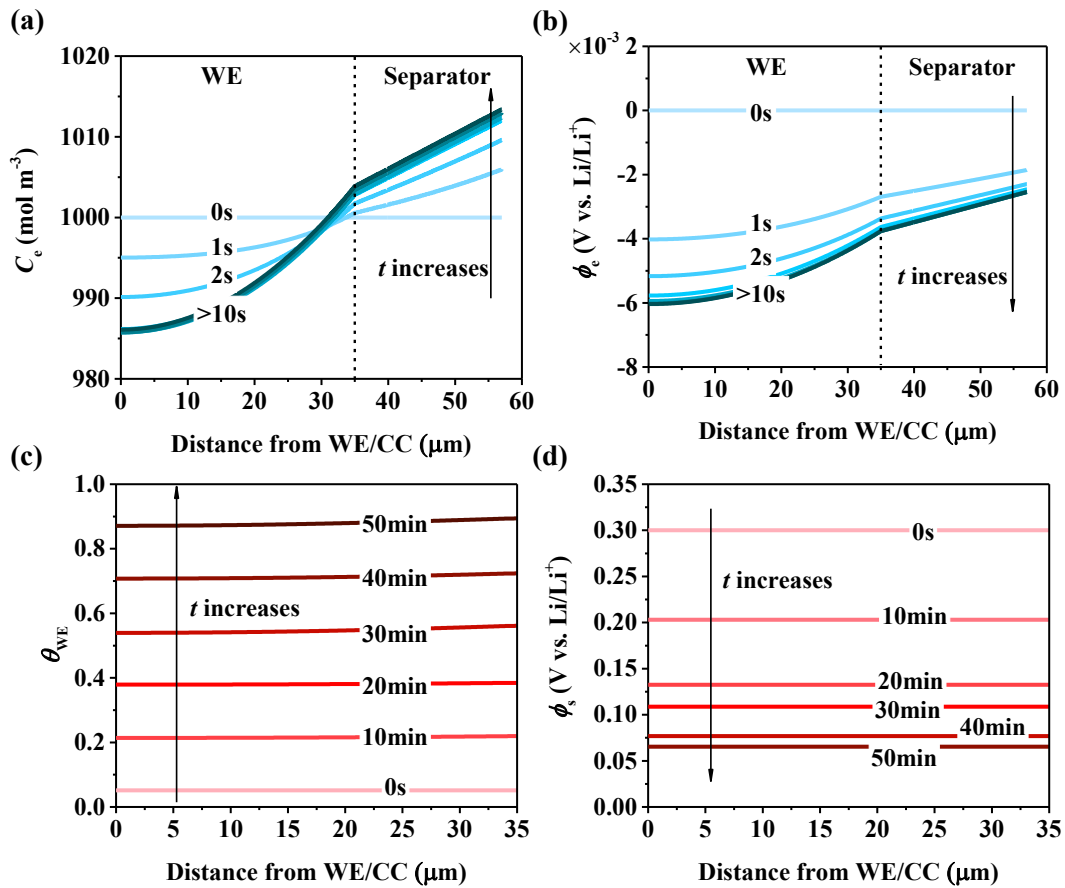


Figure 4-5 Distributions of (a) electrolyte concentration, (b) electrolyte potential, (c) state of charge and (d) solid-phase potential across the thickness of the half-cell domain during lithiation at $r_{\text{Si/Gr}} = 0.1$.

Figure 4-5(b) shows that the electrolyte potential drops from the CE side to the WE side, suggesting that the ionic current and the lithium-ions flow from the lithium metal electrode to the Si/Gr electrode during lithiation. The distribution of electrolyte potential ϕ_e is almost linear across the separator as the ionic conductivity remains almost constant through the thickness of the separator. Within the WE domain, the electrolyte potential exhibits a downward convex shape due to lithium consumption during lithiation. The electrolyte potential drops with time and it approaches a dynamic equilibrium after ~ 10 s. Figure 4-5(c) shows that the averaged state of charge in the WE domain rises during lithiation process. The state of charge in the WE is higher at the side approaching to the separator, although this variation is not obvious in this case

because of little fluctuation of reaction rate through the thickness of the WE. In Figure 4-5(d), the electrode potential ϕ_s is nearly uniform in the WE domain due to the high electrical conductivity of the solid phases. The electrode potential decreases as time increases during lithiation.

4.3.4. (De)Lithiation competition between Si and Gr at different Si/Gr ratios

The lithiation/delithiation processes of Si and Gr during cycling of Si/Gr electrodes with different Si/Gr ratios are shown in Figure 4-6. Figure 4-6(a1)-(a2) show the case at $r_{\text{Si/Gr}} = 0.1$, where Si and Gr have roughly equal contributions to the total capacity of the Si/Gr electrode. The lithiation process can be separated into seven stages, as labelled by L1-L7 in Figure 4-6(a1). From the figure, it can be seen that the lithiation starts with Si in stage L1 at electrode potentials > 0.225 V, and Gr becomes dominant in the lithiation reaction in the later stages after the potential drops below 0.225 V. In stage L2, the contribution of Gr increases fast while the increase in Si contribution slows down. This is because of the phase transition in the lithiated Gr (reflected by the voltage plateau). There are two additional voltage plateaus of Gr in Stages L4 and L6, where the lithiation rate of Gr accelerates. In the intermediate stages L3 and L5, Si dominates in the lithiation reaction of the electrode, giving a fast increase in capacity. In stage L7, Gr reaches its lower cut-off potential, while Si still has capability to accept more lithium until the potential drops to nearly 0 V. As shown in Figure 4-6(a2), delithiation of Si/Gr electrodes happens sequentially first from Gr at high SOC levels and then from Si at low SOC levels. We divide the delithiation process into six stages. In the first three stages D1, D2 and D3, delithiation is mostly contributed by Gr whereas the capacity of Si has no obvious decline. The contribution of Si becomes comparable to that of Gr in stages D4 and D5 after the second voltage plateau of Gr. Graphite reaches its high voltage limit in stage D6 and its delithiation ends, while Si plays a dominant role in this

stage of delithiation with a linear drop in its capacity. It is worth noting that the asymmetric behaviors in lithiation and delithiation shown in Figure 4-6(a1)-(a2) are attributed to the voltage hysteresis of Si. These results agree well with the in-operando EDXRD results from a Si/Gr electrode with $r_{\text{Si/Gr}} = 0.15$ reported by Yao et al. [65].

The profile of the reaction competition between Si and Gr is dependent on Si/Gr ratios. At $r_{\text{Si/Gr}} = 0.01$ where the total maximum capacity of Si is approximately 10% of that of Gr, the capacity of Gr during lithiation increases linearly over the whole range of SOC except for a small region at the beginning of the lithiation process (Figure 4-6(b1)). During delithiation as shown in Figure 4-6(b2), graphite dominates for most of the SOC range, while the capacity of Si decreases slowly till the SOC of the Si/Gr electrode drops below 20%. Figure 4-6(c1)-(c2) show the capacity variations of Si and Gr during cycling when the total maximum capacity of Si is ~ 10 times that of Gr ($r_{\text{Si/Gr}} = 1.0$). Si dominates the electrode reaction over the whole SOC range, and Gr is only active in the SOC range from 30% to 85%. During delithiation, it is found in Figure 4-6(c2) that Gr dominates the contribution within the initial $\sim 20\%$ SOC range and Si dominates for the remaining 80% SOC. By comparing Figure 4-6(a1), (b1) and (c1), the active SOC range for Si is found to increase with increasing Si content. It is found in Figure 4-6(a2), (b2) and (c2) that the Si/Gr ratio does not affect the Si/Gr delithiation sequence. However, the active SOC range for Gr decreases with increasing Si content.

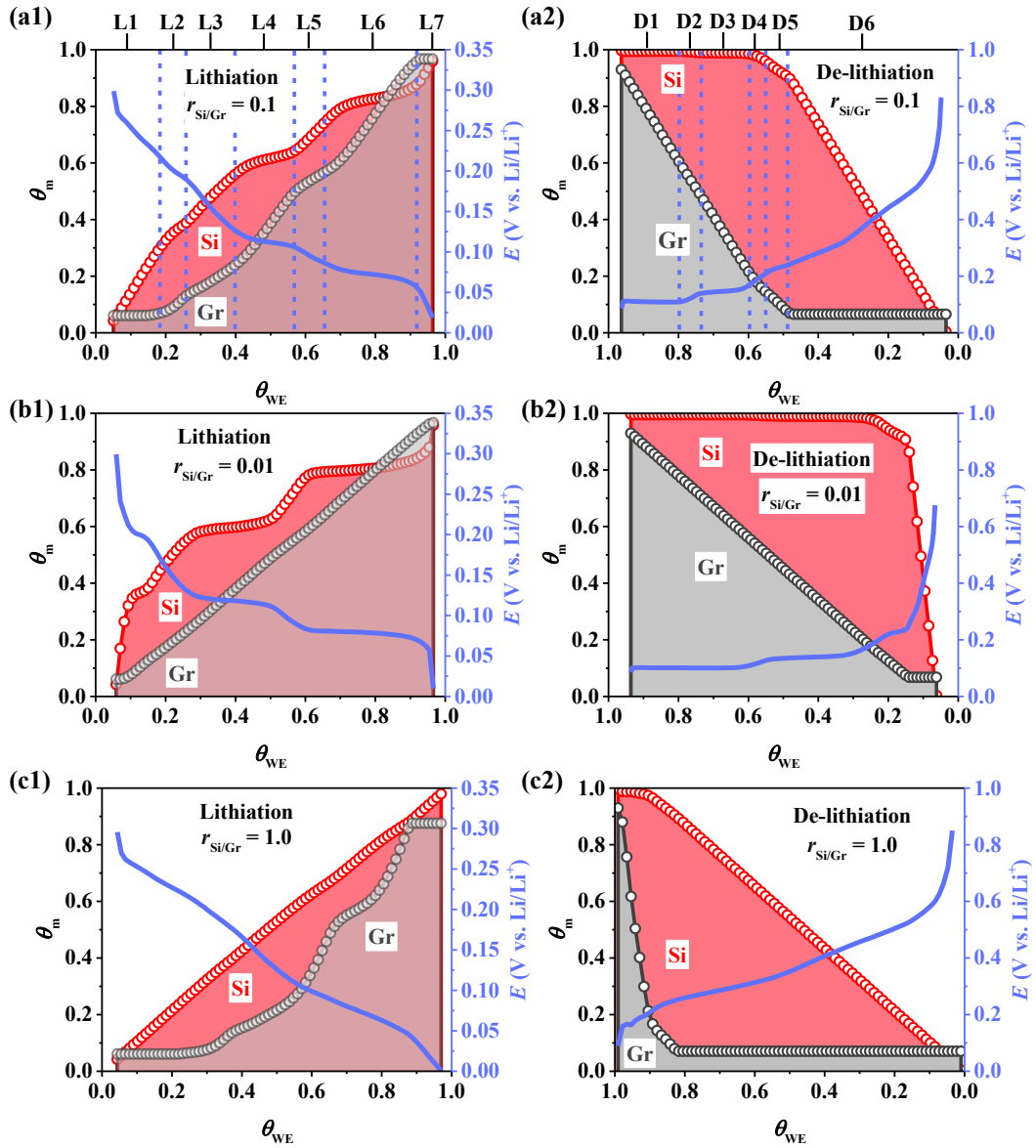


Figure 4-6 SOC variation in Si and Gr during lithiation and delithiation of electrodes with (a) $r_{\text{Si/Gr}} = 0.1$, (b) $r_{\text{Si/Gr}} = 0.01$ and (c) $r_{\text{Si/Gr}} = 1.0$.

4.3.5. Dimensionless competing factor and its implications for strategies for mitigating Si/Gr electrode degradation

To quantify the competition between Si and Gr, a dimensionless “competing factor” is proposed by analyzing the expression of the electrode current density below

$$\begin{aligned}
i_{\text{app}} &= \frac{\delta_{\text{WE}} \left(C_{\text{s,Gr}}^{\text{max}} \varepsilon_{\text{s,Gr}} + C_{\text{s,Si}}^{\text{max}} \varepsilon_{\text{s,Si}} \right) F c_{\text{rate}}}{3600} & (4-33) \\
&= \frac{\delta_{\text{WE}} F c_{\text{rate}} C_{\text{s,Gr}}^{\text{max}} \varepsilon_{\text{s,Gr}}}{3600} + \frac{\delta_{\text{WE}} F c_{\text{rate}} C_{\text{s,Si}}^{\text{max}} \varepsilon_{\text{s,Si}}}{3600} \\
&= \tilde{i}_{\text{Gr}} + \tilde{i}_{\text{Si}}
\end{aligned}$$

where δ_{WE} is the thickness of the working electrode (m). As derived in Eq. (4-33), the overall current density of the Si/Gr electrode can be split into two parts, \tilde{i}_{Gr} and \tilde{i}_{Si} , each proportional to the maximum capacity of the corresponding active material. This means that, if Gr and Si are operating at a current density of \tilde{i}_{Gr} and \tilde{i}_{Si} respectively, they will have the same time rate of state of charge change ($d\theta/dt$) as shown below

$$\frac{d\theta_{\text{Gr}}}{dt} = \frac{\tilde{i}_{\text{Gr}}}{C_{\text{s,Gr}}^{\text{max}} \varepsilon_{\text{s,Gr}} \delta_{\text{WE}} F} \text{ for graphite} \quad (4-34)$$

$$\frac{d\theta_{\text{Si}}}{dt} = \frac{\tilde{i}_{\text{Si}}}{C_{\text{s,Si}}^{\text{max}} \varepsilon_{\text{s,Si}} \delta_{\text{WE}} F} \text{ for silicon} \quad (4-35)$$

Combining Eqs. (4-33)-(4-35) yields

$$\frac{d\theta_{\text{Gr}}}{dt} = \frac{d\theta_{\text{Si}}}{dt} \quad (4-36)$$

Hence, \tilde{i}_{Gr} and \tilde{i}_{Si} are essentially the current densities that lead to the same (de)lithiation rate for Gr and Si. The dimensionless “competing factor” can thus be defined by

$$\chi_{\text{m}} = \frac{a_{\text{s}} i_{\text{m}}^{\text{Li}} \delta_{\text{WE}}}{\tilde{i}_{\text{m}}} \quad (4-37)$$

The reaction rates of Gr and Si are comparable when $\chi_{\text{m}} = 1$, and the electrochemical reaction of active material m is dominant over the other when $\chi_{\text{m}} \gg 1$.

Figure 4-7 plots the competing factor against the electrode potential for all the cases in Figure 4-6. The peaks/valleys of the competing factor curves indicate phase transitions in the active electrode materials.

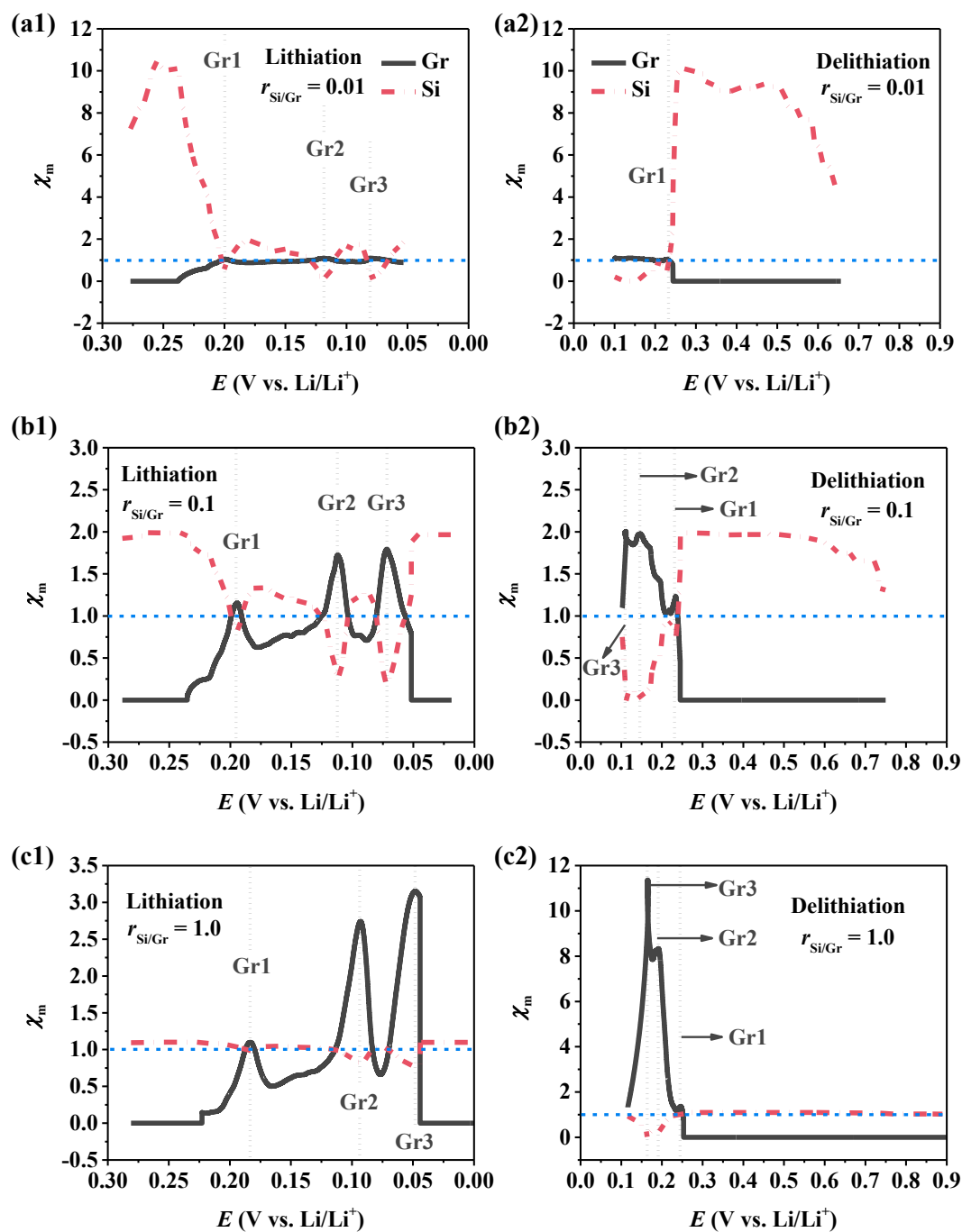


Figure 4-7 Competing factors as a function of electrode potential during lithiation and delithiation of electrodes with (a) $r_{\text{Si/Gr}} = 0.1$, (b) $r_{\text{Si/Gr}} = 0.01$ and (c) $r_{\text{Si/Gr}} = 1.0$.

It is shown in Figure 4-7(a1), (b1) and (c1) that there are three voltage regions where the graphite reaction dominates over the Si reaction during lithiation. The three distinguished peaks of χ_{Gr} (corresponding to the three valleys of χ_{Si}) are the three phase transition processes in Gr at around 0.2, 0.12 and 0.075 V, and the peaks gradually shift

to lower electrode potentials with increasing $r_{\text{Si/Gr}}$. In Figure 4-7(a2), (b2) and (c2), the competing factor of Gr during delithiation exceeds 1 at $E < 0.24$ V, indicating the electrode delithiation is dominated by graphite reaction. Compared to the capacity curves in Figure 4-6, it is demonstrated in Figure 4-7 that the newly defined competing factor offers a more intuitive indicator for identifying the dominant material and its associated active regions. The competing factor can be sensitive to the variations in reaction rates because it reflects the derivative of capacity to time.

Since Si has a much higher degradation rate than Gr, degradation of Si/Gr electrodes can be mitigated by avoiding intensive use of Si. The competing factor can therefore be used for the design of cycling strategies for mitigating electrode degradation. To demonstrate this potential application of the competing factor, microcycles are selected for the Si/Gr electrode with $r_{\text{Si/Gr}} = 0.1$ based on its χ_m distributions (Figure 4-7(b1) and (b2)) and analyzed in detail. Since the competing factor curves in Figure 4-7(b2) suggest that Si is less active at $E < 0.24$ V, the Si/Gr electrode is cycled between 0.01 V and 0.24 V to reduce the use of Si. As shown in Figure 4-8(a), the Si/Gr electrode is firstly fully lithiated to around 0.01 V, and then the delithiation proceeds from an equilibrium state until the electrode potential reaches 0.24 V during the first cycle. The second lithiation starts immediately after the first cycle until the voltage drops to 0.01 V, followed by a delithiation process to increase the voltage back to 0.24 V. In contrast to the first cycle, it is found that the electrode potential overshoots at the onset of the lithiation and delithiation processes during the second cycle due to the voltage hysteresis of Si. The voltage hysteresis of Si (as shown in Figure 4-2(b)) will lead to two remarkably different equilibrium potentials of Si for lithiation and delithiation processes even at the same state of charge. Take the onset of the lithiation of cycle 2 for example, if the current density is reversed abruptly, Si turns

to be far from its equilibrium state due to the immediate change in its OCP. As the equilibrium potential of Si drops from the delithiation branch to the lithiation branch (referring to Figure 4-2(b)), the electrode potential also overshoots towards its equilibrium.

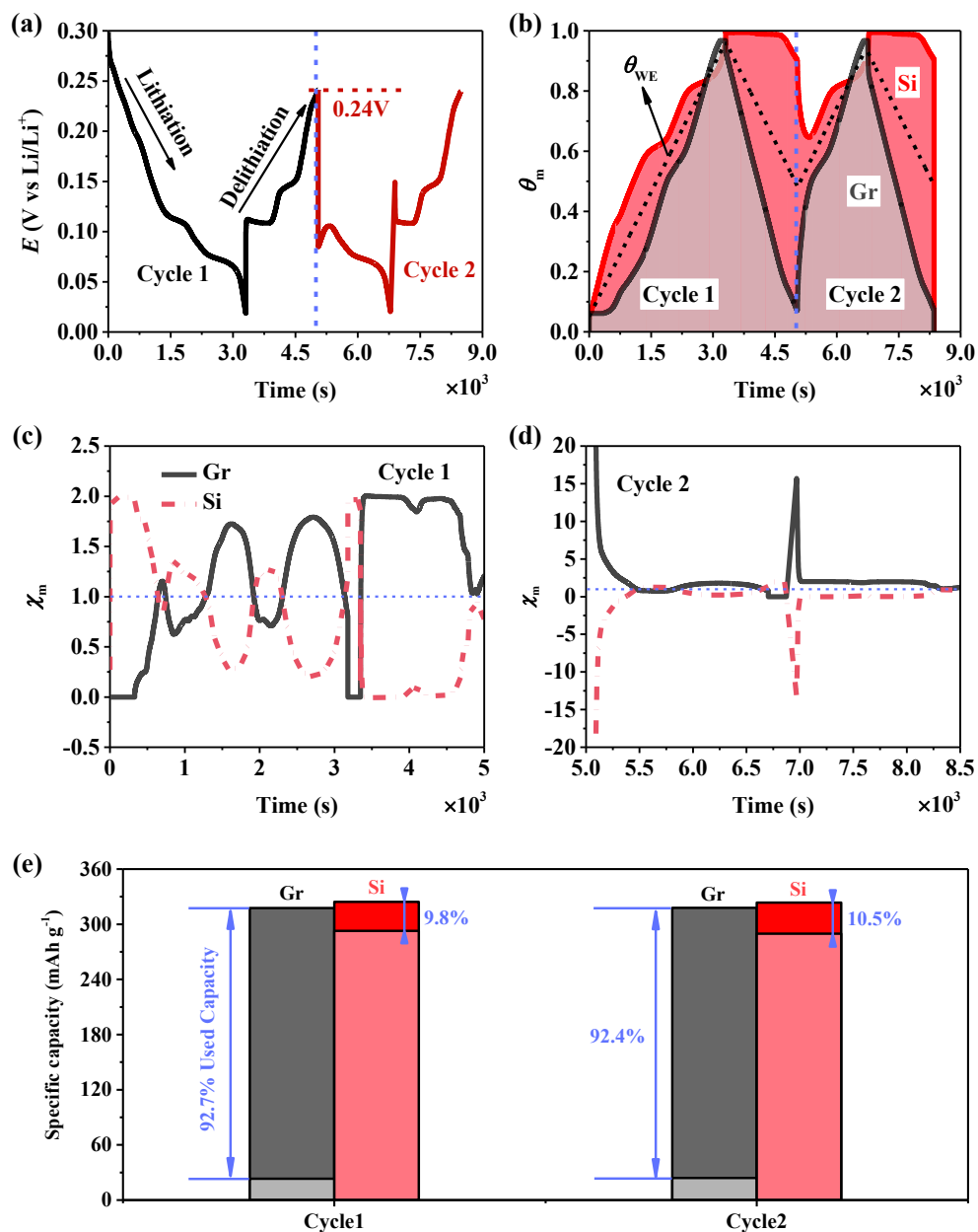


Figure 4-8 Galvanostatic micro-cycling of the Si/Gr electrode with $r_{\text{Si/Gr}} = 0.1$: (a) voltage, (b) SOC, (c) competing factors in the first cycle and (d) competing factors in the second cycle as a function of time, and (e) capacity usage for Si and Gr during the two successive micro cycles.

Figure 4-8(b) shows that the Si capacity declines at the beginning of cycle 2, and Si has not yet reached its equilibrium. Due to the galvanostatic condition, the state of charge for the Si/Gr electrode (θ_{WE}) climbs and declines linearly back and forth during the two cycles, while θ_{Si} is limited between 0.6 to 1.0 following this cycling scheme in cycle 2.

Figure 4-8(c) and (d) further examines the variations of the competing factors during the two cycles. Consistent with the results in Figure 4-7(b1) and (b2), it is shown in Figure 4-8(c) that graphite dominates the whole delithiation process. Compared to the first cycle, the competing factor of Gr in Figure 4-8(d) exceeds 1 almost during the whole lithiation and delithiation processes, indicating that the electrode capacity with this cycle scheme mainly comes from Gr. Figure 4-8(e) compares the maximum capacity contribution of Gr and Si and their actual capacity usages during both cycles. It is found that ~92% of the graphite capacity is used during micro cycling, whereas Si only contributes ~10% of its capacity to the overall electrode capacity. The micro cycle results suggest there are opportunities to design cycling strategies that can avoid excessive usage of Si capacity, thus mitigating electrode degradation.

4.4. Interim conclusion

A multi-material model is developed for Si/Gr blended electrodes with detailed descriptions of the contributions of the individual active materials during the cycling of electrodes. The model takes into account different properties and electrochemical reactions of the different active materials, and shows good agreement with both electrochemical measurements and in-operando EDXRD profiling. Based on the model, the charge/discharge characteristics of Si/Gr electrodes with different Si/Gr ratios are studied. Results show that Si additives can significantly enhance the specific capacity of Si/Gr electrodes, and the electrochemical features of Gr become less obvious with

increasing Si content. Si can also introduce voltage hysteresis for Si/Gr electrodes and consequently a “plateau shift” during delithiation of blended electrodes. The contributions of the individual active materials to the capacity of blended electrodes are analyzed. It is found that lithiation starts with Si and the lithiation reaction rate of Gr is comparable to that of Si at high SOC levels of Si/Gr electrodes. Delithiation occurs preferentially from Gr at high SOC levels, whereas Si dominates the electrode delithiation at lower SOC levels. Si/Gr ratio can affect the active SOC regions for the individual materials: increasing material content will increase the active SOC range for that material. A dimensionless competing factor is introduced to quantify the relative contribution of each active material, which is demonstrated to be an effective parameter for identifying the active regions of the individual materials. Micro cycling studies suggest that the competing factor can be used to design cycling strategies for mitigating degradation of Si/Gr electrodes. The multi-material model can be readily implemented into full-cell models and coupled with other physics to guide further development of lithium-ion batteries with Si-based electrodes.

Chapter 5. Modelling the thermal behaviors of Si/Gr electrodes

5.1. Introduction

In previous chapters, the electrochemical behaviors of Si/Gr composite electrodes have been studied. The thermal behavior and electrochemical behavior are interdependent on each other. As discussed in the literature review, the thermal behaviors of Si/Gr blended electrodes are observed as a superposition of contributions from both Si and Gr. However, this feature has never been retrieved in any modelling study. Therefore, this chapter establishes a thermally coupled electrochemical model for Si/Gr composite electrodes, which is able to differentiate the thermal characteristics and behaviors of each active material.

The following research questions are answered based on the thermally coupled electrochemical model:

(1) How do Si and Gr affect the overall thermal behaviors of the composite electrode, especially the thermal peaks which have been observed in the experimental results?

(2) How will the thermal behaviors be affected by silicon fraction, C-rate and exterior heat transfer coefficient?

Part of this chapter is based on “Zirui Shao, Yang Jiang*, Gregory J Offer, Huizhi Wang, Modeling of the Thermal Behaviors of Silicon/Graphite Composite Electrodes for Lithium-ion Batteries, Energy Proceedings, 2022, 2004 / 2965” [131]. Zirui Shao: Methodology, Software, Formal analysis, Writing - original draft, Visualization. Yang Jiang: Conceptualization, Supervision, Methodology, Software, Formal analysis, Writing - original draft, Visualization, Project administration. Gregory Offer: Supervision, Writing – review & editing, Project administration. Huizhi Wang:

Conceptualization, Supervision, Writing – review & editing, Funding acquisition, Project administration.

5.2. Electrochemical-thermal coupled multimaterial electrode model

5.2.1. Thermal equations and boundary conditions

This research focuses on the thermal behaviors of Si/Gr electrodes, for simplicity, a half cell model is constructed with a Si/Gr electrode as a working electrode (WE), and Li metal as a reference and counter electrode (CE). A separator soaked with electrolyte is seated between two electrodes. The transport limiting effect incurred by Li metal electrode is negligible because it has significantly higher rate constant than Gr and Si.

The following energy conservation equation is added to the multi-material electrochemical model detailed in the previous chapter to calculate the temperature field T (K) [132]

$$\rho C_p \frac{\partial T}{\partial t} = \frac{\partial}{\partial x} \left(\lambda \frac{\partial T}{\partial x} \right) + \dot{Q}_{\text{gen}} \quad (5-1)$$

where ρ (kg m^{-3}) represents the density of different battery components; C_p ($\text{J kg}^{-1} \text{K}^{-1}$) refers to the specific heat capacity; λ ($\text{W m}^{-1} \text{K}^{-1}$) is the thermal conductivity; while \dot{Q}_{gen} (W m^{-3}) means the total heat generation rate.

There are generally three heat generation components including reversible, irreversible and ohmic heat generations. The heat generation of Li metal is ignored because of its small reaction entropy variation and negligible overpotential during lithiation/delithiation as a reference electrode [75]. The irreversible heat $\dot{Q}_{\text{irr,m}}$ (W m^{-3}) of active material m is caused by the energy loss associated with kinetics reactions and it is determined by the reaction overpotential:

$$\dot{Q}_{\text{irr,m}} = j_m^{\text{Li}} \eta_m \quad (5-2)$$

The ohmic heat generation is attributed to the transport resistance of charge species (ions or electrons), which appears to be the potential gradient in electrolyte or solid electrode particles:

$$\dot{Q}_{\text{ohm,ele}} = \sigma^{\text{eff}} \left(\frac{\partial \phi_s}{\partial x} \right)^2 \quad (5-3)$$

$$\dot{Q}_{\text{ohm,ion}} = \kappa^{\text{eff}} \left(\frac{\partial \phi_e}{\partial x} \right)^2 + \kappa_D^{\text{eff}} \frac{\partial \ln C_e}{\partial x} \frac{\partial \phi_e}{\partial x} \quad (5-4)$$

where $\dot{Q}_{\text{ohm,ele}} / \dot{Q}_{\text{ohm,ion}}$ (W m^{-3}) represents ohmic heat sources due to electron/ion transport.

The reversible heat sources $\dot{Q}_{\text{rev,m}}$ (W m^{-3}) of material m due to the reaction entropic change is expressed as

$$\dot{Q}_{\text{rev,m}} = j_m^{\text{Li}} T \frac{\partial E_{\text{eq,m}}}{\partial T} \quad (5-5)$$

Summing up these three heat sources gives rise to the total heat generation source

\dot{Q}_{gen}

$$\dot{Q}_{\text{gen}} = \sum_{m=\text{Gr,Si}} (\dot{Q}_{\text{irr,m}} + \dot{Q}_{\text{rev,m}}) + \dot{Q}_{\text{ohm,ele}} + \dot{Q}_{\text{ohm,ion}} \quad (5-6)$$

The thermal boundaries are listed as follows

$$-\lambda_{\text{WE}} \frac{\partial T}{\partial x} \Big|_{x=0} = h(T_{\text{amb}} - T(x=0)) \quad (5-7)$$

$$-\lambda_{\text{SEP}} \frac{\partial T}{\partial x} \Big|_{x=L_{\text{SEP/CE}}} = h(T(x=L_{\text{SEP/CE}}) - T_{\text{amb}}) \quad (5-8)$$

where h ($\text{W m}^{-2} \text{K}^{-1}$) is the heat transfer coefficient at the surface of the cell.

5.2.2. Temperature dependent properties

Temperature in turn can affect the equilibrium potential and entropy coefficient.

The equilibrium potential or OCP of each active material is modified as

$$E_{\text{eq,m}} = E_{\text{eq,m}}^{\text{ref}} + (T - T^{\text{ref}}) \frac{\partial E_{\text{eq,m}}}{\partial T} \Big|_{T^{\text{ref}}} \quad (5-9)$$

where $E_{\text{eq},m}^{\text{ref}}$ (V) is the OCP of material m at the reference temperature which are shown in Figure 4-2. The thermodynamic entropic coefficient of Gr with respect to θ_{Gr} during (de)lithiation, $\frac{\partial E_{\text{eq},\text{Gr}}}{\partial T}$ (V K⁻¹), is displayed in Figure A1-1 [74] and implemented as lookup tables in the model.

The reversible heat flow of Si anode was measured by Arnot et al. [75] and Lisa et al. [133], and it was demonstrated to be different during lithiation and delithiation.

The open circuit entropic coefficient of Si, denoted as $\frac{\partial E_{\text{eq},\text{Si}}}{\partial T}$ (V K⁻¹), is a function of SOC shown in Figure A1-2 and implemented as lookup tables in the model.

Temperature can also affect the transport properties and kinetic reaction rates. The temperature dependent effective electrolyte diffusivity D_e^{eff} (m² s⁻¹) is [21]

$$D_e^{\text{eff}} = \varepsilon^{\text{brugg}} \times 10^{-4} \times 10^{-4.43 - \frac{54}{T - 229 - 5 \times 10^{-3} C_c} - 0.22 \times 10^{-3} C_c} \quad (5-10)$$

The effective solid-phase diffusion coefficient $D_{s,m}^{\text{eff}}$ (m² s⁻¹) relies on temperature in an Arrhenius form

$$D_{s,m}^{\text{eff}} = D_{s,m} e^{-\frac{E_a^{D_{s,m}}}{R} \left(\frac{1}{T} - \frac{1}{T^{\text{ref}}} \right)} \quad (5-11)$$

where $E_a^{D_{s,m}}$ (J mol⁻¹) means the solid-phase diffusion activation energy of material m.

The effective reaction rate constant $k_{\text{react},m}$ (m^{2.5} mol^{-0.5} s⁻¹) is expressed as

$$k_{\text{react},m}^{\text{eff}} = k_{\text{react},m} e^{-\frac{E_a^{k_{\text{react},m}}}{R} \left(\frac{1}{T} - \frac{1}{T^{\text{ref}}} \right)} \quad (5-12)$$

where $E_a^{k_{\text{react},m}}$ (J mol⁻¹) refers to the reaction constant activation energy of material m.

The time derivative term of the composite electrode is expressed as the weighted average of the term for each active material

$$\rho_{\text{WE}} C_{p,\text{WE}} \varepsilon_s = \sum_m \left(\rho_m C_{p,m} \varepsilon_{s,m} \right) \quad (5-13)$$

The effective thermal conductivity of the composite electrode can be expressed as

$$\lambda^{\text{eff}} = \sum_m (\lambda_m \varepsilon_m^{\text{brugg}}) \quad (5-14)$$

where λ_m ($\text{W m}^{-1} \text{K}^{-1}$) is the thermal conductivity for each material.

5.2.3. Numerical procedures and model parameters

The same finite volume method as that in chapter 4 is used to discretize the differential equation system, and the computation was repeated until convergence was achieved for all the field variables. The parameter values used for base case simulations are summarized in Table 5-1.

Table 5-1 Parameter values of thermal properties.

Parameter	Value	Comment/reference
λ_{Gr} (W mK^{-1})	1.7	Ref. [94]
λ_{Si} (W mK^{-1})	2	Ref. [134]
$C_{\text{p,Gr}}$ (kJ kg^{-1})	700	Ref. [94]
$C_{\text{p,Si}}$ (kJ kg^{-1})	843	Ref. [135]
$E_a^{k_{\text{react,Gr}}}$ (J mol^{-1})	3600	Ref. [94]
$E_a^{k_{\text{react,Si}}}$ (J mol^{-1})	3600	Estimated
$E_a^{D_{\text{s,Gr}}}$ (J mol^{-1})	5000	Ref. [94]
$E_a^{D_{\text{s,Si}}}$ (J mol^{-1})	41431	Ref. [136]
T^{ref} (K)	298.15	-

5.3. Results and discussion

5.3.1. Temperature variation and contribution of different heat sources

Figure 5-1(a) and (c) show the temperature variation and contribution of heat sources associated with Gr and Si during delithiation of an electrode with $r_{\text{Si/Gr}} = 0.2$ at a 2C condition. The thermal characteristics of the Si/Gr composite electrode during the delithiation process can be divided into two stages. In the initial stage ($t < 500\text{s}$), graphite produces most of the heat compared to Si (shown in Figure 5-1(c)), while in the remaining stage, silicon is the major contributor to the heat generation. This is

mainly because during the delithiation process, graphite has a higher priority than Si to release lithium-ions at high state of charge (SOC). The observed phenomenon is in agreement with both the electrochemical competition process between Si and Gr described in Chapter 4, and with experimental results reported by Yao et al. [65], who concluded that the preferential delithiation occurs in Gr during the initial stage of the reaction when the electrode voltage (E) is lower than 0.23V.

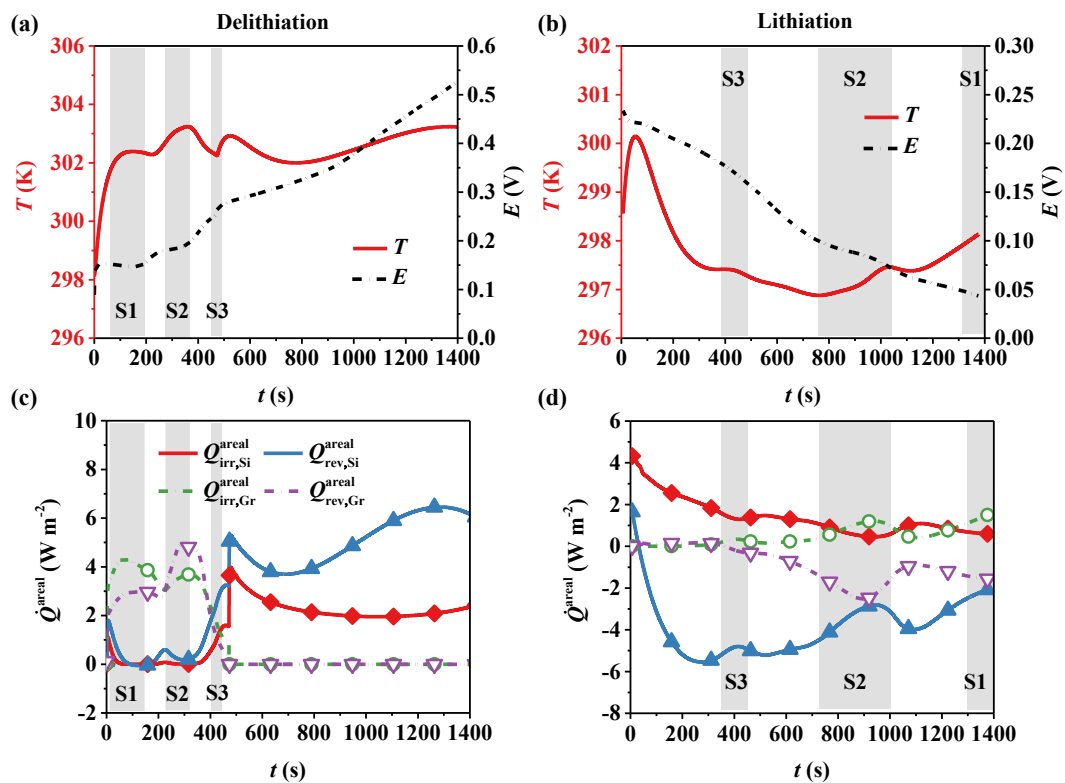


Figure 5-1 Temperature variation and electrode potential during (a) delithiation and (b)lithiation for an electrode with $r_{\text{Si/Gr}} = 0.2$ at a galvanostatic 2C delithiation condition, and $h = 1 \text{ W m}^{-1} \text{ K}^{-1}$. The heat contribution attributed to active materials is shown during (c) delithiation and (d) lithiation. Label S1 to S3 indicate the three phase transition processes of Gr.

Figure 5-1(a) displays two distinct thermal peaks occurring at the phase transition stages S1 and S2, which result from the significant irreversible and reversible heat generation of Gr during these stages, as shown in Figure 5-1(c). The high irreversible

and reversible heat generations of Gr are determined by its high reaction rate, which reaches a maximum at these two stages (as demonstrated in Figure 4-7). The heat generation of Si is only significant at the capacity intervals between phase transitions of Gr, when Si becomes more electrochemically active. At S3, the reaction rate and heat generation peak of Gr are not prominent, and the temperature decreases to a minimum due to external heat dissipation until silicon gradually dominates the reaction, leading to the appearance of a third peak in the temperature curve.

Figure 5-1(b) displays the temperature evolution over time during lithiation, which shows a distinct trend. Initially, the reaction of Si dominates and the composite electrode experiences a temperature increase due to the reversible and irreversible heat generation of Si. However, after the first thermal peak, there is a significant drop in temperature. Apart from the heat dissipation at the boundary, the reversible heat of Si and Gr becomes negative, as indicated in Figure 5-1(d), outweighing the ohmic and irreversible heat and resulting in a heat sink phenomenon. Three heat rejection peaks can be observed in the temperature curve of composite electrodes during lithiation, which may be attributed to the higher reaction rate of Si at these stages. The temperature profile closely resembles the heat contribution of Si (as seen in Figure 5-1(d)), while the impact of Gr's heat generation on temperature variation is not significant. This is because the reversible and irreversible heat of Gr are of similar magnitude and opposite sign, nearly canceling each other out. The heat generation and rejection peaks of Gr are visible at S1, S2, and S3 (as seen in Figure 5-1(d)), where Gr exhibits a high reaction rate.

As the thermal peaks signify the phase transitions of electrode materials, the degradation of active materials can thus be quantified by tracking the evolution of these

thermal peaks. These simulated results therefore have implications in guiding for such thermal diagnostic experiments.

5.3.2. Effects of Si content on thermal behaviors

Figure 5-2(a) shows the temperature change of electrodes with different silicon fractions during lithiation process. An initial temperature increase of the composite electrode is seen due to the positive heat sources, and a first thermal peak is seen in Figure 5-2(a). Three subsequent thermal peaks can be found for composite electrodes, which are caused by the competition of reaction rate of the two active materials. These thermal peaks increase in magnitude and shift to the high SOC side as the Si content increases. This is because the lithiation of Gr delays with higher Si additives.

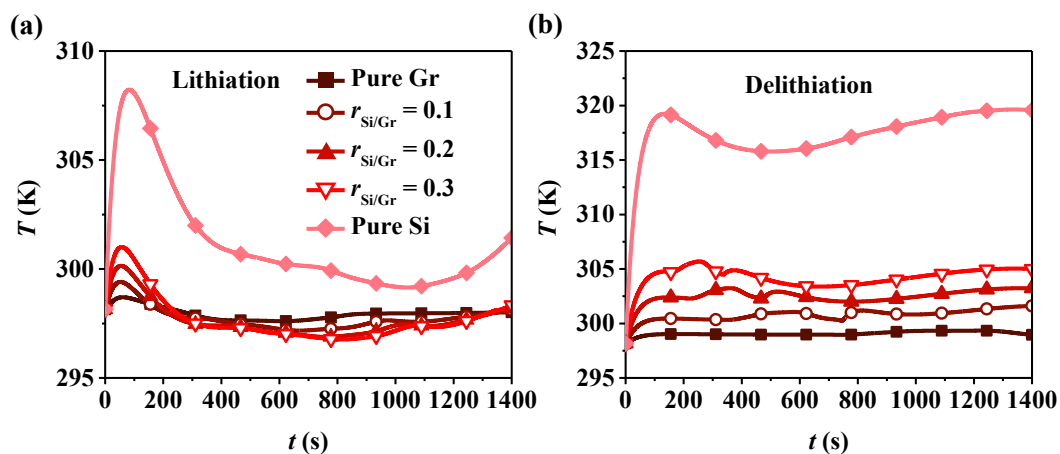


Figure 5-2 Temperature variation of electrodes with different Si content during (a) lithiation (b) delithiation at a galvanostatic 2C condition, and $h = 1 \text{ W m}^{-1} \text{ K}^{-1}$.

In contrast, the temperature evolution with time during delithiation is different, displayed by Figure 5-2(b). For delithiation, temperature variations of composite electrodes with different Si content show a similar trend, increasing first followed by a drop, and concave profiles are observed during latter stage of the reaction, which present the same shape of that for pure Si. This implies that Si dominates the lower end of SOC during delithiation process for all these electrodes, supported by our previous results in chapter 4. The temperature rises more significantly for composite electrodes

with higher Si fractions. The reason is that the composite electrode with a higher Si fraction can provide more capacity, which leads to a higher current density at the same C-rate. As a result, more heat production and higher temperature increment will be seen in the composite electrode. Besides, as Si content increases, the thermal peaks shift to the left-hand side in Figure 5-2(b), namely the higher end of SOC during delithiation. This is mainly because that a higher $r_{\text{Si/Gr}}$ means a lower fraction of Gr, and hence its phase transition processes during delithiation will last for a shorter time.

Comparing Figure 5-2(a) and (b), it is marked that the thermal behaviors during lithiation and delithiation are irreversible. This irreversibility derives from the asymmetric reaction kinetic behaviors of composite electrodes due to voltage hysteresis of Si. Another cause is the asymmetric entropic change of Si during lithiation and delithiation. In summary, Figures 5.2(a) and 5.2(b) provide valuable insights into the temperature changes of composite electrodes with different compositions during the lithiation and delithiation processes.

5.3.3. Thermal temporal-spatial inhomogeneity during delithiation

The thermal behaviors strongly depend on the reaction rates of different electrode materials. The electrochemical reaction of Gr converges on the beginning stage of delithiation followed by the reaction of Si, which is consistent with the results shown in the previous sections. The spatial distribution of current density of Gr is shown in Figure 5-3(a). Gr shows noticeable spatial inhomogeneity of the reaction activity during delithiation, while Si presents little difference in its reaction activity across the composite electrode, shown in Figure 5-3(b). The reaction rate of Gr is higher at the separator side ($x = L_{\text{SEP/CE}}$) than the current collector side ($x = 0$) when Gr undergoes two-phase transitions. However, the phenomenon changes within the single-phase stages of Gr (between S1, S2 and S3), and local reaction rate of Gr becomes larger at

the current collector side ($x = 0$). Similar heterogeneity of the reaction activity was observed and analyzed by Chen et al., who concluded that this “reaction distribution wave” was generated when going through the voltage plateaus (i.e. stages S1, S2 and S3) of Gr, and it is attributed to both thermodynamics and kinetics of the reaction [137].

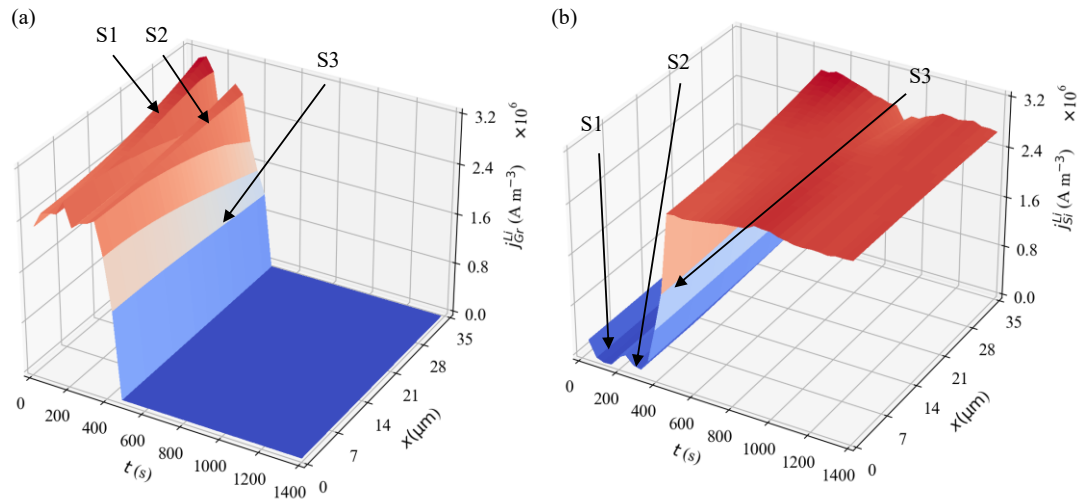


Figure 5-3 Current density of (a) Gr and (b) Si for electrode with $r_{\text{Si/Gr}} = 0.2$ at a galvanostatic 2C delithiation condition. Label S1 to S3 indicate the three phase transition processes of Gr.

Figure 5-4 shows that the ohmic heat distribution across the composite electrode remains unchanged during the whole delithiation process. The ohmic heat generation in the working electrode declines from the separator side to the current collector side. The reason is that a major part of the ohmic heat originates from the ionic migration, which is determined by the ionic current density. The ionic current density equals zero at the current collector side ($x = 0$) as the current collector is ionic insulate, while it reaches its maximum value at the separator side ($x = L_{\text{SEP/CE}}$) where the ionic current density equals the applied current density.

In contrast, uniform distribution of ohmic heat generation across the separator is seen at each time step because the ionic current density and conductivity are similar in the separator, shown in Figure 5-4(b). However, the ohmic heat generation in the

separator fluctuates with time during the delithiation process, and it reaches peaks at phase transformation stages of Gr (S1-S3). The phase transition processes of Gr can lead to significant fluctuation of electrolyte concentration [137], and hence the concentration dependent conductivity is expected to change greatly within the corresponding time spans. Consequently, the variation of conductivity will cause the large fluctuation of ohmic heat with time.

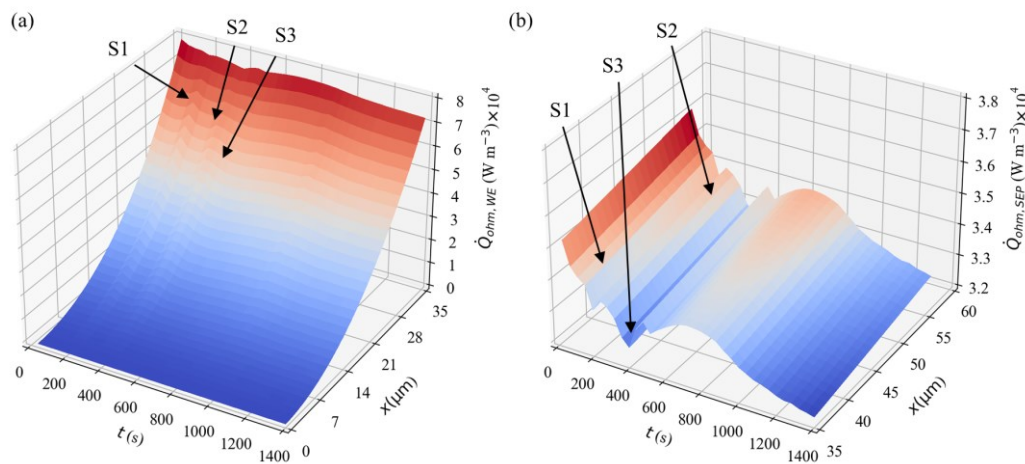


Figure 5-4 Ohmic heat generation of (a) working electrode and (b) separator for composite electrode with $r_{\text{Si/Gr}} = 0.2$ at a galvanostatic 2C delithiation condition. Label S1 to S3 indicate the three phase transition processes of Gr.

The spatial and temporal distributions of reversible and irreversible heat sources produced by different electrode materials (i.e. Gr ad Si) are shown in Figure 5-5. In essence, the spatial inhomogeneity in reversible heat generation is the superimposed

effect of both $\frac{\partial E_{\text{eq,m}}}{\partial T}$ and current density distribution in space. Figure 5-5(a) shows that

only slight inhomogeneity in reversible heat generation occurs during the phase transformation processes of Gr. The reversible heat generation of Si also shows a uniform spatial distribution in Figure 5-5(b) due to the homogeneous spatial distribution of the current density of Si displayed in Figure 5-3 (b).

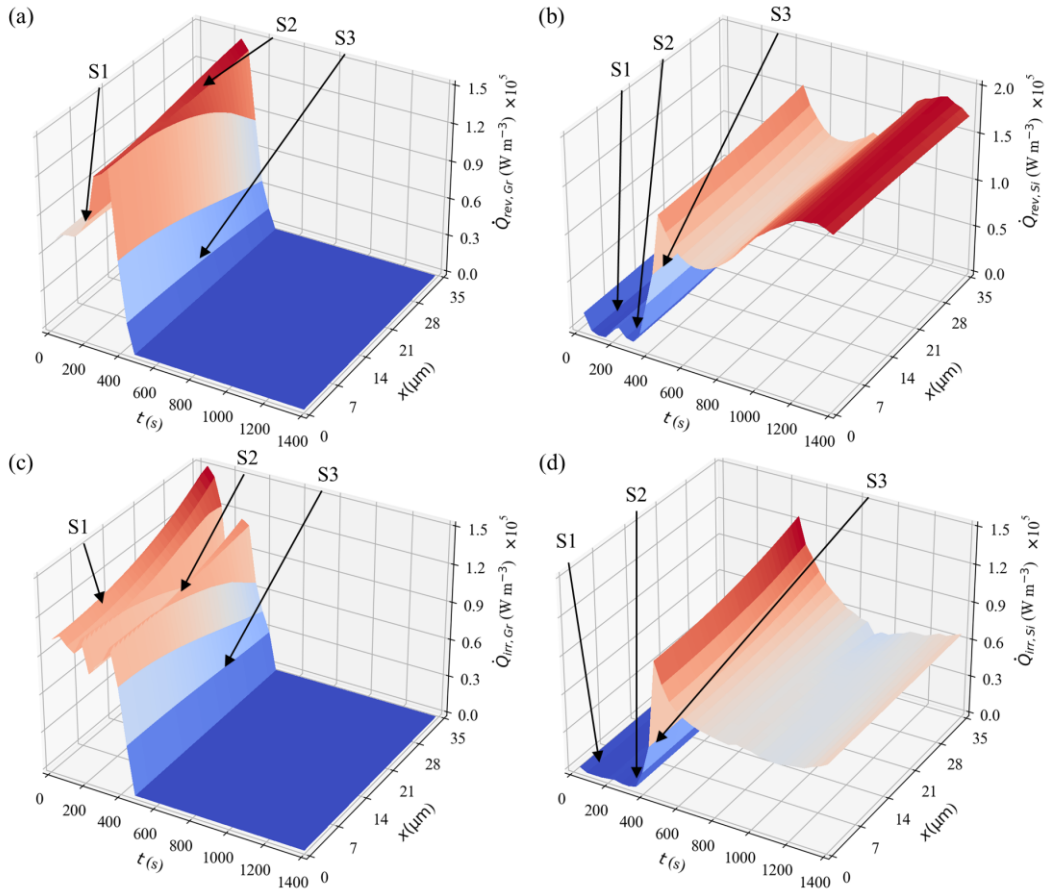


Figure 5-5 Reversible heat generation of (a) Gr. and (b) Si, and irreversible heat generation of (c) Gr and (d) Si for electrode with $r_{Si/Gr} = 0.2$ at a galvanostatic 2C delithiation condition. Label S1 to S3 indicate the three phase transition processes of Gr.

The irreversible heat generation is determined by both the current density and overpotential. By comparing Figure 5-3(a) and Figure 5-5(c), the irreversible heat profile of Gr has the same features as the partial current density of it. In comparison, the irreversible heat generation profile of Si only experiences minor fluctuation in space due to its uniform current density distribution shown in Figure 5-3(b)

5.3.4. Thermal temporal-spatial inhomogeneity during lithiation

The current densities of two active materials during lithiation are illustrated in Figure 5-6. The temporal variation of the current density for Gr displays three distinct peaks, as depicted in Figure 5-1(b) and (d) during lithiation. These peaks correspond

to the initial high lithiation rate of Si and the staging processes S3 and S2. In terms of spatial distribution, Gr exhibits a slightly higher current density on the separator side than on the current collector side during its phase transition stages (S1-S3). However, the overall current density distribution for Gr is more uniform across the electrode during lithiation compared to delithiation. This is due to the simultaneous lithiation of Gr and Si, leading to a lower partial lithiation current density for Gr compared to delithiation. The peak lithiation current density of Gr is $1.6 \times 10^6 \text{ A m}^{-3}$, as shown in Figure 5-6(a), which is half of that observed during delithiation in Figure 5-3(a). Meanwhile, the current density of Si bottoms out during the staging processes of Gr in Figure 5-6(b). The spatial current density distribution of Si is uniform.

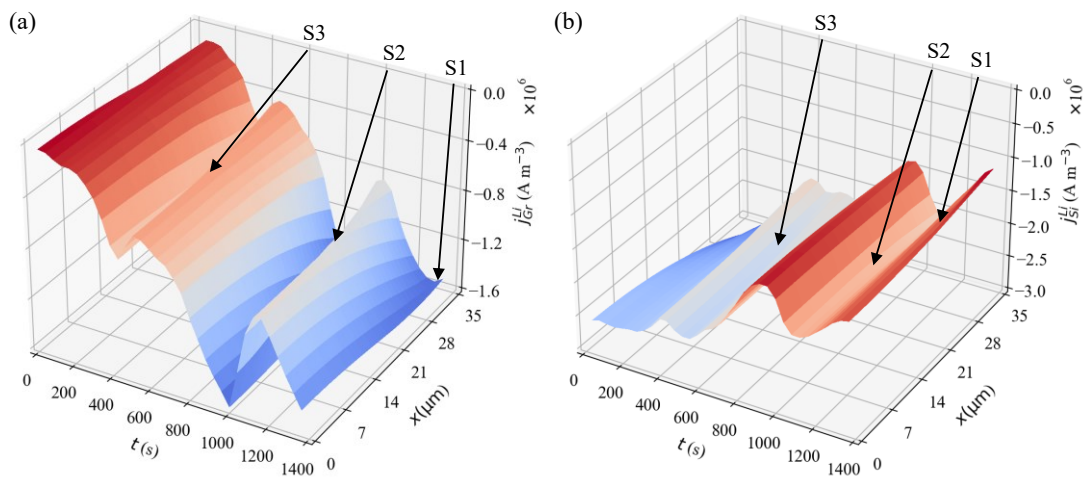


Figure 5-6 Current density of (a) Gr and (b) Si for electrode with $r_{Si/Gr} = 0.2$ at a galvanostatic 2C lithiation condition. Label S1 to S3 indicate the three phase transition processes of Gr.

In Figure 5-7(a), the spatial distribution of the ohmic heat generation in the composite electrode during lithiation is very similar to that during delithiation shown in Figure 5-4(a) for the reason that the ionic current density reduces from the separator side to the current collector side. In Figure 5-7(b), the ohmic heat generation in the separator shows three valleys at the phase transitions of Gr during lithiation. It has an

opposite spatial distribution in lithiation compared to that in delithiation process with heat generation higher at the working electrode side ($x = 35 \mu\text{m}$) than the separator side ($x = 57 \mu\text{m}$). The reason is that when the Li cations flow in an opposite direction in the cell, the ionic ohmic heat which depends on the electrolyte concentration is reversed.

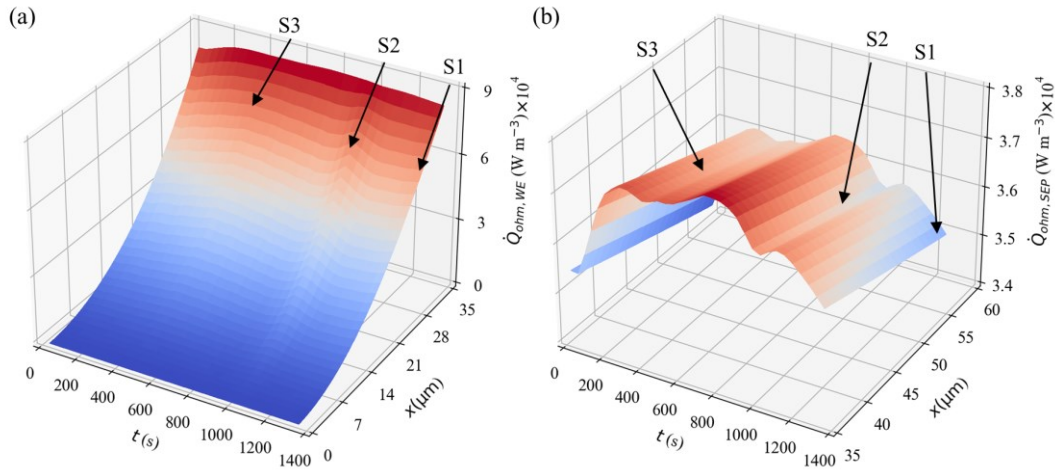


Figure 5-7 Ohmic heat generation of (a) separator and (b) composite electrode for electrode with $r_{\text{Si/Gr}} = 0.2$ at a galvanostatic 2C lithiation condition. Label S1 to S3 indicate the three phase transition processes of Gr.

During lithiation, both the reversible and irreversible heat generations of Gr exhibit peak values in their corresponding phase transition regions S1-S3, as shown in Figure 5-8(a) and (c). It should be noted that the reversible heat is negative during lithiation, and its peak is directed towards the negative axis. In terms of spatial distribution, the reversible and irreversible heats of Gr are slightly higher on the separator side than on the current collector side, which is similar to the distribution pattern of the reaction rate of Gr. In contrast, the reversible and irreversible heat of Si both appear as minimum values at the phase transition location of Gr, and their spatial distribution is relatively uniform.

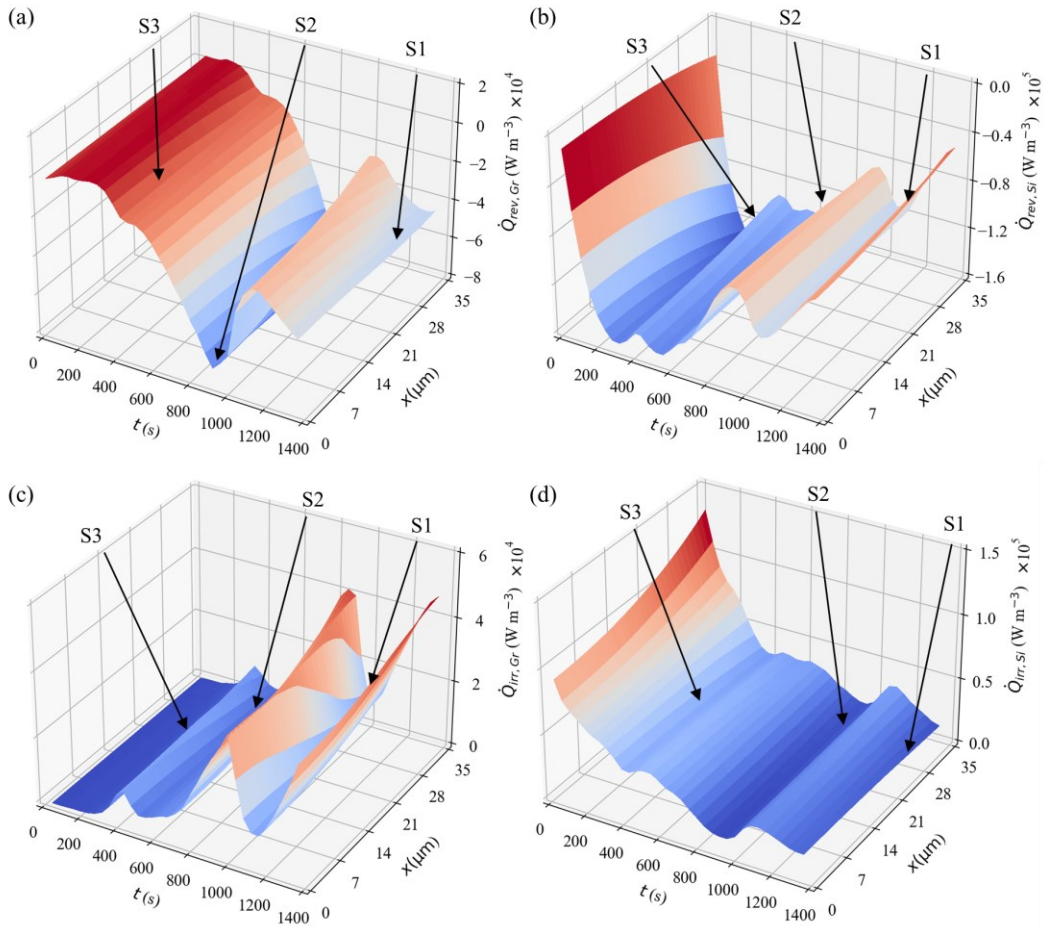


Figure 5-8 (a) Reversible and (b) irreversible heat generation of Gr. (c) reversible and (d) irreversible heat generation of Si for electrode with $r_{Si/Gr} = 0.2$ at a galvanostatic 2C lithiation condition. Label S1 to S3 indicate the three phase transition processes of Gr.

5.3.5. Effects of C rate on the thermal behaviors

Figure 5-9 compares the temperature profiles of composite electrodes at different C-rates. During both lithiation and delithiation, the temperature of the entire electrode increases, and the temperature fluctuations become more noticeable as the C-rate increases. However, increasing the C-rate does not cause significant changes in the shape of the temperature curve, nor does it cause any significant change in the position of the temperature peak. These findings suggest that C-rate has a large impact on the thermal behavior of the electrode but does not affect the characteristic features of the temperature curve.

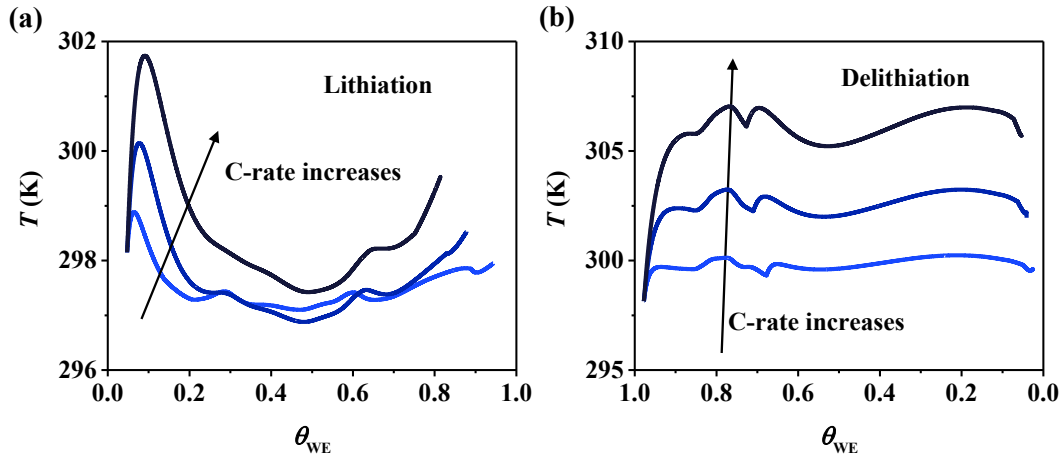


Figure 5-9 Temperature variation for the electrode with $r_{\text{Si/Gr}} = 0.2$ with a rising C-rate from 1C, 2C to 3C during (a) lithiation and (b) delithiation.

5.3.6. Effects of heat transfer coefficient

Figure 5-10(a) and (b) depict the temperature changes of the Si/Gr composite electrode with $r_{\text{Si/Gr}} = 0.1$ under various external heat transfer conditions during lithiation and delithiation. As the heat transfer coefficient decreases during lithiation, the temperature of the electrode exhibits more significant fluctuations. Specifically, under adiabatic conditions ($h = 0 \text{ W m}^{-1} \text{ K}^{-1}$), the temperature can rise by up to 6K. During delithiation, a decrease in the heat transfer coefficient h can result in difficulty dissipating heat inside the electrode, leading to an increase in electrode temperature. In extreme adiabatic conditions, the temperature of the Si/Gr electrode during lithium removal can surge to as high as 400K, which is significantly beyond the normal operating temperature range of lithium-ion batteries. In practical applications, subjecting LIBs to such high temperature significantly increases the risk of thermal abuse. The components (such as SEI) of LIBs become unstable and a series of exothermic reactions may happen [138]. Furthermore, the separator will melt at temperature exceeding about 140°C , resulting in a short circuit within the cell and potentially causing a fire [139]. This predicted high temperature implies the importance of employing an effective cooling system for Si/Gr composite electrode. It can also be

concluded that the heat release of the Si/Gr composite electrode is more prominent during delithiation than during lithiation. This can be attributed to the fact that the reversible heat during lithiation reactions for both Si and Gr is mostly endothermic.

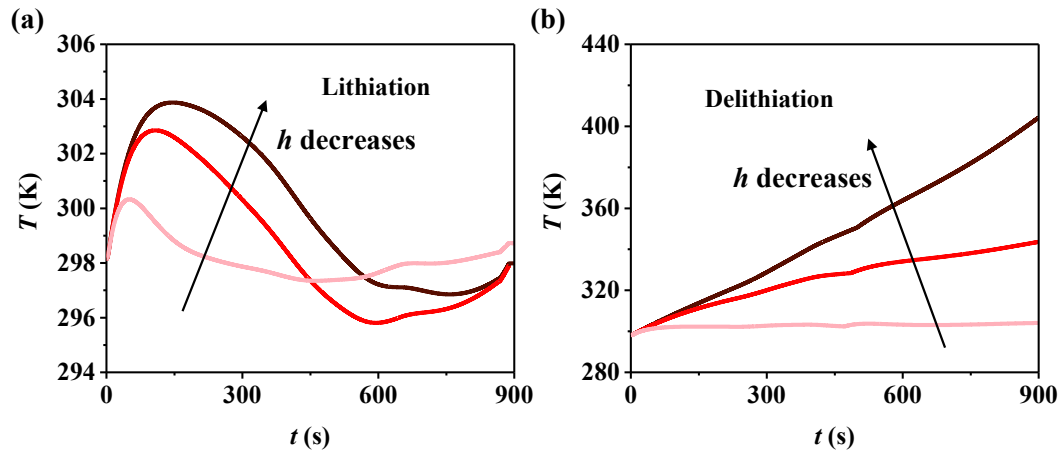


Figure 5-10 Temperature variation of the electrode with $r_{Si/Gr} = 0.1$ during a (a) lithiation and (b) delithiation galvanostatic 3C condition. The ambient temperature remains a constant 298.15K with different external heat transfer rate ($h = 0, 0.1$ and $1 \text{ W m}^{-1} \text{ K}^{-1}$).

5.4. Interim conclusion

A thermally coupled electrochemical model for Si/Gr composite electrodes is developed based on a multi-material model framework. This model can separate different heat contributions of each active material by adopting their respective thermal properties and reaction rates. The temperature variation and different heat sources are analyzed for electrodes with different Si fractions. Results show that at the same C-rate, an electrode with a higher Si content sees a higher temperature rise. Observable thermal peaks can be identified during both lithiation and delithiation processes, corresponding to the phase transition processes of Gr. These thermal peaks can be potentially used to detect the ageing of Si-based batteries in service. The contribution of different heat sources is further analyzed. The heat generation of Gr converges on the beginning stage of delithiation, followed by huge heat generation from Si. In contrast, the two active

materials are lithiated simultaneously, and Gr plays a dominant role in the thermal behaviors during its phase transition processes. Both the temporal and spatial variation of heat sources are analyzed in this study. Obvious spatial fluctuations, attributed to heterogeneous current density field, is observed between the phase transition processes of Gr. The effect of external heat transfer rate on electrodes is also investigated, and a higher convective heat transfer coefficient leads to more obvious thermal peaks which signifies the phase transitions of Gr. This distinguishable thermal feature can be used for electrode diagnosis in future work. Additionally, the maximum temperature that a single battery can reach under a given condition can be predicted by simulating the insulation condition, offering important information to guide for the battery safety.

Chapter 6. Conclusions and future works

6.1. Conclusions

The aim of this work is to develop fundamental modelling tools towards silicon-based lithium-ion batteries. The literature review reveals that the existing battery model framework lacks capability to describe the unique electrochemical behaviors of Si, especially its voltage hysteresis. Secondly, commercial silicon-based batteries normally use Si/Gr composite electrodes instead of pure Si to mitigate their degradation by taking advantage of the high capacity of Si and good structural integrity of Gr. As silicon has distinct behaviors from Gr, the analysis and design of such composite electrodes require an improved understanding of the individual effects of each active material on the overall performance. Therefore, building a multi-material model framework considering respective effect of Si and Gr is important.

To this end, a zero-dimensional mechanistic voltage model is developed for silicon anodes in LIBs. The model is able to capture key electrochemical phenomena during cycling of silicon electrodes for the first time, including the sloping voltage curve with voltage hysteresis at small lithiation depths and the shift to a single distinct voltage plateau on discharge from the initial sloping curve upon deep lithiation. Comparisons show a good agreement between the model and experimental results. The processes of phase transformations, crystallization and amorphization underlying the electrode behaviors are resolved in the model. The model correlates the electrochemical behaviors of Si with the underlying reaction processes in a quantitative manner. Results show that the voltage hysteresis is path-dependent and the asymmetric hysteresis originates from asymmetric reaction pathways. The model is then used to study the effects of crystallization rate and surface energy barriers. The crystallization rate constant k_{cryst} can affect the shape of the crystalline growth curve, and a lower k_{cryst} will

delay the appearance of the crystalline phase. The extra potential increase E^* induced by surface energy barriers between crystalline and amorphous phases is shown to be the underlying cause of the elevated voltage plateau for silicon electrodes. Even though there are two electrochemical reactions, the differential analysis can only detect one visible voltage peak when E^* is large enough. The surface energy barrier also explains qualitatively why smaller silicon particles present a sloping voltage curve even charged to 0 V. The model is a necessary tool for future design and development of high-energy-density, longer-life silicon-based LIBs.

Furthermore, a multi-material model is developed for Si/Gr blended electrodes considering the voltage hysteresis of Si. The model takes into account different properties and electrochemical reactions of the different active materials and can provide detailed descriptions of the contributions of the individual active materials during the cycling of electrodes. The modelling results shows good agreement with both electrochemical measurements and in-operando EDXRD profiling. Based on the model, the charge/discharge characteristics of Si/Gr electrodes with different Si/Gr ratios are studied. Results show that Si additives can significantly enhance the specific capacity of Si/Gr electrodes, and the electrochemical features of Gr become less obvious with increasing Si content. Si can also introduce voltage hysteresis for Si/Gr electrodes and consequently a “plateau shift” during delithiation of blended electrodes. The contributions of the individual active materials to the capacity of blended electrodes are analyzed. It is found that lithiation starts with Si and the lithiation reaction rate of Gr is comparable to that of Si at high SOC levels of Si/Gr electrodes. Delithiation occurs preferentially from Gr at high SOC levels, whereas Si dominates the electrode delithiation at lower SOC levels. Si/Gr ratio can affect the active SOC regions for the individual materials: increasing material content will increase the active

SOC range for that material. A dimensionless competing factor is introduced to quantify the relative contribution of each active material, which is demonstrated to be an effective parameter for identifying the active regions of the individual materials. Micro cycling studies suggest that the competing factor can be used to design cycling strategies for mitigating degradation of Si/Gr electrodes. The multi-material model can be readily implemented into full-cell models and coupled with other physics to guide further development of lithium-ion batteries with Si-based electrodes.

A thermally coupled electrochemical model for Si/Gr composite electrodes is then developed based on the multi-material model framework. This model can separate different heat contributions of each active material by adopting their respective thermal properties and reaction rates. It is found that the thermal characteristics of Si/Gr composite electrodes are highly correlated to the reaction competition between Si and Gr, and the voltage hysteresis of Si results in the irreversible thermal behaviors between lithiation and delithiation processes. Observable thermal peaks can be identified during both lithiation and delithiation processes, corresponding to the phase transition processes of Gr. The temperature variation and different heat sources are analyzed for electrodes with different Si fractions. Results show that at the same C-rate, an electrode with a higher Si content sees a higher temperature rise. Meanwhile, the thermal peaks shift to the higher end of SOC (where Gr is more electrochemically active) and undermines in their magnitude with higher Si content. These thermal peaks can be potentially used to detect the ageing of Si-based batteries in service. The contribution of different heat sources is also analyzed. The heat generation of Gr converges on the beginning stage of delithiation, followed by huge heat generation from Si. In contrast, the two active materials are lithiated simultaneously, and Gr plays a dominant role in the thermal behaviors during its phase transition processes. Both the temporal and

spatial variation of heat sources are analyzed in this study. During both lithiation and delithiation processes, the heat generation of Gr reaches its peak during its phase transition period, which is consistent with the pattern of its current density. Moreover, the phase transition of Gr is evidenced to be the reason for the heterogeneous spatial distribution of different heat generations. The effects of external heat transfer rate on electrodes are also investigated, and a higher convective heat transfer coefficient leads to more obvious thermal peaks which signifies the phase transitions of Gr. This distinguishable thermal feature can be used for electrode diagnosis in future work. Additionally, the maximum temperature that a single battery can reach under a given condition can be predicted by simulating the insulation condition, offering important information to guide for the battery safety.

6.2. Future works

The modelling tools developed in this research provide insights into the unique voltage hysteresis behavior of silicon-based electrodes, and how this phenomenon leads to the asymmetric reaction competition processes and thermal behaviors of a Si/Gr composite electrode. Compared to previous models, these new modelling tools have the advantage of allowing for the design of crucial parameters of composite electrodes, such as silicon mass fraction. Furthermore, there is a strong need and motivation to broaden the application of modelling tools for silicon-based electrodes in lithium-ion batteries and extend these tools to cover the degradation of these electrodes.

Given the limited timeframe of a PhD, there were a few remaining works that should be of interest to continue:

- The zero-dimensional multi-phase voltage hysteresis model can be further coupled into the core-shell model of electrode particles, which allows dividing the electrode particles into Li-rich and Li-poor regions along the radial direction. The disparities

in volume expansion rates between the Li-rich and Li-poor phases will result in significant internal stresses at the phase boundaries, leading to particle fracture and consequently, a reduction in the cycle life of silicon-based electrodes. By employing this model, it becomes possible to optimize the design of silicon-based electrodes, focusing on particle-level morphologies and refining cycling protocols for enhanced performance.

- The voltage hysteresis model with multi-step reactions can also be integrated into high-dimensional continuity battery models. This approach can provide further insights into other nonlinear behaviors of silicon-based batteries, such as the experimentally observed nonlinear diffusivity and irreversible volume change during (de)lithiation. By incorporating this model into higher-dimensional models, it also becomes feasible to better understand and interpret the inhomogeneous behaviors of silicon-based batteries, including localized nonuniform volume variations, SEI growth rates and cracking. The resulting insights may lead to improvements in the design and optimization of silicon-based batteries across diverse applications.
- The lack of experimental data on thermal measurements of Si/Gr composite electrodes needs to be addressed by carrying out experiments on Si/Gr composite electrode half-cells with Li metal as the counter electrode. The experimental data will be used to re-parametrize and validate the thermally coupled Si/Gr composite electrode model, providing a more accurate understanding of its thermal behavior, and improving the predictive capability of the simulation model.
 - To combine the thermally coupled model of Si/Gr composite electrodes with differential thermal voltammetry (DTV) technique to simulate and diagnose batteries under various cell conditions.

Reference

- [1] Olof Ramström, Scientific Background on the Nobel Prize in Chemistry 2019 LITHIUM-ION BATTERIES, R. Swedish Acad. Sci. 50005 (2019) 0–13.
- [2] Y. Merla, Development of new on-board battery diagnosis/prognosis tools for extending lifetime and mitigating failure, Ph.D. Thesis, Imperial College London, London, UK, 2019.
- [3] Y. Ding, Z.P. Cano, A. Yu, J. Lu, Z. Chen, Automotive Li-Ion Batteries: Current Status and Future Perspectives, *Electrochem. Energy Rev.* 2 (2019) 1–28.
- [4] L. Zhang, C. Zhu, S. Yu, D. Ge, H. Zhou, Status and challenges facing representative anode materials for rechargeable lithium batteries, *J. Energy Chem.* 66 (2022) 260–294.
- [5] V.H. Nguyen, Y.H. Kim, Recent advances in cathode and anode materials for lithium ion batteries, *Appl. Chem. Eng.* 29 (2018) 635–644.
- [6] G. Xu, X. Shangguan, S. Dong, X. Zhou, G. Cui, Formulation of Blended-Lithium-Salt Electrolytes for Lithium Batteries, *Angew. Chemie - Int. Ed.* 59 (2020) 3400–3415.
- [7] X. Zeng, M. Li, D. Abd El-Hady, W. Alshitari, A.S. Al-Bogami, J. Lu, K. Amine, Commercialization of Lithium Battery Technologies for Electric Vehicles, *Adv. Energy Mater.* 9 (2019).
- [8] V. Agubra, J. Fergus, Lithium ion battery anode aging mechanisms, *Materials (Basel)*. 6 (2013) 1310–1325.
- [9] J.Y. Kim, D.Y. Lim, Surface-modified membrane as a separator for lithium-ion polymer battery, *Energies*. 3 (2010) 866–885.

- [10] A. Etienne, N. Besnard, A. Bonnin, J. Adrien, T. Douillard, P. Tran-Van, L. Gautier, J.C. Badot, E. Maire, B. Lestriez, Multiscale morphological characterization of process induced heterogeneities in blended positive electrodes for lithium-ion batteries, *J. Mater. Sci.* 52 (2017) 3576–3596.
- [11] M.K. Nasir, R. Md Noor, M.A. Kalam, B.M. Masum, Reduction of fuel consumption and exhaust pollutant using intelligent transport systems, *Sci. World J.* 2014 (2014).
- [12] A. Awan, Batteries: An essential technology to electrify road transport, in: *Glob. EV Outlook 2020 Enter. Decad. Electr. Drive?*, International Energy Agency, 2020: pp. 185–219.
- [13] IEA, Net Zero by 2050: A Roadmap for the Global Energy Sector, *Int. Energy Agency.* (2021) 224. <https://www.iea.org/reports/net-zero-by-2050>.
- [14] I.E.A.G.E. V Outlook, International Energy Agency: Paris, Francia. (2017).
- [15] The Lifecycle Emissions of Electric Vehicles, Bloom. New Energy Financ. (2023). <https://about.bnef.com/blog/the-lifecycle-emissions-of-electric-vehicles/> (accessed March 3, 2023).
- [16] M. Ue, K. Sakaushi, K. Uosaki, Basic knowledge in battery research bridging the gap between academia and industry, *Mater. Horizons.* 7 (2020) 1937–1954.
- [17] Z. Lin, T. Liu, X. Ai, C. Liang, Aligning academia and industry for unified battery performance metrics, *Nat. Commun.* 9 (2018) 8–12.
- [18] M. Ue, K. Sakaushi, K. Uosaki, Basic knowledge in battery research bridging the gap between academia and industry, *Mater. Horizons.* 7 (2020) 1937–1954.
- [19] S. Zhang, K. Ueno, K. Dokko, M. Watanabe, Recent advances in electrolytes for lithium-sulfur batteries, *Adv. Energy Mater.* 5 (2015) 1500117.

- [20] Q. Wang, B. Liu, Y. Shen, J. Wu, Z. Zhao, C. Zhong, W. Hu, Confronting the Challenges in Lithium Anodes for Lithium Metal Batteries, *Adv. Sci.* 8 (2021) 1–25.
- [21] P. Li, G. Zhao, X. Zheng, X. Xu, C. Yao, W. Sun, S.X. Dou, Recent progress on silicon-based anode materials for practical lithium-ion battery applications, *Energy Storage Mater.* 15 (2018) 422–446.
- [22] N. Nitta, F. Wu, J.T. Lee, G. Yushin, Li-ion battery materials: Present and future, *Mater. Today.* 18 (2015) 252–264.
- [23] H. Zheng, H. Xiang, F. Jiang, Y. Liu, Y. Sun, X. Liang, Y. Feng, Y. Yu, Lithium difluorophosphate-based dual-salt low concentration electrolytes for lithium metal batteries, *Adv. Energy Mater.* 10 (2020) 2001440.
- [24] S. Liu, Y. Zhao, X. Li, J. Yu, J. Yan, B. Ding, Solid-state lithium metal batteries with extended cycling enabled by dynamic adaptive solid-state interfaces, *Adv. Mater.* 33 (2021) 2008084.
- [25] A. Fu, C. Wang, J. Peng, M. Su, F. Pei, J. Cui, X. Fang, J. Li, N. Zheng, Lithiophilic and antioxidative copper current collectors for highly stable lithium metal batteries, *Adv. Funct. Mater.* 31 (2021) 2009805.
- [26] D. Larcher, S. Beattie, M. Morcrette, K. Edström, J.C. Jumas, J.M. Tarascon, Recent findings and prospects in the field of pure metals as negative electrodes for Li-ion batteries, *J. Mater. Chem.* 17 (2007) 3759–3772.
- [27] M.N. Obrovac, V.L. Chevrier, Alloy negative electrodes for Li-ion batteries, *Chem. Rev.* 114 (2014) 11444–11502.
- [28] T. Placke, R. Kloepsch, S. Dühnen, M. Winter, Lithium ion, lithium metal, and alternative rechargeable battery technologies: the odyssey for high energy density, *J. Solid State Electrochem.* 21 (2017) 1939–1964.

- [29] M.T. McDowell, S.W. Lee, W.D. Nix, Y. Cui, 25th anniversary article: Understanding the lithiation of silicon and other alloying anodes for lithium-ion batteries, *Adv. Mater.* 25 (2013) 4966–4985.
- [30] H. Wu, Y. Cui, Designing nanostructured Si anodes for high energy lithium ion batteries, *Nano Today*. 7 (2012) 414–429.
- [31] Yiu, Nicholas. Jing, Linda. Yeh, Yen. He, Katherine. Zheng, Eric. “State of Batteries Report 2020.” *BatteryBits*, 16 January 2021. Web. (Accessed March 3, 2023).
- [32] F. Brosa Planella, W. Ai, A.M. Boyce, A. Ghosh, I. Korotkin, S. Sahu, V. Sulzer, R. Timms, T.G. Tranter, M. Zyskin, S.J. Cooper, J.S. Edge, J.M. Foster, M. Marinescu, B. Wu, G. Richardson, A continuum of physics-based lithium-ion battery models reviewed, *Prog. Energy*. 4 (2022) 042003.
- [33] C.Y. Wang, V. Srinivasan, Computational battery dynamics (CBD) - Electrochemical/thermal coupled modeling and multi-scale modeling, *J. Power Sources*. 110 (2002) 364–376.
- [34] T. Ohzuku, Formation of Lithium-Graphite Intercalation Compounds in Nonaqueous Electrolytes and Their Application as a Negative Electrode for a Lithium Ion (Shuttlecock) Cell, *J. Electrochem. Soc.* 140 (1993) 2490.
- [35] M.P. Mercer, C. Peng, C. Soares, H.E. Hoster, D. Kramer, Voltage hysteresis during lithiation/delithiation of graphite associated with meta-stable carbon stackings, *J. Mater. Chem. A*. 9 (2021) 492–504.
- [36] M. Klett, J.A. Gilbert, K.Z. Pupek, S.E. Trask, D.P. Abraham, Layered Oxide, Graphite and Silicon-Graphite Electrodes for Lithium-Ion Cells: Effect of Electrolyte Composition and Cycling Windows, *J. Electrochem. Soc.* 164 (2017) A6095–A6102.

- [37] P. Limthongkul, Y. Il Jang, N.J. Dudney, Y.M. Chiang, Electrochemically-driven solid-state amorphization in lithium-metal anodes, *J. Power Sources*. 119–121 (2003) 604–609.
- [38] H. Okamoto, The Li-Si (lithium-silicon) system, *Bull. Alloy Phase Diagrams*. 11 (1990) 306–312.
- [39] C.J. Wen, R.A. Huggins, Chemical diffusion in intermediate phases in the lithium-silicon system, *J. Solid State Chem.* 37 (1981) 271–278.
- [40] T.D. Hatchard, J.R. Dahn, In Situ XRD and Electrochemical Study of the Reaction of Lithium with Amorphous Silicon, *J. Electrochem. Soc.* 151 (2004) A838.
- [41] M.N. Obrovac, L. Christensen, Structural changes in silicon anodes during lithium insertion/extraction, *Electrochem. Solid-State Lett.* 7 (2004).
- [42] W.J. Zhang, Lithium insertion/extraction mechanism in alloy anodes for lithium-ion batteries, *J. Power Sources*. 196 (2011) 877–885.
- [43] J.W. Wang, Y. He, F. Fan, X.H. Liu, S. Xia, Y. Liu, C.T. Harris, H. Li, J.Y. Huang, S.X. Mao, T. Zhu, Two-phase electrochemical lithiation in amorphous silicon, *Nano Lett.* 13 (2013) 709–715.
- [44] X.H. Liu, J.W. Wang, S. Huang, F. Fan, X. Huang, Y. Liu, S. Krylyuk, J. Yoo, S.A. Dayeh, A. V. Davydov, S.X. Mao, S.T. Picraux, S. Zhang, J. Li, T. Zhu, J.Y. Huang, In situ atomic-scale imaging of electrochemical lithiation in silicon, *Nat. Nanotechnol.* 7 (2012) 749–756.
- [45] J. Li, J.R. Dahn, An In Situ X-Ray Diffraction Study of the Reaction of Li with Crystalline Si, *J. Electrochem. Soc.* 154 (2007) A156.
- [46] J. Lyubina, Phase transformations and hysteresis in Si-based anode materials, *Appl. Phys. Lett.* 118 (2021).

- [47] J.B. Kim, H.Y. Lee, K.S. Lee, S.H. Lim, S.M. Lee, Fe/Si multi-layer thin film anodes for lithium rechargeable thin film batteries, *Electrochem. Commun.* 5 (2003) 544–548.
- [48] Y. Yao, M.T. McDowell, I. Ryu, H. Wu, N. Liu, L. Hu, W.D. Nix, Y. Cui, Interconnected silicon hollow nanospheres for lithium-ion battery anodes with long cycle life, *Nano Lett.* 11 (2011) 2949–2954.
- [49] V.L. Chevrier, J.R. Dahn, First Principles Model of Amorphous Silicon Lithiation, *J. Electrochem. Soc.* 156 (2009) A454.
- [50] B. Key, R. Bhattacharyya, M. Morcrette, V. Seznéc, J.M. Tarascon, C.P. Grey, Real-time NMR investigations of structural changes in silicon electrodes for lithium-ion batteries, *J. Am. Chem. Soc.* 131 (2009) 9239–9249.
- [51] J. Saint, M. Morcrette, D. Larcher, L. Laffont, S. Beattie, J.P. Pères, D. Talaga, M. Couzi, J.M. Tarascon, Towards a fundamental understanding of the improved electrochemical performance of silicon-carbon composites, *Adv. Funct. Mater.* 17 (2007) 1765–1774.
- [52] J. Graetz, C.C. Ahn, R. Yazami, B. Fultz, Highly reversible lithium storage in nanostructured silicon, *Electrochem. Solid-State Lett.* 6 (2003) A194–A197.
- [53] H. Wu, Y. Cui, Designing nanostructured Si anodes for high energy lithium ion batteries, *Nano Today.* 7 (2012) 414–429.
- [54] J.S. Edge, S. O’Kane, R. Prosser, N.D. Kirkaldy, A.N. Patel, A. Hales, A. Ghosh, W. Ai, J. Chen, J. Yang, S. Li, M.C. Pang, L. Bravo Diaz, A. Tomaszewska, M.W. Marzook, K.N. Radhakrishnan, H. Wang, Y. Patel, B. Wu, G.J. Offer, Lithium ion battery degradation: what you need to know, *Phys. Chem. Chem. Phys.* 23 (2021) 8200–8221.

- [55] H.S. Sitinamaluwa, H. Li, K.C. Wasalathilake, A. Wolff, T. Tesfamichael, S. Zhang, C. Yan, Nanoporous SiO coated amorphous silicon anode material with robust mechanical behavior for high-performance rechargeable Li-ion batteries, *Nano Mater. Sci.* 1 (2019) 70–76.
- [56] M. Otero, C. Heim, E.P.M. Leiva, N. Wagner, A. Friedrich, Design-Considerations regarding Silicon/Graphite and Tin/Graphite Composite Electrodes for Lithium-Ion Batteries, *Sci. Rep.* 8 (2018) 1–10.
- [57] H. Wu, G. Chan, J.W. Choi, I. Ryu, Y. Yao, M.T. Mcdowell, S.W. Lee, A. Jackson, Y. Yang, L. Hu, Y. Cui, Stable cycling of double-walled silicon nanotube battery anodes through solid-electrolyte interphase control, *Nat. Nanotechnol.* 7 (2012) 310–315.
- [58] N. Dimov, S. Kugino, M. Yoshio, Mixed silicon–graphite composites as anode material for lithium ion batteries: Influence of preparation conditions on the properties of the material, *J. Power Sources.* 136 (2004) 108–114.
- [59] Z. Luo, D. Fan, X. Liu, H. Mao, C. Yao, Z. Deng, High performance silicon carbon composite anode materials for lithium ion batteries, *J. Power Sources.* 189 (2009) 16–21.
- [60] X. Shen, Z. Tian, R. Fan, L. Shao, D. Zhang, G. Cao, L. Kou, Y. Bai, Research progress on silicon/carbon composite anode materials for lithium-ion battery, *J. Energy Chem.* 27 (2018) 1067–1090.
- [61] U. Kasavajjula, C. Wang, A.J. Appleby, Nano- and bulk-silicon-based insertion anodes for lithium-ion secondary cells, *J. Power Sources.* 163 (2007) 1003–1039.
- [62] J. Wu, Y. Cao, H. Zhao, J. Mao, Z. Guo, The critical role of carbon in marrying silicon and graphite anodes for high-energy lithium-ion batteries, *Carbon Energy.* 1 (2019) 57–76.

- [63] J. Sturm, A. Rheinfeld, I. Zilberman, F.B. Spingler, S. Kosch, F. Frie, A. Jossen, Modeling and simulation of inhomogeneities in a 18650 nickel-rich, silicon-graphite lithium-ion cell during fast charging, *J. Power Sources*. 412 (2019) 204–223.
- [64] P. Li, H. Kim, S.T. Myung, Y.K. Sun, Diverting Exploration of Silicon Anode into Practical Way: A Review Focused on Silicon-Graphite Composite for Lithium Ion Batteries, *Energy Storage Mater.* 35 (2021) 550–576.
- [65] K.P.C. Yao, J.S. Okasinski, K. Kalaga, J.D. Almer, D.P. Abraham, Operando Quantification of (De)Lithiation Behavior of Silicon–Graphite Blended Electrodes for Lithium-Ion Batteries, *Adv. Energy Mater.* 9 (2019).
- [66] M. Wetjen, D. Pritzl, R. Jung, S. Solchenbach, R. Ghadimi, H.A. Gasteiger, Differentiating the Degradation Phenomena in Silicon-Graphite Electrodes for Lithium-Ion Batteries, *J. Electrochem. Soc.* 164 (2017) A2840–A2852.
- [67] X. Li, A.M. Colclasure, D.P. Finegan, D. Ren, Y. Shi, X. Feng, L. Cao, Y. Yang, K. Smith, Degradation mechanisms of high capacity 18650 cells containing Si-graphite anode and nickel-rich NMC cathode, *Electrochim. Acta.* 297 (2019) 1109–1120.
- [68] G. Nava, J. Schwan, M.G. Boebinger, M.T. McDowell, L. Mangolini, Silicon-Core-Carbon-Shell Nanoparticles for Lithium-Ion Batteries: Rational Comparison between Amorphous and Graphitic Carbon Coatings, *Nano Lett.* 19 (2019) 7236–7245.
- [69] K.P.C. Yao, J.S. Okasinski, K. Kalaga, J.D. Almer, D.P. Abraham, Operando Quantification of (De)Lithiation Behavior of Silicon–Graphite Blended Electrodes for Lithium-Ion Batteries, *Adv. Energy Mater.* 9 (2019) 1–7.

- [70] E. Moyassari, T. Roth, S. Kücher, C.-C. Chang, S.-C. Hou, F.B. Spingler, A. Jossen, The Role of Silicon in Silicon-Graphite Composite Electrodes Regarding Specific Capacity, Cycle Stability, and Expansion, *J. Electrochem. Soc.* 169 (2022) 010504.
- [71] X. Han, L. Lu, Y. Zheng, X. Feng, Z. Li, J. Li, M. Ouyang, A review on the key issues of the lithium ion battery degradation among the whole life cycle, *ETransportation*. 1 (2019).
- [72] J. Sturm, A. Rheinfeld, I. Zilberman, F.B. Spingler, S. Kosch, F. Frie, A. Jossen, Modeling and simulation of inhomogeneities in a 18650 nickel-rich, silicon-graphite lithium-ion cell during fast charging, *J. Power Sources*. 412 (2019) 204–223.
- [73] Wojtala M E, Zülke A A, Burrell R, et al. Entropy profiling for the diagnosis of NCA/Gr-SiO_x Li-ion battery health[J]. *Journal of The Electrochemical Society*, 2022, 169(10): 100527.
- [74] D. Allart, M. Montaru, H. Gualous, Model of Lithium Intercalation into Graphite by Potentiometric Analysis with Equilibrium and Entropy Change Curves of Graphite Electrode, *J. Electrochem. Soc.* 165 (2018) A380–A387.
- [75] D.J. Arnot, E. Allcorn, K.L. Harrison, Effect of Temperature and FEC on Silicon Anode Heat Generation Measured by Isothermal Microcalorimetry, *J. Electrochem. Soc.* 168 (2021) 110509.
- [76] V. Ramadesigan, P.W.C. Northrop, S. De, S. Santhanagopalan, R.D. Braatz, V.R. Subramanian, Modeling and Simulation of Lithium-Ion Batteries from a Systems Engineering Perspective, *J. Electrochem. Soc.* 159 (2012) R31–R45.

- [77] S. Cho, H. Jeong, C. Han, S. Jin, J.H. Lim, J. Oh, State-of-charge estimation for lithium-ion batteries under various operating conditions using an equivalent circuit model, *Comput. Chem. Eng.* 41 (2012) 1–9.
- [78] A. Fotouhi, D.J. Auger, K. Propp, S. Longo, M. Wild, A review on electric vehicle battery modelling: From Lithium-ion toward Lithium-Sulphur, *Renew. Sustain. Energy Rev.* 56 (2016) 1008–1021.
- [79] V.H. Johnson, Battery performance models in ADVISOR, *J. Power Sources.* 110 (2002) 321–329.
- [80] E. Vanem, C.B. Salucci, A. Bakdi, Ø.Å. sheim Alnes, Data-driven state of health modelling—A review of state of the art and reflections on applications for maritime battery systems, *J. Energy Storage.* 43 (2021) 103158.
- [81] M.-F. Ge, Y. Liu, X. Jiang, J. Liu, A review on state of health estimations and remaining useful life prognostics of lithium-ion batteries, *Measurement.* 174 (2021) 109057.
- [82] W. Guo, Z. Sun, S.B. Vilsen, J. Meng, D.I. Stroe, Review of “grey box” lifetime modeling for lithium-ion battery: Combining physics and data-driven methods, *J. Energy Storage.* 56 (2022).
- [83] M. Doyle, T.F. Fuller, J. Newman, Modeling of Galvanostatic Charge and Discharge of the Lithium/Polymer/Insertion Cell, *J. Electrochem. Soc.* 140 (1993) 1526–1533.
- [84] T.F. Fuller, M. Doyle, J. Newman, Simulation and Optimization of the Dual Lithium Ion Insertion Cell, *J. Electrochem. Soc.* 141 (1994) 1–10.
- [85] J. Newman, K.E. Thomas, H. Hafezi, D.R. Wheeler, Modeling of lithium-ion batteries, *J. Power Sources.* 119–121 (2003) 838–843.

- [86] P. Johari, Y. Qi, V.B. Shenoy, The mixing mechanism during lithiation of Si negative electrode in Li-ion batteries: An Ab initio molecular dynamics study, *Nano Lett.* 11 (2011) 5494–5500.
- [87] Y. Jiang, L. Zhang, G. Offer, H. Wang, A user-friendly lithium battery simulator based on open-source CFD, *Digit. Chem. Eng.* 5 (2022) 100055.
- [88] Y. Ha, D.P. Finegan, A.M. Colclasure, S.E. Trask, M. Keyser, Evaluating temperature dependent degradation mechanisms of silicon-graphite electrodes and the effect of fluoroethylene carbonate electrolyte additive, *Electrochim. Acta.* 394 (2021) 139097.
- [89] N.T. Tran, M. Vilathgamuwa, T. Farrell, S.S. Choi, Matlab simulation of lithium ion cell using electrochemical single particle model, 2016 IEEE 2nd Annu. South. Power Electron. Conf. SPEC 2016. (2016) 2–7.
- [90] X. Han, M. Ouyang, L. Lu, J. Li, Simplification of physics-based electrochemical model for lithium ion battery on electric vehicle. Part I: Diffusion simplification and single particle model, *J. Power Sources.* 278 (2015) 802–813.
- [91] X. Liu, W. Ai, M. Naylor Marlow, Y. Patel, B. Wu, The effect of cell-to-cell variations and thermal gradients on the performance and degradation of lithium-ion battery packs, *Appl. Energy.* 248 (2019) 489–499.
- [92] S.G. Marquis, V. Sulzer, R. Timms, C.P. Please, S.J. Chapman, An Asymptotic Derivation of a Single Particle Model with Electrolyte, *J. Electrochem. Soc.* 166 (2019) A3693–A3706.
- [93] E.J.F. Dickinson, A.J. Wain, The Butler-Volmer equation in electrochemical theory: Origins, value, and practical application, *J. Electroanal. Chem.* 872 (2020) 114145.

- [94] M. Torchio, L. Magni, R.B. Gopaluni, R.D. Braatz, D.M. Raimondo, LIONSIMBA: A Matlab Framework Based on a Finite Volume Model Suitable for Li-Ion Battery Design, Simulation, and Control, *J. Electrochem. Soc.* 163 (2016) A1192–A1205.
- [95] M. Doyle, J. Newman, A.S. Gozdz, C.N. Schmutz, J. Tarascon, Comparison of Modeling Predictions with Experimental Data from Plastic Lithium Ion Cells, *J. Electrochem. Soc.* 143 (1996) 1890–1903.
- [96] G.G. Botte, R.E. White, Modeling Lithium Intercalation in a Porous Carbon Electrode, *J. Electrochem. Soc.* 148 (2001) A54.
- [97] Y. Jiang, Z. Niu, G. Offer, J. Xuan, H. Wang, Insights into the Role of Silicon and Graphite in the Electrochemical Performance of Silicon/Graphite Blended Electrodes with a Multi-Material Porous Electrode Model, *J. Electrochem. Soc.* 169 (2022) 020568.
- [98] H. Yang, F. Fan, W. Liang, X. Guo, T. Zhu, S. Zhang, A chemo-mechanical model of lithiation in silicon, *J. Mech. Phys. Solids.* 70 (2014) 349–361.
- [99] M. Wang, X. Xiao, Investigation of the chemo-mechanical coupling in lithiation/delithiation of amorphous Si through simulations of Si thin films and Si nanospheres, *J. Power Sources.* 326 (2016) 365–376.
- [100] A.F. Bower, P.R. Guduru, V.A. Sethuraman, A finite strain model of stress, diffusion, plastic flow, and electrochemical reactions in a lithium-ion half-cell, *J. Mech. Phys. Solids.* 59 (2011) 804–828.
- [101] M. Wang, X. Xiao, X. Huang, A multiphysics microstructure-resolved model for silicon anode lithium-ion batteries, *J. Power Sources.* 348 (2017) 66–79.

- [102] S.C. Jung, Y.-K. Han, Ab initio molecular dynamics simulation of lithiation-induced phase-transition of crystalline silicon, *Electrochim. Acta.* 62 (2012) 73–76.
- [103] J. Sturm, A. Rheinfeld, I. Zilberman, F.B. Spingler, S. Kosch, F. Frie, A. Jossen, Modeling and simulation of inhomogeneities in a 18650 nickel-rich, silicon-graphite lithium-ion cell during fast charging, *J. Power Sources.* 412 (2019) 204–223.
- [104] S. Dhillon, G. Hernández, N.P. Wagner, A.M. Svensson, D. Brandell, Modelling capacity fade in silicon-graphite composite electrodes for lithium-ion batteries, *Electrochim. Acta.* 377 (2021).
- [105] P.-F. Lory, B. Mathieu, S. Genies, Y. Reynier, A. Boulineau, W. Hong, M. Chandesris, Probing Silicon Lithiation in Silicon-Carbon Blended Anodes with a Multi-Scale Porous Electrode Model, *J. Electrochem. Soc.* 167 (2020) 120506.
- [106] X. Gao, W. Lu, J. Xu, Modeling framework for multiphysics-multiscale behavior of Si–C composite anode, *J. Power Sources.* 449 (2020) 227501.
- [107] D.J. Pereira, J.W. Weidner, T.R. Garrick, The Effect of Volume Change on the Accessible Capacities of Porous Silicon-Graphite Composite Anodes, *J. Electrochem. Soc.* 166 (2019) A1251–A1256.
- [108] B. Liu, Y. Jia, J. Li, H. Jiang, S. Yin, J. Xu, Multiphysics coupled computational model for commercialized Si/graphite composite anode, *J. Power Sources.* 450 (2020) 227667.
- [109] Y. Jiang, G. Offer, J. Jiang, M. Marinescu, H. Wang, Voltage Hysteresis Model for Silicon Electrodes for Lithium Ion Batteries, Including Multi-Step Phase Transformations, Crystallization and Amorphization, *J. Electrochem. Soc.* 167 (2020) 130533.

- [110] M. Verbrugge, D. Baker, X. Xiao, Formulation for the Treatment of Multiple Electrochemical Reactions and Associated Speciation for the Lithium-Silicon Electrode, *J. Electrochem. Soc.* 163 (2016) A262–A271.
- [111] J.-B. Kim, S.-H. Lim, S.-M. Lee, Structural Change in Si Phase of Fe/Si Multilayer Thin-Film Anodes during Li Insertion/Extraction Reaction, *J. Electrochem. Soc.* 153 (2006) A455–A458.
- [112] C.E. Nicholson, Crystallisation in emulsion and microemulsion systems Systems, Durham University, 2006. <http://etheses.dur.ac.uk/1298/>.
- [113] C.A. Angell, Supercooled water, *Annu. Rev. Phys. Chem.* 34 (1983) 593–630.
- [114] Q. Meng, Y. Rong, T.Y. Hsu, Nucleation barrier for phase transformations in nanosized crystals, *Phys. Rev. B.* 65 (2002) 174118.
- [115] M. Verbrugge, D. Baker, B. Koch, X. Xiao, W. Gu, Thermodynamic Model for Substitutional Materials: Application to Lithiated Graphite, Spinel Manganese Oxide, Iron Phosphate, and Layered Nickel-Manganese-Cobalt Oxide, *J. Electrochem. Soc.* 164 (2017) E3243–E3253.
- [116] C.R. Birkl, E. McTurk, M.R. Roberts, P.G. Bruce, D.A. Howey, A Parametric Open Circuit Voltage Model for Lithium Ion Batteries, *J. Electrochem. Soc.* 162 (2015) A2271–A2280.
- [117] E.P. Donovan, F. Spaepen, D. Turnbull, J.M. Poate, D.C. Jacobson, Calorimetric studies of crystallization and relaxation of amorphous Si and Ge prepared by ion implantation, *J. Appl. Phys.* 57 (1985) 1795–1804.
- [118] N. Bernstein, M.J. Aziz, E. Kaxiras, Amorphous-crystal interface in silicon: A tight-binding simulation, *Phys. Rev. B.* 58 (1998) 4579.
- [119] M. Wang, X. Xiao, X. Huang, A multiphysics microstructure-resolved model for silicon anode lithium-ion batteries, *J. Power Sources.* 348 (2017) 66–79.

- [120] V.A. Sethuraman, V. Srinivasan, J. Newman, Analysis of Electrochemical Lithiation and Delithiation Kinetics in Silicon, *J. Electrochem. Soc.* 160 (2013) A394–A403.
- [121] T. Swamy, Y.-M. Chiang, Electrochemical charge transfer reaction kinetics at the silicon-liquid electrolyte interface, *J. Electrochem. Soc.* 162 (2015) A7129–A7134.
- [122] J. Li, X. Xiao, F. Yang, M.W. Verbrugge, Y.-T. Cheng, Potentiostatic intermittent titration technique for electrodes governed by diffusion and interfacial reaction, *J. Phys. Chem. C.* 116 (2012) 1472–1478.
- [123] B. Lu, Y. Song, Q. Zhang, J. Pan, Y.T. Cheng, J. Zhang, Voltage hysteresis of lithium ion batteries caused by mechanical stress, *Phys. Chem. Chem. Phys.* 18 (2016) 4721–4727.
- [124] J.H. Ryu, J.W. Kim, Y.E. Sung, S.M. Oh, Failure modes of silicon powder negative electrode in lithium secondary batteries, *Electrochem. Solid-State Lett.* 7 (2004).
- [125] M.N. Obrovac, L.J. Krause, Reversible Cycling of Crystalline Silicon Powder, *J. Electrochem. Soc.* 154 (2007) A103.
- [126] D.R. Baker, M.W. Verbrugge, X. Xiao, An approach to characterize and clarify hysteresis phenomena of lithium-silicon electrodes, *J. Appl. Phys.* 122 (2017) 0–11.
- [127] M. Avrami, Kinetics of phase change. I General theory, *J. Chem. Phys.* 7 (1939) 1103–1112.
- [128] Y. Jiang, G. Offer, J. Jiang, M. Marinescu, H. Wang, Voltage Hysteresis Model for Silicon Electrodes for Lithium Ion Batteries, Including Multi-Step

- Phase Transformations, Crystallization and Amorphization, *J. Electrochem. Soc.* 167 (2020) 130533.
- [129] M. Doyle, J. Newman, *Design of Lithium / Polymer Battery Systems*, 40 (1995).
- [130] E. Moyassari, L. Streck, N. Paul, M. Trunk, R. Neagu, C.-C. Chang, S.-C. Hou, B. Märkisch, R. Gilles, A. Jossen, Impact of Silicon Content within Silicon-Graphite Anodes on Performance and Li Concentration Profiles of Li-Ion Cells using Neutron Depth Profiling, *J. Electrochem. Soc.* 168 (2021) 020519.
- [131] Z. Shao, Y. Jiang, G. Offer, H. Wang, Modeling of the Thermal Behaviors of Silicon/Graphite Composite Electrodes for Lithium-ion Batteries, *Energy*. 2004 (2022) 2965.
- [132] Y. Zhao, Y. Patel, T. Zhang, G.J. Offer, Modeling the Effects of Thermal Gradients Induced by Tab and Surface Cooling on Lithium Ion Cell Performance, *J. Electrochem. Soc.* 165 (2018) A3169–A3178.
- [133] L.M. Housel, W. Li, C.D. Quilty, M.N. Vila, L. Wang, C.R. Tang, D.C. Bock, Q. Wu, X. Tong, A.R. Head, K.J. Takeuchi, A.C. Marschilok, E.S. Takeuchi, Insights into Reactivity of Silicon Negative Electrodes: Analysis Using Isothermal Microcalorimetry, *ACS Appl. Mater. Interfaces*. 11 (2019) 37567–37577.
- [134] J.M. Larkin, A.J.H. McGaughey, Thermal conductivity accumulation in amorphous silica and amorphous silicon, *Phys. Rev. B - Condens. Matter Mater. Phys.* 89 (2014) 144303.
- [135] D.R. Queen, The specific heat of pure and hydrogenated amorphous silicon, UC Berkeley, 2011. <https://escholarship.org/uc/item/58d766kb#author> (accessed May 25, 2022).

- [136] G. Tritsarlis, K. Zhao, ... O.O.-T.J. of P., undefined 2012, Diffusion of lithium in bulk amorphous silicon: a theoretical study, ACS Publ. 116 (2012) 22212–22216.
- [137] Z. Chen, D.L. Danilov, R.-A. Eichel, P.H.L. Notten, Li⁺ concentration waves in a liquid electrolyte of Li-ion batteries with porous graphite-based electrodes, Energy Storage Mater. 48 (2022) 475–486.
- [138] Q. Wang, B. Mao, S.I. Stoliarov, J. Sun, A review of lithium ion battery failure mechanisms and fire prevention strategies, Prog. Energy Combust. Sci. 73 (2019) 95–131.
- [139] H. Li, X. Kong, C. Liu, J. Zhao, Study on thermal stability of nickel-rich/silicon-graphite large capacity lithium ion battery, Appl. Therm. Eng. 161 (2019) 114144.

Appendices

A1. Entropic coefficients

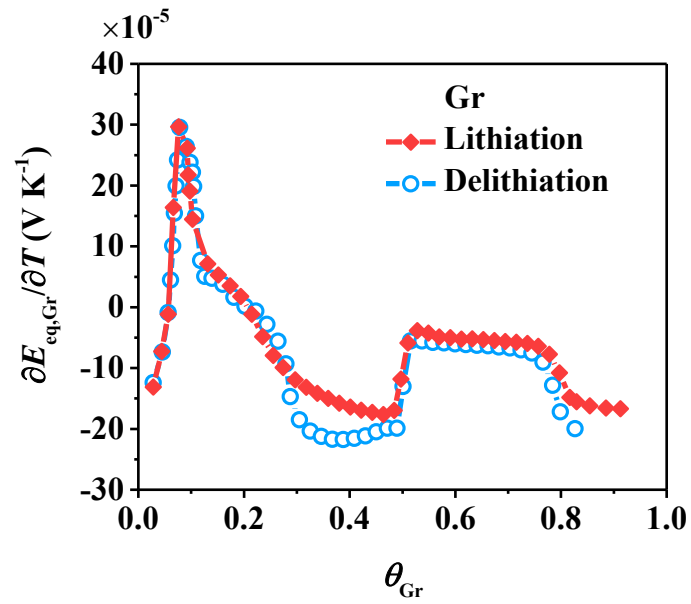


Figure A1-1 Evolution of entropic coefficient ($\frac{\partial E_{eq,Gr}}{\partial T}$) with state of charge during (de)lithiation for graphite electrodes. Data retrieved from Ref. [74], where θ_{Gr} is valid in the range of [0.28, 0.91] and [0.28, 0.83] during lithiation and delithiation respectively.

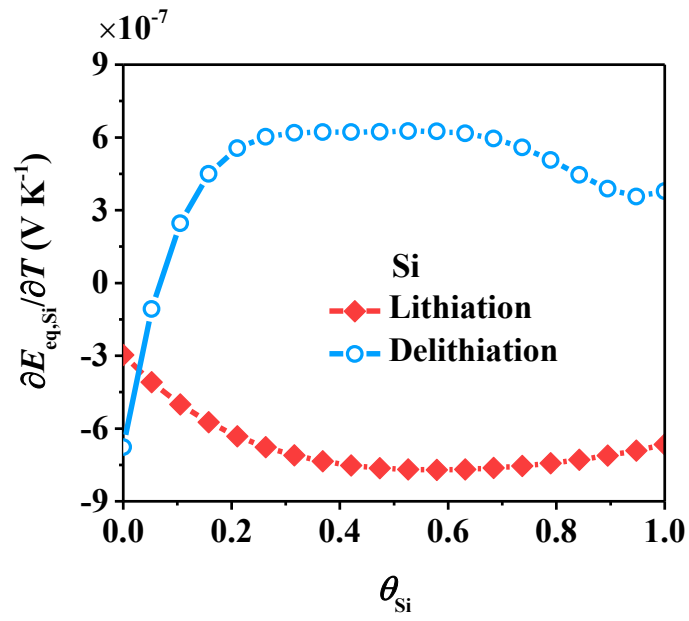


Figure A1-2 Evolution of entropic coefficient ($\frac{\partial E_{eq,Si}}{\partial T}$) with state of charge during (de)lithiation for silicon electrodes. Data retrieved from Ref. [75], where θ_{Si} is valid in the range of [0, 1] during both lithiation and delithiation.

A2. Solution procedure of the developed battery model

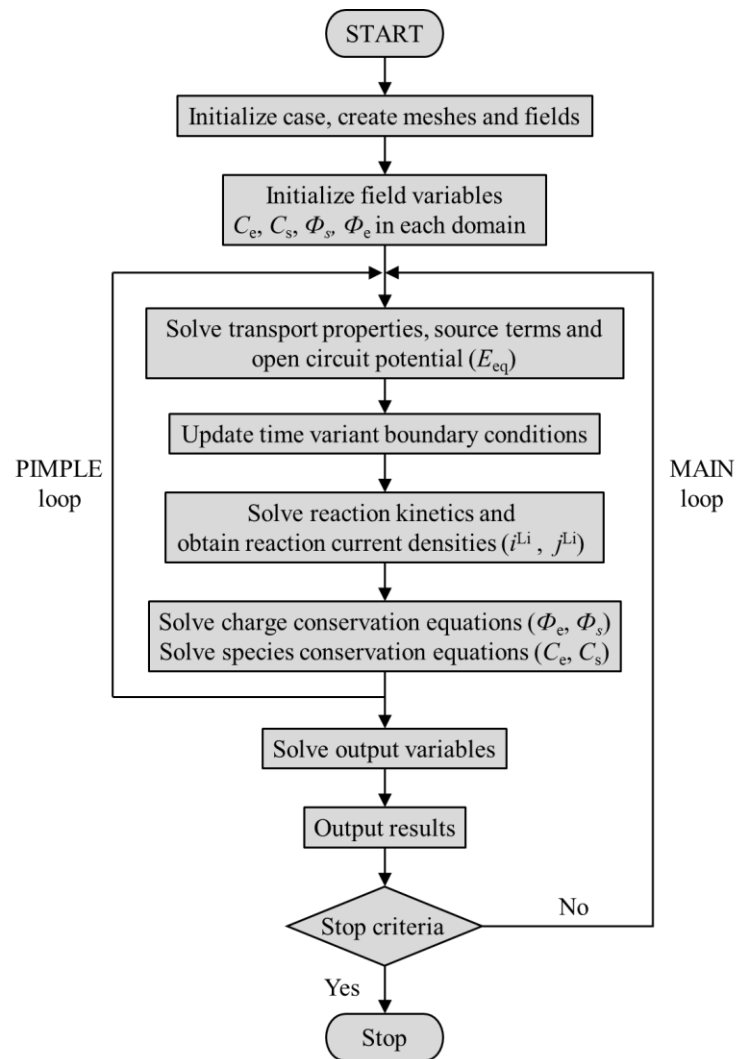


Figure A2-1 Programming flowchart of the developed battery solver.